2003

Numerical solution of ocular fluid dynamics

Satish Kumar
Louisiana State University and Agricultural and Mechanical College, skumar3@lsu.edu

NUMERICAL SOLUTION OF OCULAR FLUID DYNAMICS

A Thesis

Submitted to the Graduate Faculty of the
Louisiana State University and
Agricultural and Mechanical College
In partial fulfillment of the
Requirements for the degree of
Master of Science in Mechanical Engineering

In

The Department of Mechanical Engineering

by
Satish Kumar
B.Tech., Indian Institute of Technology, 2001
December, 2003

ACKNOWLEDGEMENTS

I would like to thank my major professor, Prof. Sumanta Acharya, for sponsoring and mentoring me on this project and my graduate school experience. Without his guidance and drive, I would have never reached the level of achievement or professional growth that I have attained over the last two years at LSU. Observing his critical thinking skills and clarity of thinking has improved me not only professionally, but also more importantly, personally. I would also like to thank Dr. Kevin Kelly and Dr. Ram Devireddy for serving in my committee and BCVC (Biological Computing and Visualization Center) for funding this project.

TABLE OF CONTENTS

LIST OF TABLES

LIST OF FIGURES

ABSTRACT

Numerical calculations of the aqueous humor dynamics in the anterior chamber of both the rabbit and the human eye are presented to delineate the basic flow and transport mechanisms. The calculations are based on a geometrical model of the eye, which represents the Trabecular mesh (TM) as a multi-layered porous zone of specified pore sizes and void fraction. Buoyancy is observed to be the dominant driving mechanism for the convective motion in both orientations (horizontal and vertical) of the eye. Reducing the TM pore size does not appear to have a significant influence on the intra-ocular pressure (IOP) until the pore size drops below 1 micron beyond which a significant increase in IOP is observed.

Simulations of particle transport are also performed to gain insight about the movement and deposition of particles of different characteristics and to identify the mechanisms for the development of observed pathological structures. Simulations predict the formation of Krukenberg Spindle through pigment cell deposition on the corneal surface. Simulation of heavy particles present in the AH show that they gravitate inside the eye and a layered structure is formed at the bottom of the anterior chamber. The simulated particle deposition patterns are seen to correspond with clinical observations.

The development of elevated pressure in the eye with pupillary block is simulated and analyzed. Potential surgical procedures (iridectomy) are simulated through virtual opening of holes at different positions along the iris disk. The effect of the location of holes along the iris surface is analyzed for single and two hole iridectomy. Key issues considered in analyzing the results are (a) reduction in IOP, (b) the asymmetry introduced in the flow profile, (c) adequate circulation of the flow in the different region since the flow provides the nutrition to the tissues and (d) the particle deposition on the ocular tissues. It is observed that when a single hole is created, the 12 o'clock iridectomy provides better results than the other locations. The preferred

arrangement with the two-hole iridectomy is the 9 o'clock and 3 o'clock positions since the flow distribution is most symmetrical and circulation is the strongest.

CHAPTER 1. INTRODUCTION

1.1 Objective

The fluid dynamics of the aqueous humor (AH) in the anterior chamber of eye, Fig [1-1] and drainage mechanisms through the Trabecular Meshwork (TM) are not fully understood. The small size of the anterior chamber and complexities of flow measurements inside the living eye makes detailed flow data difficult to obtain. Computational simulation of the flow in the anterior chamber can therefore be very useful in producing the needed understanding of the flow mechanisms. Eye diseases such as Glaucoma are often linked to obstruction of the outflow and high fluid pressure inside the eye. The pressure inside the anterior chamber of eye with respect to the atmospheric pressure is generally defined as the Intra Ocular Pressure (IOP). Increased Intra Ocular Pressure, sustained for a long time, can damage the optic nerve in the eye and can lead to blindness [1]. One of the goals of the present work is to perform flow simulations in models of the rabbit and the human eye, and to analyze the effect of the resistance of the drainage system on the flow distribution and IOP.

Many small particles of different sizes, shapes and traits circulate inside the anterior chamber in the normal or the diseased eye. The interaction of these particles with the ocular tissues depends on their particular characteristics and the flow field of aqueous humor inside the anterior chamber. The behavior of pigment granules, protein particles (albumin), erythrocytes and leucocytes inside the anterior chamber are of great interest to the ophthalmologists in identifying the mechanisms of specific eye diseases. Pigment Dispersion Syndrome (PDS) [2] is a special case of defective eye with high concentration of pigment granules in the aqueous humor. Eyes with PDS may have pigment deposition on the corneal endothelium in a vertical band known as Krukenberg Spindle [2] or heavy pigmentation of the TM. The rupture of blood vessels and bleeding inside the eye leads to accumulation of blood (erythrocytes) inside the anterior chamber

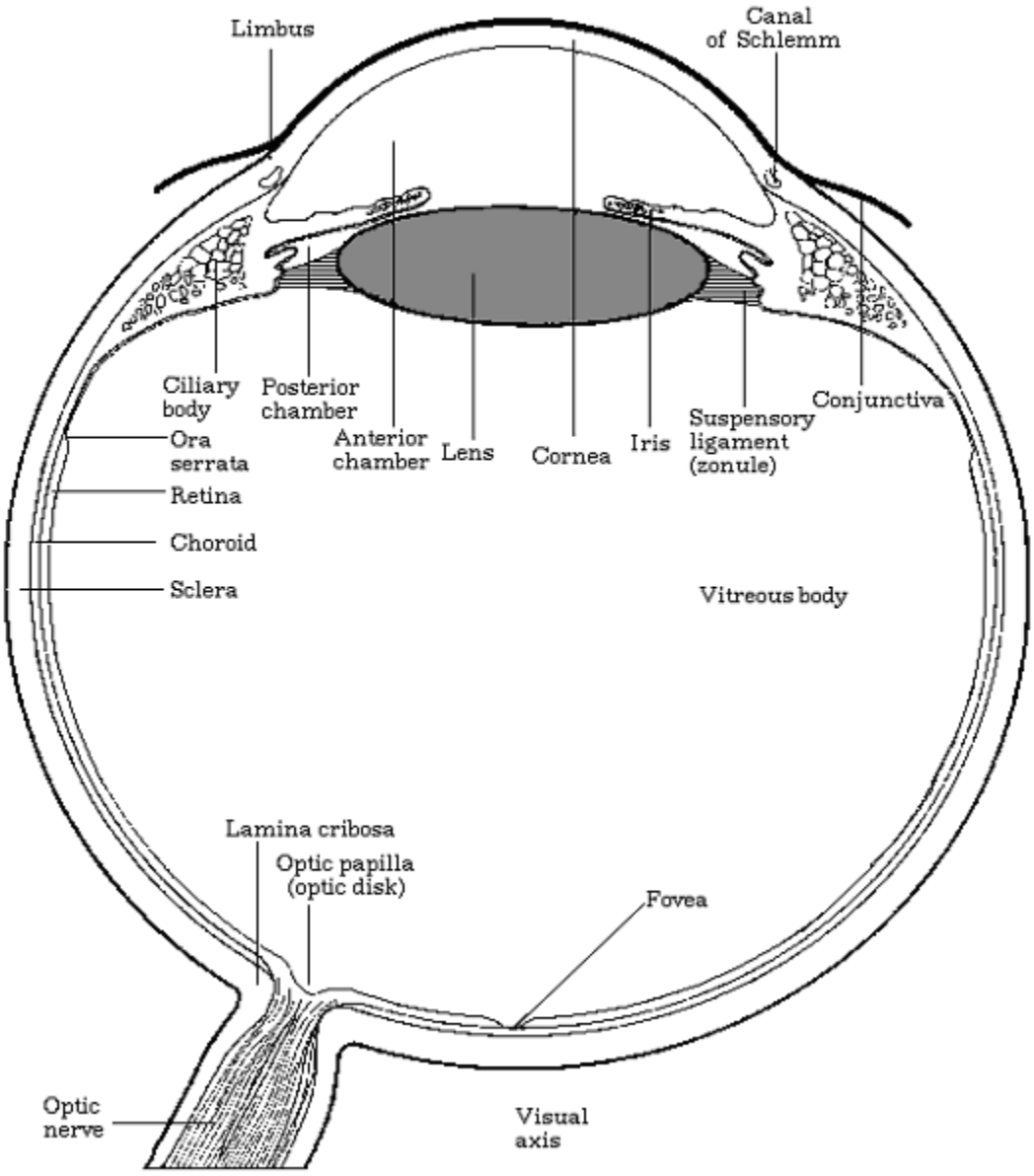

Figure 1-1. Horizontal mid section of human eye.

[3]. and formation of Hyphema [4]. In cases of ocular inflammation leucocytes sediment at the bottom of the anterior chamber and forms a white layered structure known as Hypopyon [5]. Obtaining flow data and visualizing the behavior of different particles is a difficult task with present-day medical tools. The present work is aimed to perform computational simulations inside a geometrical model of eye to get insight about the movement and deposition of particles

of different characteristics and formation of some observed clinical structures (Krukenberg Spindle, Hyphema and Hypopyon).

Angle closure in the anterior chamber occurs when the peripheral iris is lifted upwards and physically opposes the trabecular meshwork or corneal endothelium impeding the aqueous outflow. The most common reason for angle closure is pupillary block, whereby the flow of aqueous from the posterior to anterior chamber is inhibited. This may be simply due to genetic predisposition and anterior segment anatomy (primary pupil block), or from posterior synechiae, lenticular enlargement or displacement of the lens (secondary pupil block). Blockage of the pores of TM by the anterior iris surface leads to elevation in IOP of the eye and the development of Angle Closure Glaucoma. Laser iridectomy is the treatment of choice for most cases of Angle Closure Glaucoma, which is a surgical process of making small holes in the iris to enable the easy passage of AH from posterior chamber to anterior chamber. This surgery leads to decrease of pressure difference between the anterior and posterior chambers; iris contours preoccupies its shape and IOP drops to the normal value. The objective of the work is to analyze the process of pupillary block and development of elevated pressure. The iridectomy surgical procedure is simulated to investigate the flow and pressure distribution after opening of holes at different positions along the iris disk.

Aqueous humor is formed by secretion and ultra-filtration in the highly vascularized ridges projected from the ciliary body of the posterior chamber. The bulk flow rate of the aqueous humor into the anterior chamber of normal human eye varies in the range of 1.5-2.5 $\mu L/\min$ [6], while for pigmented rabbits it varies in the range of 1.0-2.5 $\mu L/\min$ [6]. It enters the anterior chamber through the pupil between the lens and iris. More than 80% of the aqueous humor in the rabbit eye exits through the Trabecular Meshwork (TM) into the Schlemm's canal [7], which is located in the junction of the iris and cornea. The aqueous humor is then discharged into the

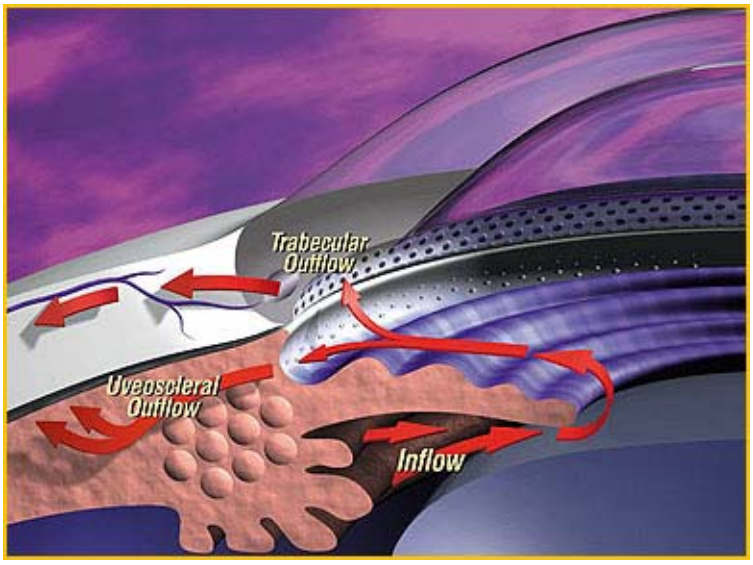

Figure 1-2: Outflow system of human eye.

venous system, either through the aqueous veins or through the episcleral veins. Another exit pathway for the AH is the uveoscleral drainage system where the AH enters the iris root and passes between the muscle bundles in the ciliary body to the choroids and out through the episcleral tissues. This pathway contributes little to the outflow in the rabbit eyes (20 %) and is neglected in the present study [7].

The blood flow in the iris and the ciliary body maintain their tissues at the body temperature (37^0C) [8, 9]. The outer surface of the cornea (0.6 mm thick) [10] is generally maintained at 32-33 ^0C [11,12] by the tear film evaporation. The inner corneal surface is at lower temperature, and is only 2-4 ^0C less than the body temperature because of the thermal resistance provided by the corneal tissues. However, the small temperature difference (2-4 ^0C) across the anterior chamber is believed to be the dominant mechanism driving the fluid flow in the anterior chamber of the eye.

The outflow network system of the eye consists of a graded porous mesh from the inside of the eye to the outside. These include: (1) the uveal and corneoscleral meshwork, (2) the juxtacanalicular meshwork (JCM), (3) the endothelial wall of the Schlemm's canal, (4) the

Schlemm's canal, and (5) the aqueous veins. Both the uveal and corneoscleral meshwork have negligible resistance because of their bigger pore size (25-75 μ) [10]. It is believed that the tortuous flow passage from the JCM accounts for the most of the flow resistance [13, 14] because of its very small pore size (~1.0 μ) [15] and the presence of the extra-cellular matrix gel in the open spaces.

The present study is intended to develop a model for identifying the mechanisms for the development of Krukenberg-spindle, Hyphema and Hypopyon, which are the structures formed inside the eye due to the deposition of particles in the anterior chamber. The achievement of the model is to include the effect of TM resistance in determining the flow and pressure distribution inside the eye, particle deposition rates and locations, and how they are related with different pathological conditions of the eye. A comprehensive three-dimensional flow simulation is presented where the details of the TM are represented as a graded porous structure, and the flow patterns and the pressure distribution in the anterior chamber for different parametric conditions are analyzed to delineate key flow mechanisms and parametric effects. Both the horizontal, upward-facing orientation of the eye and the vertical orientation of the eye are considered. Simulations are performed for both rabbit and human eye, which have different dimensions of eye globe. The work is extended to simulate some surgical procedures (iridectomy), which is applied on eye for the treatment of Glaucoma.

1.2 Literature Survey

Computational modeling of complex drainage system of eye and obtaining an insight in the variation of IOP for various pathological conditions is an extremely complicated problem. Several models have been previously reported that explore the temperature distribution and flow mechanism inside the anterior chamber of eye, but these models are limited due to many assumptions and simplifications. None of the computational models reported in the literature have

attempted to include the TM to obtain flow field inside the anterior chamber and analyze its effect on IOP.

Johnson and Kamm [16] have proposed a mathematical model of Schlemm's canal to simulate the collapse of the canal and its resistive effect on the aqueous outflow. Their theoretical model is focused on the analysis of two principle sites of resistance, Schlemm's canal and Inner wall of Schlemm's canal. In their flow model, the aqueous humor flows from the TM through the inner wall, into the Schlemm's canal, and along the canal in the circumferential direction, and finally exits through a number of spaced collector channels. They modeled the TM as a series of linear springs that allow the inner wall to deform in proportion to the local pressure drop across it. In their model the inner wall is supported by the meshwork attachment and is flexible in accordance with the pressure changes, while the outer wall is assumed rigid. They concluded that most of the resistance in the aqueous outflow network occurs along the inner wall of the Schlemm's canal, and Glaucoma is a consequence of the collapse of the Schlemm's canal alone. They completely ignored the effect of JCM on the outflow resistance, which is considered by a number of investigators to be most important site of the outflow resistance.

Ethier et al. [17] later developed a model to determine the relation between the resistance of the meshwork with the concentration of the extra-cellular matrix- gel of JCM. They proposed two computational models that could predict the flow resistance of the JCM. In the first model they described the JCM as a porous medium permeated by open spaces (pores) through which aqueous humor flows. This model under predicts the resistance of JCM by a factor of 10-100, which suggests that the gel, which fills the open spaces of JCM, may control the resistance of the tissue. In the second model open spaces of the JCM is filled with a GAG gel for predicting the flow resistance of the gel. This model showed that the measured bulk concentration of GAG gel was consistent with gel concentrations needed to account for the estimated resistance of the JCM in vivo. The entire model is based on the analysis of the effect of gel-concentration on the JCM resistance to outflow, but they did not focus on the flow field and related IOP.

Johnson et al. [18] proposed a model to explore possible hydrodynamic interactions between JCM and inner wall pores of the Schlemm's canal. In their study they have considered the JCM and inner wall of Schelmm's canal as a coupled system to analyze the interaction between these two important sites of outflow resistance. This interaction arises because the pores in the inner wall endothelium are small and well separated. The flow is non-uniform in JCM and preferentially directed towards the region, which are in vicinity of the pores of inner wall endothelium, reducing the effective cross-section area available for the flow of aqueous humor. This funneling interaction of the pores markedly increases the effective resistance of the JCM by 30-fold. This increase was not due to the flow resistance of the inner wall themselves, rather flow resistance was the result of a decrease in the effective area through which the fluid must flow. They have determined a simple relationship for estimating the magnitude of this effect as a function of the number of the pores and their size. Their work is again limited to the analysis of pores and relation of their resistive effect with respect to the other parts of the drainage system.

Scott [19] has presented a mathematical model of human eye based on the bio-heat heat transfer equation for calculating the intra-ocular temperature distribution. They have used the Galerkin finite element method for analyzing the sensitivity of the temperature distribution in the unexposed eye to the uncertainties in the parameters investigated, which includes thermal conductivities of the ocular tissues, the heat loss from the anterior corneal surface to the surroundings by convection and evaporation and the convective heat loss from the sclera to the body core. Scott [20] has extended this work to calculate the temperature rise experienced by the intra-ocular media when exposed to infrared radiation. The model is used to calculate transient and steady state temperature distributions for different exposure times and a range of incident irradiances. They did not solve for the intra-ocular flow field, so their analysis of temperature rise is done without inclusion of buoyancy, and therefore the model does not predict realistic temperature rise.

Heys et al. [7] presented a two-dimensional mathematical model of the coupled aqueous humor-iris system that accounts for the passive iris deformation to the iris contour. They modeled the aqueous humor as the Newtonian fluid and iris as linear elastic solid. They solved the resulting coupled equation set by finite element method with mesh motion in response to the iris displacement accomplished by tracking a pseudo-solid overlying the aqueous humor. Their simulation for normal eyes shows that the iris is displaced by the aqueous humor as it circulates through the anterior segment. Their model predicts the iris contour and apparent iris lens contact, which is primarily a function of the aqueous flow rate, the trabecular meshwork permeability, the permeability of the posterior pathway and iris modulus. They modeled the blinking process by applying a normal stress along the cornea. The model prediction of rise in IOP of eye agrees with the experimental measurement on rabbit's eye, but the shape of the pressure curve has poor agreement. They also predicted the smallest pressure difference (1Kpa) between the anterior and posterior chamber of eye necessary to achieve the dramatic iris contour observed in case of iris bombe. There are many simplifications in the model due to the absence of the third dimension, symmetry about the center axis and neglecting the buoyancy & gravity effect. The other major limitation of the model is that it includes only a portion of the eye. Due to these simplifications, it is unable to accurately represent the flow process.

Heys and Barocas [21] have proposed a mathematical model of the coupled aqueous humor-iris system to predict the effects of the iris accommodation on the iris position and the pressure distribution in the aqueous humor. Their model predicts that the accommodation produces pressure reversal with the anterior chamber pressure being higher than the posterior chamber. This leads to an iris movement into a concave configuration. They confirmed that the magnitude of the bowing is a strong function of the amount of accommodation, but the total time leading to accommodation, the iris attachment point, the iris modulus and TM permeability has negligible effect on the pressure changes and iris contour. The radial symmetry in these models, the neglect of gravity and buoyancy effects, the neglect of the TM and the absence of the third

dimension limits the capabilities of the model to predict the realistic flow mechanisms inside the eye.

Canning et al. [22] solved the flow profile inside the anterior chamber using a simplified three-dimensional computational model and analyzed the deposition of particles leading to the formation of structures inside the eye. Their model show the dominance of buoyancy on the flow field inside the anterior chamber and indicates that only a small temperature difference is required to drive such flows. They analyzed the deposition of pigment particles on the corneal surface and formation of Krukenberg Spindle; they used the criterion that pigment granules stuck to the ocular tissue if the corneal shear stress at that location is less than a particular value. They estimated the maximum possible size of Hyphema that could be formed at the bottom of the anterior chamber by the sedimentation of erythrocytes in case of ocular trauma or rupture of blood vessel. Depending on the balance of settling force and convective flow they determined how far Hyphema could project upward into the flow before its constituents blood cells are swept away by the flow. The absence of third dimension in their model limits the visualization of real flow field. They did not consider the effect of TM and included lot of simplifications in their model, which restrict their simulations to completely depict the behavior of different particles inside the anterior chamber.

Heys and Barocas [23] have proposed a three-dimensional model with a more realistic geometry of eye in which they have included the iris and posterior chamber. They solved for the buoyancy driven ocular flow inside the posterior and anterior chamber. They released the particles from the tip of the iris and the center of the eye and observed their path inside the anterior chamber. They released few particles evenly spaced on the inner circumference of the iris tip and predicted the formation of Krukenberg Spindle based on the plot of particles residence time at different positions in the coronal plane. Their results show two dark bands in the center of the eye, which represent the location where particles circulated for the longest time. There are two outer bands on the corneal surface which is additional region occupied by the particles for the

significant time. They compared these results with the simulations on the eye model with higher temperature gradient across the anterior chamber and found less circulation of particles near to the posterior surface of the cornea for high temperature gradient. Based on these results they suggested that people living in the cooler climate might not develop a spindle as distinct and heavily pigmented as the general population. Although their model is three-dimensional and geometry is more realistic, they have neglected the effect of TM-resistance on deposition of particles, which play a major role in trapping, or escaping of particles of different traits through TM-pores.

1.3 Outline of the Thesis

This first chapter of the present report contained an introduction and a literature survey. The introduction part is an overview of the present work, which explains the problem of interest and the simulations performed in a concise form. The literature survey portion is devoted to present the summary of the previous work done in the field of ocular fluid dynamics.

The second chapter contains the explanation of the eye-physiology. It is important to understand the anatomy of eye, the functioning of its different constituents and the different terminologies used frequently in the context of ocular dynamics. This chapter includes all the required details of the eye to understand the present work. The characteristics of the particles present in the AH and their important role inside the eye is also discussed.

The third chapter is focused on explaining the mathematical and computational model used for the simulations on the eye. The geometry used to represent the ocular tissues and the governing equations, which could predict the ocular fluid dynamics, is explained in detail. Emphasis is given to explain the strategy followed and procedures used for modeling the particles present in the AH and their interaction with the ocular tissues. Finally the boundary conditions used on the ocular tissues to properly represent the environmental conditions of eye and numerical procedure used to solve the governing equations is explained.

Fourth to seventh chapters include the results of the simulations performed and the conclusions drawn. Fourth chapter contains the results of flow simulations on the rabbit eye. The effect of buoyancy is established, the effect of different inlet profiles is compared and the obtained velocity, pressure, temperature and shear stress inside the geometrical model is discussed. The effect of porosity and pore size of the TM on IOP of the eye is analyzed in detail. Finally the effect of temperature difference across the anterior chamber and effect of pupillary expansion is included.

The fifth chapter is concerned with the results and conclusions of particle simulations in the rabbit eye. The trajectories of the particles, their residence time inside the eye and their interaction with the ocular tissues are discussed. The mechanism of formation of Krukenberg Spindle, Hyphema and Hypopyon is analyzed and how the simulation results resemble with the clinical observations are explained in detail.

The sixth chapter is concentrated on explaining the simulation results on the human eye. The human eye has different dimensions compared to the rabbit eye, so the geometrical model for the human eye is different from the rabbit eye. In this chapter the geometrical model of human eye and boundary conditions used on the ocular tissues are discussed; then the flow results in the eye are explained. The last portion of the chapter is focused on discussing the prediction of the model for the formation of Krukrnberg Spindle, Hyphema and Hypopyon inside the eye.

The seventh chapter contains the results of virtual simulation for surgical procedure iridectomy that is commonly used in the treatment of Glaucoma. The results of simulations representing pupillary block and Angle Closure Glaucoma are explained. The outcome of single hole and double hole iridectomy at peripheral and central position is discussed. The comparisons of flow and pressure redistribution for different iridectomy locations are included and best site for the creation of hole is discussed.

CHAPTER 2. PHYSIOLOGY OF EYE

2.1 Anatomy of Eye

The eye globe, approximately spherical in shape, is recessed in the pyramidal shaped bony orbit, and it is connected to the brain by optic nerves. The posterior five-sixth of the globe is covered by external white and opaque protective coat, sclera [10]. The remaining anterior one-sixth of the globe consists of a uniquely transparent, convex, protective fibrous structure, the cornea, which is responsible for the refractive incident rays on eye. The limbus marks the transition between the cornea and sclera, Fig [1-1]. The extra-ocular muscles, which originate into the bony orbit and insert into the sclera, are responsible for the directional movement of the globe. The eyelids provide mechanical protection to the globe, and they interrupt and limit the amount of light entering the eye; they harbor the tear secreting glands and distribute the tear fluid over the anterior surface of the globe.

Interposed between the retina and the sclera is vascular tunic of the choroids which primarily supplies nutrients to the retina. Anteriorly, the choroids continue to the ciliary body, which is responsible for the formation of intraocular fluid, for providing the distal attachment of the zonular fibers of the crystalline lens, and for harboring the smooth muscles [10]. The ciliary body continues anteriorly as the iris, a diaphragm with around contractile opening, the pupil. With its variable diameter, the pupil acting like an automatically adjustable aperture of camera allows rays of light to fall on the retina. The choroids, ciliary body and iris together constitute the uvea.

The anterior chamber, an elliptical space between the iris diaphragm and the cornea, acts as a reservoir for a clear, watery fluid, the aqueous humor. In conjunction with the outer fibrous tunic of the eye, the distended, stable dimensions of the globe are maintained largely by the hydro-mechanical properties of this fluid. The aqueous humor is formed continuously by the

ciliary processes in the posterior chamber behind the iris and flows into the anterior chamber via the pupil; it finally leaves the eye through the intricate system of outflow channels located in the corneoscleral limbus. The resistance encountered during the passage and rate of aqueous humor production is the principal factors determining the level of intraocular pressure. Additionally, this fluid acts as carriers of nutrients, substrates, metabolites and waste products.

The larger posterior chamber of the eye is filled with a transparent, delicate connective tissue gel, and the vitreous humor. The anterior face of the vitreous is hollowed to accommodate the biconvex crystalline lens. The lens, situated behind the iris diaphragm, is supported by suspensory ligaments, also referred to as the zonules that extend between the ciliary body and the lens surface. The lax state of the zonules is imparted by the contraction of the ciliary muscles together with the inherent plasticity of the lens. The lens has the capacity to accommodate to focus outside images clearly to the retina.

2.1.1 Shape and Dimensions of Eyeball

Although the eyeball is referred to as a globe, it is only approximately spherical and consists of segment of two spheres placed one in front of the other. The anterior corneal portion is smaller and more curved than the posterior, has a radius of curvature of about 8 mm, and comprises one-sixth of the surface area of the eye. The cornea is elliptical, with its vertical axis shorter than the horizontal one. The posterior scleral portion is flatter, has a radius of curvature of about 12 mm, and comprises the remaining five-sixths of the ocular surface area.

The anterior and posterior poles are the central points of the corneal and scleral curvatures respectively; the line joining these two poles is the geometric axis. The external geometric axis is measured from the anterior surface of the cornea to the external surface of the sclera, whereas the internal geometric axis is measured only to the anterior surface of the retina. The three diameters of the globe are the sagittal (anterior-posterior), transverse and vertical.

Histologic sections of the globe can be made in several planes. The meridional plane passes through the anterior and posterior poles of the eye and may be vertical, horizontal or

oblique. Sagittal planes lie on either side of the meridional plane and are parallel to it. The equatorial plane is midway between the anterior and posterior poles and is perpendicular to the meridional plane. Sections parallel to the equatorial plane, whether passing anterior or posterior to it, are called transverse, coronal, frontal, or radial planes.

The dimensions of adult human eyes are relatively constant, the average diameters are 24 mm antero-posteriorly (sagittal diameter), 23 mm vertically and 23.5 mm horizontally [10]. The sagittal diameter may vary most, ranging from 21 to 26 mm in normal eyes. With a high degree of axial myopia, the sagittal diameter may be as large as 29 mm; with hypermertopia, it may be as small as 20 mm. The transverse and vertical diameters are less variable with a range of 23 to 25 mm. The circumference of human eye is about 75mm. Overall, the male eye is about 0.5 mm larger than the female eye and the Negro eye is said to be somewhat larger than those of white races. The eye of the newborn is more spherical than the adult eye, and therefore more hypermeteropic, with a sagittal diameter of 16 to 17 mm; this increases rapidly in size to 22-23 by thee years of age. A further increase of about 1 mm occurs between 3 to 13 years, but there after little growth takes place. The eyeball weighs about 7.5 gm, its volume is about 6.5 ml, and its specific gravity varies from 1.002 to 1.009.

2.1.2 Tunics of the Eyeball

The eyeball, bisected along a meridian, discloses the fundamental architectural plan of the globe, Fig [1-1]. The three tunics of the eyeball revealed are the fibrous coat, the uveal tract, and the retina. The external tough fibrous coat is formed by the sclera, which is continuous anteriorly with the cornea and posteriorly with the meningeal covering of the optic nerve. The uveal tract, a highly vascular layer, forms the middle pigmented tunic and is in contact with the sclera. The anterior portion of the uveal tract, the iris, forms a partition subdividing the interior of the eye. The central opening of this diaphragm, the pupil is the aperture of the optical system. The retina forms the whitish, inner tunic of the eyeball and is in contact with the choroid. The nerve fiber layer of the retina continues posteriorly as the optic nerve.

2.1.2.1 Fibrous Tunic

- **Sclera**

The sclera is an opaque, dull white, dense, visco-elastic and resilient outer coat of the eye, which occupies the posterior five-sixth of the globe. Together with the intraocular pressure, the sclera keeps the ocular dimensions stable for optimum visual function. Although the sclera is resilient, the extent of its stretch is not proportional to the intraocular pressure, since the scleral rigidity increases with increasing stretch of the collagen bundles. This rigidity is described as immediate ocular rigidity. The enlargement of the eyeball in congenital glaucoma and myopia is caused by the gradual distension of the scleral coat beyond its elastic limit.

- **Cornea**

The cornea consists of a clear, transparent, avascular, viscoelastic tissue with a smooth, convex external surface and a concave internal surface. It occupies one sixth ($1.3\ cm^2$) of the total surface area of the fibrous coat of the globe. The main function of the cornea is optical; it forms the principal refracting surface of the dioptric system of the eye. Anteriorly, when the lids are open, the cornea is separated from the air only by the precorneal tear film (6-20 μm thick), which imparts the characteristic brilliant luster [10]. The tear film is a physiologic secretion that covers the external surface of the corneal epithelium and, strictly speaking, is not an anatomic part of the cornea. It is divisible into three layers. (a) The anterior oily layer, less than 0.5 μm thick, is derived from the sebaceous glands of the lid and caruncle. (b) The middle aqueous layer, 5-18 μm thick, represents the secretion of the lacrimal glands and dissolved proteins. (c) The posterior mucoid layer (0.5 μm thick), rich in glycoproteins, is derived from the conjunctival goblet cells. By filling minor surface irregularities, the tear film provides a smooth air/cornea interface for refraction of light. The precorneal tear film is the main vehicle for the supply of nourishment to the corneal epithelium and for removal of detritus. The movements of the lids

replenish the integrity of the tear film and, if the interblinking time is prolonged more than half a minute, breaks in the tear film may appear (the so-called tear break-up time). Viewed anteriorly in vivo, the cornea is a meniscus elliptical in shape because of the greater extension of the less transparent limbus above and below it. Therefore, the vertical corneal diameter is smaller than the horizontal diameter (10.6 mm and 11.7 mm respectively in males); in females, each is 0.1 mm smaller. The anterior curvature of the cornea (radius of curvature 7.8 mm) is greater than that of the sclera (radius of curvature 11.5 mm). Nevertheless, the cornea does not protrude much beyond the scleral surface, because of the flattening of the anterior sclera and peripheral cornea and the sinking effect of the external scleral. In the central or optical zone (approximately 4 mm in diameter), the two surfaces of the cornea are parallel, and the cornea is nearly spherical except for a small amount of astigmatism (the surface is more curved in the vertical than in the horizontal meridian), which gives it a toric form.

Viewed posteriorly, the cornea is circular, with a diameter of 11.7 mm and with an average radius of curvature of 6.5 mm. Measured by optical methods, the cornea in vivo is 0.52 mm thick centrally with little difference between males and females. Towards the periphery, the cornea thickens to 0.97 mm and merges with the conjunctiva, episclera, and sclera. The weight of the freshly excised cornea is approximately 180 mg and the specific gravity is 1.052.

Structurally, the cornea consists of: (1) Epithelial layer with its basement membrane; (2) Stroma with its anterior modified zone of Bowman; (3) Descemet's membrane, which in fact is the basement membrane of the corneal endothelium; and (4) Endothelium (Mesothelium).

- **Corneoscleral Limbus**

The limbus is the gray transitional zone between the transparent cornea anteriorly and the opaque, white sclera Posteriorly, Fig [2-1]. It is here the smaller corneal curvature merges with the greater curvature of the sclera; this region is often referred to as the corneoscleral sulcus. Unlike the circular profile of the posterior corneal periphery, the anterior cornea is horizontally elliptical in shape. The sclera therefore extends forward in the superior and inferior regions in the

medial and the lateral aspects. This gives rise to the slightly wider zone of the limbus in the vertical plane (2 mm) than in the horizontal plane (1.5 mm). The transitional zone of the limbus is composed of both scleral and corneal elements, the contribution of each varying from superficial to deep regions and also in the various sectors around the circumference of the limbus. The limbus can be divided into three separate zones.

The anterior limbus is the part of limbus consisting of the conjunctival epithelium and the stroma that contains the episcleral and subconjunctival vascular plexuses and loose fibrous tissue of the episclera.

The mid-limbus consists of compact corneoscleral tissue and traversed by the veins of the deep and intrascleral plexus and by small arterioral channels and nerves.

The inner deep limbus contains the trabecular meshwork and Schelmm's canal, as well as related arterial and venous plexuses. The deep limbus contains: (1) Schlemm's canal, collector channels, and the arterial plexus; (2) Trabecular meshwork; (3) Scleral spur and Scleral roll; and (4) Line of Schalwbe.

(1) Schlemm's canal: The canal of Schlemm is an annular structure of about 36 mm circumference in the human eye, Fig [2-2 & 2-3]. Located in the inner part of the limbus, it is supported on its inner aspect by the trabecular meshwork. Anteriorly, it is bound by the compact scleral tissue; posteriorly, it lies against the main mass of the corneoscleral trabeculae. Laterally, the canal is bordered by the scleral spur and scleral roll, and medially it is limited by the approximation of the first trabecular sheet with the compact corneoscleral tissue of the limbus. The lumen of the canal is usually an elongated, slit-like opening that lies parallel to the corneoscleral trabeculae. Its dimensions vary from eye to eye; in the adult eye, when a single lumen is present, it measures 200 to 500 μm in the meridional axis and 10 to 25 μm in the opposite axis; it is generally smaller in children. In some instances, the canal may be triangular in

shape with the base of the triangle lying against the scleral spur, where it measures 50 μ in width, whereas the apex narrows medially to 5 or 10 μm.

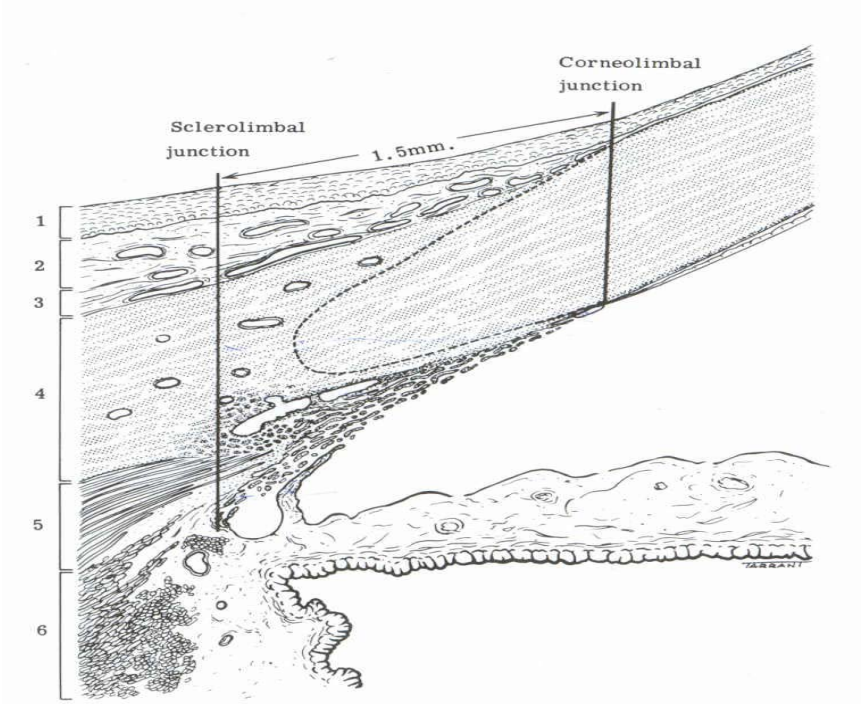

Figure 2-1: Limbus Structures 1. Conjunctiva. 2. Conjunctival stroma. 3. Tenon's capsule and episclera. 4. Limbal or corneosclaeral sroma containing intrascleral plexus of veins and collector channels from Schlemm's canal. 5. Meridional portion of ciliary muscle. 6. Radial and circular portions of ciliary muscle (from Tripathi and Tripathi [10]).

Aqueous humor is drained away from the canal of Schlemm, Fig [2-2] by three venous plexuses: the deep intrascleral, mid-intrascleral, and episcleral and subconjunctival. The lumen of the canal is connected to the deep scleral plexus by 25 to 35 collector channels distributed unevenly around the circumference of the canal. The channels are relatively wide when they arise at the canal (diameter, 20-90 μm), but become narrower as they anastomose with the venous channels.

The collector channels join the deep scleral plexus, which is made up of fine branches of the anterior ciliary veins. The deep scleral plexus, in turn, is connected to the mid-intrascleral and episcleral plexuses. The mid-intrascleral plexus is formed by a large interconnecting venous network in the limbal sclera; in addition to receiving blood from the deep scleral plexus, it drains

the ciliary venous plexus. Posteriorly, the intrascleral plexus drains into the episcleral plexus and finally into the anterior ciliary veins, Fig [2-3]. A few vessels, known as aqueous veins, varying in number from 2 to 8, arise from the canal of Schlemm and directly join the episcleral plexus. A variable amount of aqueous humor reaches the episcleral veins directly via the aqueous veins. Where an aqueous vein joins a blood vessel, the aqueous humor and blood do not mix immediately, but flow in parallel streams to give a laminated aqueous vein.

(2) Trabecular Meshwork: The trabecular meshwork is located in the inner limbus, Fig [2-2], which is limited by the ring of Schwalbe anteriorly and by the scleral spur and roll posteriorly. Since the trabecular meshwork is composed of a number of superimposed fibrocellular sheets, it presents a trabeculated and reticular appearance. It surrounds the eye in an annular shape and forms a three-sided prismatic band. The base is connected posteriorly with the scleral spur, the

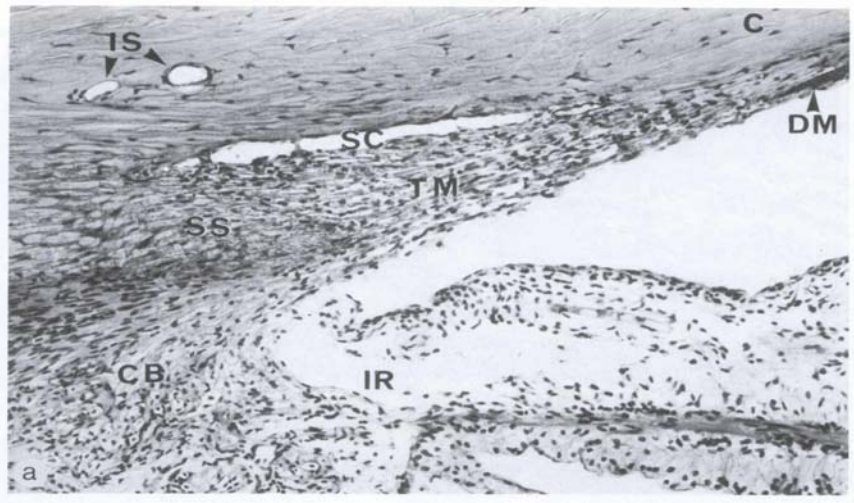

Figure 2-2: Drainage system of eye. (a) SC- Schlemm canal, (b) TM- Trabecular Meshwork, (c) C- Cornea (d) IS- Interscleral vascular channels (e) DM –Descemet's membrane, (f) SS- Scleral spur, (g) CB- Ciliary body, (h) IR- Iris (From Tripathi and Tripathi [10]).

anterior face of the ciliary body, and the iris root (hence the demarcation of the corneoscleral trabeculae, the uveal trabeculae, and the iris processes). The apex terminates anteriorly in the deep corneal lamellae. At the base, the number of trabecular sheets varies from 12 to 20, but toward the apex they are reduced to 3 to 5 layers. The outermost trabecular sheet borders the

tissues of Schlemm's canal; the inner aspect of the trabecular meshwork directly borders on the anterior chamber, Fig 3. For descriptive purposes, the meshwork can be divided into: iris

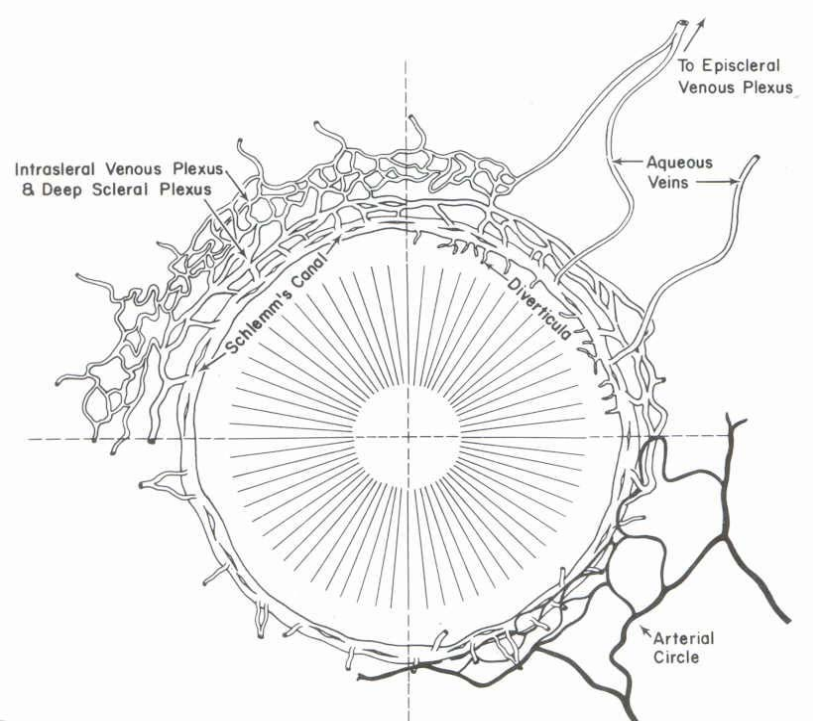

Figure 2-3: Canal of Schlemm and its communication with collector channels, aqueous veins and intrascleral venous plexus. (from Triapthi and Tripathi [53]).

processes or "pectinate" fibers, uveal trabeculae (also called ciliary, ciliocorneal, or uveocorneal trabeculae), corneoscleral (also called sclerocorneal or scleral) trabeculae and juxtacanalicular meshwork (JCM).

The iris processes are large, wide bands that arise from the anterior surfaces of the iris and join midway in the inner uveal trabeculae. The uveal trabeculae represent a tendinous extension of the ciliary muscle cells, which generally terminate below the scleral spur in man, but may continue for a variable distance in other species. The corneoscleral trabeculae are flattened, perforated sheets, the individual layers being 5 to 12 μm thick in the mid-region. Morphologically, these are similar to the anterior or outer uveal sheets and are oriented similarly, lying in a circumferential plane parallel to the surface of the limbus. In meridional sections, they appear as superimposed beams. The corneoscleral trabeculae are connected posteriorly to the

sloping antero-medial border of the scleral spur. In man, their number may vary from 8 to 15 layers, measuring from 120 to 150 μm in total thickness. The juxtacanalicular meshwork is permeated by an interconnected and complex network of apparently open pores having typical diameters in the range of 0.1 to 1.0 μm. The pores of JCM are supposed to be filled by an extracellular gel.

The open spaces in the trabecular meshwork result from the spatial separation of superimposed trabecular sheets; these spaces vary from 0 to 8 μm in size. The spaces communicate through perforations or stomata in individual trabecular sheets, i.e. intra-trabecular spaces, varying in size from 25 to 75 μm in the uveal meshwork and from 2 to 20 μm in the outer corneoscleral meshwork [10]. The perforations in the trabecular sheets are not superimposed in succeeding layers, but rather communicate with each other through tortuous pathways. Collapse of the trabecular meshwork, as occurs in hypotony, thus reduces the effective area of the openings. Both the uveal and corneoscleral meshwork have negligible resistance because of their bigger pore size. It is believed that the tortuous flow passage from the JCM accounts for the most of the flow resistance [13,14] because of its very small pore size (~1.0 μm) [15] and the presence of the extra-cellular matrix gel in the open spaces. The porosity of the meshwork is increased when the trabeculae are separated, as occurs with the contraction of the ciliary muscle and the posterior pull of the scleral spur. Such mechanisms are important in the treatment of glaucoma.

(3) Scleral spur and scleral roll: The scleral spur is a firm, fibrous, wedge-shaped ridge or projection from the inner aspect of the anterior sclera and is oriented circumferentially in the inner limbus.

(4) Line of Schwalbe: A prominent anterior border ring of the trabecular region, called the line of Schwalbe, is seen in only about 15-20% of human eyes. The line of Schwalbe consists of regular

collagen fibrils intermixed with elastic fibers, both being oriented parallel to the limbus, somewhat similar to the uveal trabeculae.

2.1.2.2 Uveal Tract

The uveal tract forms the pigmented vascular tunic of the eye. It may be divided topographically into three regions [10]: (1) the choroid, (2) the ciliary body, and (3) the iris.

(1) The Choroid: The choroid, a soft, brown vascular tunic, is the posterior part of the uveal tract that extends from the edge of the optic nerve to the ora serrata and provides nourishment for the outer retina.

(2) The Ciliary Body: The ciliary body is an anterior continuation of the choroid and of the retina and, as such, is divisible into uveal and neuro-epithelial portions. The ciliary body forms a circumferential, asymmetric girdle, slightly narrower on the nasal side and in the upper part (4. 2 to 5.2 mm, respectively) than on the temporal side and lower part (5.5 to 6.3 mm, respectively).

(3) The Iris: The iris is the most anterior portion of the uveal tract and forms a delicate diaphragm between the anterior and posterior chambers of the eye. It has a central aperture called the pupil, which is located slightly nasal from the center and controls the amount of light entering the eye. It also provides communication for the free flow of aqueous humor from the posterior into the anterior chamber. The iris is thickest close to the pupillary zone in the region of the collarette and thinnest (0.5 mm) and weakest at its root, from which it can easily be torn surgically or in contusion injuries (irido-dialysis). The major portion of the iris rests on the anterior surface of the lens. In the absence of support from the lens, the pupillary plane falls back, the anterior chamber deepens, and the iris becomes tremulous (irido-donesis) during the movements of the eye.

The color of the iris, which varies in different individuals, depends upon the amount of pigment in the stromal cells. The stromal pigmentation increases rapidly during the first year of life, and hence many infants who were born blue-eyed gradually lose the lightness of their irises. An iris devoid of tromal pigmentation, but with a normally pigmented bi-layered epithelium, will

also appear blue. In the event of pigment deficiency in the iris epithelium, the red fundal reflex gives the iris a pink color.

The diameter of the iris is about 12 mm. The anterior surface is divided into a central (pupillary) zone and a peripheral (ciliary) zone. The junction of these two zones is marked by the collarette (0.6 mm thick and 1.5 mm from the pupillary margin) and the embryonic location of the minor circulus iridis which gives rise to the embryonic pupillary membrane.

2.1.2.3 The Retina

It refers to all of the tissues derived from the optical vesicle and thus it includes the epithelial linings of the ciliary body and of the iris. The retina, with a surface area of some 266 sq. mm is a thin, delicate layer of nervous tissue which has two components: the sensory layer, derived from the inner wall of the optic vesicle, and the pigment epithelium which develops from the outer wall of the optic vesicle. Two layers normally remain in contact with each other, being held only by a matrix. The pigment epithelium is firmly attached to the choroids through Bruch's membrane. As there is no specialized attachment between the sensory retina and the pigment epithelium, the sensory layer readily detaches both in pathological conditions and postmortem changes.

2.1.3 Anterior Chamber

The anterior chamber of the human eye has an approximately ellipsoidal shape. Its boundaries are formed anteriorly by the inner surface of the cornea and peripherally by the inner surfaces of the trabecular meshwork. On the posterior aspect, the chamber is limited by the anterior surface of the iris and the pupillary portion of the anterior lens surface. On the lateral aspect, it ends in the anterior face of the ciliary body, where the anterior and posterior boundaries meet, and where the apex of the angle of the anterior chamber is located. Whereas the corneal endothelium forms a complete covering for the chamber, the anterior surface of the iris, the anterior face of the ciliary body, and the trabecular meshwork do not have a complete cellular

covering; the anterior chamber thus communicates directly with the extracellular spaces of these structures.

The size, shape, and depth of the anterior chamber are determined by the curvature of the cornea, the shape of the iris, and the size and position of the lens. Since the plane of the iris is not completely horizontal, because of the forward location of the lens, the pupillary portion of the iris is displaced 0.6 to1 mm anteriorly with respect to the iris root. This forward displacement of the pupillary plane, however, is smaller in myopic than in hypermetropic eyes. The forward inclination of the iris and the pupillary sphincter produces a ball-valve action, which offers some resistance to flow of aqueous humor from the posterior to the anterior chamber. During forceful contraction of the sphincter muscle, the aqueous pressure in the posterior chamber may cause an anterior bowing of the peripheral iris that produces "iris bombe". Pupillary dilatation or iridectomy may reverse this situation.

The diameter of the anterior chamber varies between 11.3 to 12.4 mm and is slightly greater than that of the cornea. Because of the corneal curvature, the chamber is deepest centrally and shallower peripherally near the angle. The diameter of the cornea and the depth of the anterior chamber are related. The chamber depth is slightly greater in males than in females, but in both it decreases with advancing age as the size of the lens increases. As a rule, the anterior chamber is shallower in hypermetropes and deeper in myopes; on average, the central depth measures 3.15 mm (range, 2.6 to 4.4 mm). The depth of the anterior chamber in the two eyes of the same individual is almost equal.

2.1.4 Posterior Chamber

The aqueous humor is secreted by the ciliary bodies in the posterior chamber, which is bound anteriorly by the pigment epithelium of the posterior iris; anterolaterally by the junctional zone of the iris and ciliary body; and anteromedially by the contact of the iris with the lens. Aqueous humor gains entry into the anterior chamber from the posterior chamber via pupil. The equatorial portion of the lens forms the medial boundary of the posterior chamber. Posteriorly, the

anterior face of the vitreous limits it. Laterally, the chamber is bounded by the ciliary body with its processes and valleys, and it may extend back to the point of contact between the anterior face of the vitreous.

2.1.5 Vitreous Cavity

The vitreous, which occupies almost four-fifth of the volume of the globe, is a clear, transparent, avascular, gel-like structure of semi-solid consistency. It is undoubtedly the most delicate connective tissue structure of the body. Even after fixation, the vitreous body is incapable of maintaining its shape, and the shape of the vitreous cavity, which is spheroidal posteriorly, determines its outline. The large volume of the vitreous body provides support for the intraocular structures including the lens and, in conjunction with the aqueous humor and the fibrous tunics of the eye, helps to maintain the intraocular pressure.

The vitreous body in the human eye weighs about 4 gm and its volume is approximately 4 ml; it consists of 99 % water. The specific gravity (1.0053 to 1.0089) is only slightly higher than that of water, and its refractive index (1.334) is slightly lower than that of aqueous humor. Its viscosity is almost twice than that of water, but the osmotic pressure is very close to that of aqueous humor.

2.1.6 The Lens

The human lens is a transparent, biconvex, elliptical, semi-solid, avascular structure with smooth, shiny surfaces. In infants and children, the lens is soft but the central or nuclear portion becomes firmer with advancing age. The lens is located between the iris and the vitreous, with its anterior central region exposed by the pupil. The posterior surface of the pupillary part of the iris glides over the anterior surface of the lens, Fig. [1-1]. In eyes with a narrow anterior chamber angle and shallow anterior chamber, the iris/lens contact may be wider and firmer causing interference with the passage of the aqueous humor from the posterior to the anterior chamber, and may be a causative factor in angle-closure glaucoma.

Peripherally, the equatorial region of the lens (rounded junction of its anterior and posterior surfaces) projects into the posterior chamber and is separated from the ciliary body by a 0.5 mm wide circumlental space. The lens is supported by a system of zonules (suspensory ligaments) which extend from the ciliary epithelium to a 2.5 mm circular zone around the lens equator; 1.5 mm of this is on the anterior, and 1 mm on the posterior lens surface. When traction is applied, as during relaxation of the ciliary muscles, the zonule induces dentate processes on the otherwise smooth, rounded lens equator.

The shape of the human lens in vivo is, to some extent, dependent upon the tension of the suspensory ligament, which in turn, is dependent upon the tone of the ciliary muscle and the inherent elasticity of the lens tissue. The shape of the lens in situ, therefore, differs from that of the excised lens. The lens is almost spherical at birth and flattens markedly during the first two years of life. In adults, the anterior surface is a flattened ellipsoid with an average radius of curvature of 10 mm (range, 8 to 14 mm). The geometric center of this curve constitutes the anterior pole, which is about 3 mm distant from the central posterior corneal surface (i.e., the depth of the anterior chamber). The posterior lens surface is curved more steeply, with an average radius of 6mm (range, 4.5 to 7.5mm). At birth, the equatorial diameter is about 6.25 mm and 9 to 10 mm in adult life. The axial (sagittal) diameter, which joins the anterior and posterior poles, varies markedly with age and accommodation. The axial diameter is approximately 3.5 to 4 mm in the newborn and in young children; between the ages of 20 and 50 years, it changes little; in the extremely old, it gradually increases to almost 5 mm.

2.2 Aqueous Humor Particles

2.2.1 Pigment Granules

Pigmentary Glaucoma and Pigment Dispersion Syndrome (PDS) is a condition of defective eye found most commonly in young males [2]. The symptom of these diseases is the deposition of pigment particles (melanin granules) on the ocular tissues of the eye. Defect of the iris pigment epithelium causes the liberation of pigment particles from the pigment layer of the

iris surface. The previous mechanistic theory suggests that rubbing of peripheral iris with lens surface or anterior zonular packets causes liberation of melanin granules from the iris [2]. Most of the melanin granules are released from the posterior surface (surface towards the posterior chamber) of the iris and enter into the anterior chamber with the aqueous humor. There is contradiction and variation in documented information about the size, density and concentration of these particles in aqueous humor. Its diameter is the order of 0.5-1 μm [24] and density is about 1700 Kg/m^3 [22], which is used for all simulations of pigment particles in the present model. It is reported by Kuchle et al. [25] in their experimental results for eyes with PDS that 250 μL of aqueous humor contains approximately 9700 melanin granules.

Pigment particles have the property of stickiness and they can get adhered to the posterior part of the cornea under specific circumstances, which causes the accumulation of particles on the corneal surface in some distinctive shape commonly known as Krukenberg Spindle (KS), Fig [2-4a & 2-4 b]. It is found that distribution of the pigment granules on the corneal surface is both extra and intra-endothelial. It is reported in literature that corneal endothelium possess phagozytic properties. According to previous hypothesis of formation of KS, pigment particles first adhere to the irregularities on the endothelial surface of cornea and later on the granules are phagozytized and accumulated in the endothelial cells that leads to the formation of KS structures [2]. Due to smaller size and volume of the pigment particles vision is generally not obstructed by formation of smaller KS, but all patients with KS should be considered as glaucoma suspects [26]. As KS structures are indication of pigment dispersion in the anterior chamber, there are possibilities of clogging of the pores of TM with pigment particles in eyes with KS structures, and thereby increasing the IOP [27].

2.2.2 Red Blood Corpuscles (RBC)

Red blood cells or erythrocytes are one of the important constituents of the blood. In normal conditions one cubic millimeter of blood contains 4-5 millions of erythrocytes [28]. Fresh

red blood cells are less than 120 days old and have the capabilities of squeezing to come out from the anterior chamber through the TM-drainage system [22]. The diameter of these red blood cells lies in the range of 6.7-7.7 μ m and density is about 1000 Kg/m^3 [22]. While ghost cells are more than 120 days old and loses its pliability to get deformed. They are much denser than fresh red cells (1500 Kg/ m^3) [22]. They take rigid spherical shape and due to incapability of deformation they tend to get tucked in the TM and clog the drainage system of the eye.

Commonly erythrocytes are not found in the anterior chamber, but the damage of the intra-ocular tissues or breakdown of the blood-ocular barrier causes the accumulation of the blood in the anterior chamber. This hemorrhage in the anterior chamber with accumulation of blood is very serious and challenging problem commonly referred as Hyphema, Fig [2-4c]. Tiny hemorrhages are visible in form of erythrocytes floating and circulating in the aqueous humor. Slightly larger amounts of blood settle as variously shaped masses on the surface of the iris and lens. Still larger hemorrhages gravitate to the inferior aspect of the anterior chamber, producing a grossly visible layered Hyphema. For most severe hemorrhages impaired circulation of AH causes clotting of blood and trabecular blockage with normal sickle erythrocytes. Ophthalmologists grade four categories of Hyphema- Grade-1. Hyphema in which layered blood occupied less than one third of the anterior chamber. Grade-2. Hyphema consists of blood filling one third to one half of the anterior chamber. Grade-3 Hyphema is layered blood filling one half to less than total. Grade-4 includes total clotted Hyphema, often referred as Blackball Hyphema, [4]. Clotting of TM increases the resistance to outflow and consequently leads to increase of IOP, which can go up to 50 mm of Hg in some severe cases of Hyphema [30]. Continued bleeding and elevated IOP for a long time may lead to onset of glaucoma, optical atrophy and sometimes corneal blood staining (in case of total Hyphema), which results in final poor vision [4].

One of our objectives is to formulate a model to analyze the sedimentation of erythrocytes in anterior chamber, when they are not able to come out due to blockage of TM. The

sources of bleeding are tear in anterior face of the ciliary body; disruption in arterial circle of the iris [30] or sometimes blood-corpuscles enters into the anterior chamber from some sources of posterior part of the eye through the pupil. We aim to identify the concentration of the particles at different locations inside the eye released from different sources of bleeding.

2.2.3 White Blood Corpuscles (WBC)

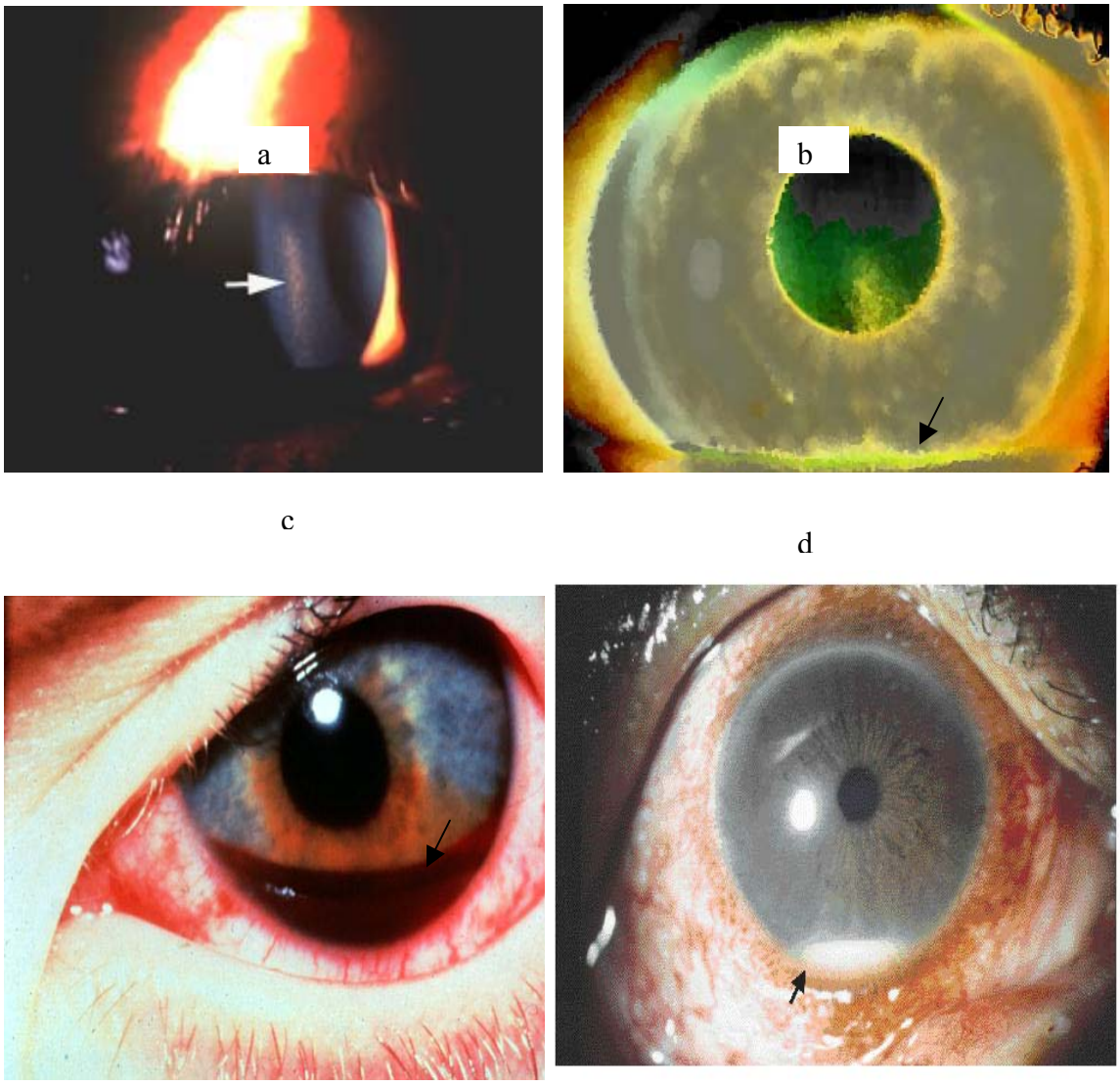

Figure 2-4: (a) KS as a vertical spindle on the corneal surface [31]. (b) KS formation due to the accumulation of pigment particles at lower portion of the corneal surface. [32](c) A typical Hyphema. [32](d) Hypopyon (sedimentation of leucocytes at the bottom of the anterior chamber) [32].

WBC or leucocytes are rounded slightly flattened, nucleated cells, mainly protoplasmic in composition, and possessed of contractile power. There average size is about 10 microns [28] and they are present in blood in much smaller numbers than the red blood corpuscles. The density of leucocytes is close to the fresh red blood cells [22]. They have property of stickiness, so they can either clump together or stick with the ocular tissues. WBC are complete cells because they contain a nucleus and other vital organelles. There are two types of WBC, which are distinctly recognized: (a) the agranular Leucocytes, which include Lymphocytres and Monocytes (b) the granular Leucocytes include Neutrophiles, Eosinophils and Basophils each of which have their own specific granules. The average number of leucocytes in a normal adult varies between 5000and 9000 per mm^3 . In disease states the number of leucocytes increase or decrease. Neutrophils constitute 60 to 75 % (4200-5200/mm^3) of the White blood cells. They are 12 to 15 μ in diameter. Eosinophils constitute 2 to 4 % (70-210/mm^3) of circulating white blood cells. The cell is 12 to 15 μ in diameter and usually has bi-lobed nucleus. Basophils are less than 1 percent (35-70 mm^3) of the circulating white blood cells and usually found with diameter in the range of 12 to15 μ, but they may be smaller. Lymphocytes constitute 20 –45 % (1400-3150/mm^3) of WBC and vary widely in size. Small lymphocytes are approximately 7 to 10 μm in diameter and larger ones could have diameter up to 20 μm. Monocytes have 2 to 10 % sharing in WBC (140-700/mm^3) and having size approximately 15 to 25 μm in diameter [34].

The life span of white blood cells is considered to be shorter than that of red blood cells. The exact life span is, however, not known, because these cells normally leave the vascular system to enter tissue spaces to perform their special functions. Aging leucocytes are removed from the circulation by the macrophages located in the liver or spleen. The leucocytes wage continuous war with unwanted visitors, such as bacteria, viruses or fungi or even abnormal cells of the body [34].

With malignant diseases of the bone marrow, the number of leucocytes is greatly increased. These leucocytes are immature cells, which are not able to function. They are produced by the bone marrow and in their chaotically growing state they suppress the erythrocyte and thrombocyte cells developing in the bone marrow. An increase (leucocytosis) in the total number is mainly manifested with inflammations triggered off by bacteria or fungi [34]. The presence of white blood corpuscles in the anterior chamber indicates that the patient is suffering from inflammation of uveal tissues, known as Uveitis [22]. When accumulation of leucocytes is mild and typically in triangular shape, then it is known as Keratic Precipitates. These Keratic Precipiates do not affect vision generally, but when they accumulate in sufficient amount at the bottom of the anterior chamber, a layered white structure is formed, which is known as Hypopyon [5], Fig [2-4d]. These Hypopyon are indication of severe intraocular inflammation inside the anterior chamber, which may lead to damage of ocular tissues and consequently leads to loss of sight.

CHAPTER 3. COMPUTATIONAL MODEL

3.1 Mathematical Model

3.1.1 Geometrical Model of the Rabbit's Eye

In the present work, attention is focused on a rabbit's eye, whose shape and geometry are slightly different from those of the human eye. The depth of the anterior chamber of the rabbit eye is in the range of 5-6 mm and diameter in the plane of the iris root is 12 mm. The iris, which is the front extension of the ciliary body, has a slightly elliptical shape with a vertical axis 11-12 mm long, Fig [3-1a & 3-1c]. The pupil changes its diameter depending on the amount of the light falling on the eyeball. It has been experimentally found that iris-tissue is incompressible and linearly elastic under small deformations [7]. The biconvex crystalline lens located at the back of the anterior chamber is enclosed in a capsule suspended by the ciliary body with zonular fibers. AH secreted in the posterior chamber by the ciliary body enters the anterior chamber through the small gap between the iris and lens which is estimated to be few microns ($\approx 10\ \mu$) wide [23]. In this paper, the anterior chamber is modeled as a hemispherical geometry with a diameter of 6 mm, Fig. [3-1b]. The iris is modeled as a rigid surface at the bottom of the hemispherical anterior chamber with a circular aperture at the center (the pupil) from which the flow enters the anterior chamber of eye. It is assumed that neglecting the curvature of the iris surface and modeling it as a plane annular surface will incorporate insignificant error in the simulation results. Since the velocity profile and the flow pattern in the anterior chamber is buoyancy driven it is unlikely that the inlet profile will have significant effect. Therefore, for simplicity we have assumed a flat inlet velocity profile of AH through the pupil (of radius 2.5 mm unless otherwise specified).

The cornea is a vascular and transparent tissue with thermal properties close to that of water. It is modeled as a rigid hemispherical shell with a constant temperature (T_C). The temperature drop between the iris and the cornea (generally considered to be in the 2-4 ^0C for the open eye) provides the buoyant force mechanism to drive the AH. This temperature drop is

treated as a parameter in the present study, and is varied between $0.02\,^{0}C$ (eye lids closed) to $6\,^{0}C$. The AH is assumed to be linear viscous liquid with properties close to those of water. The properties used in the present simulations are listed in Table [1-1].

Table 1-1. Properties of AH and Ocular tissues used in simulations.

Properties	Density (ρ, Kg/m^3)	Thermal conductivity (K, W/m-K)	Specific heat (C_p, J/Kg-K)	Dynamic viscosity (μ, Kg/ms)	Volume expansion coefficient (β, 1/K)
Aqueous Humor	1000.0	0.60	4182	0.001	0.0003
Cornea	1000.0	0.58	4200		
Lens	1000.0	0.40	4200		
Ciliary Body	1000.0	0.58	4200		
Iris	1000.0	0.58	4200		

As noted earlier, the TM is treated as annular porous zone at the bottom of the anterior chamber. It is assumed to have a thickness of 1 mm and an annular radius of 1.2 mm. The part of the TM immediately adjacent to the anterior chamber is the Uveal meshwork followed by the Corneoscleral meshwork. This part of the meshwork has negligible resistance to outflow due to its bigger pore size. We treat this part of TM as a porous jump interior surface at the entry of the annular porous zone with 0.2 mm thickness and a resistance coefficient corresponding to 100 microns pore size. The porous jump interior surface is a thin porous medium of finite thickness over which the pressure change is defined as a combination of Darcy's Law and an additional inertial loss term, Fig [3-1d]. The pressure gradient across the porous jump surface is given by equation (4) and the coefficients of the equation are used corresponding to porous bed of 0.5 void fraction and 100 microns mean particle diameter. The remaining part of TM is treated as a porous zone (packed bed) with a specified average pore size and a void fraction of 0.5. The average pore size is varied from 100 microns to 0.6 microns to understand the effect of the pore size on the IOP of the eye.

3.1.2 Governing Equations

The steady three-dimensional incompressible Navier-Stokes equations are solved with the inclusion of buoyancy terms for natural convection [34,35] and Darcy pressure drop terms in the porous zone. The density appearing in the buoyancy term is assumed to satisfy the Bousinesq approximation. The resulting non-dimensional forms of the momentum and energy equations are

Momentum equation:

$$U_j \frac{\partial U_i}{\partial X_j} = \frac{1}{\mathrm{Re}_D}\left(\frac{\partial^2 U_i}{\partial X_j \partial X_j}\right) + \delta_{im}\left(\frac{Gr_D}{\mathrm{Re}_D^2}\right)\theta + (\delta_{im} - 1)\frac{\partial P}{\partial X_i} - P_i \quad \text{.....(1)}$$

where m represents the index of the co-ordinate direction in which gravity is acting.

where P_i is the momentum sink term added in the momentum equation for porous zone. The second term in right hand side of equation (1) (buoyancy term) is included in the momentum equation only for the co-ordinate direction in which body forces are acting (gravity forces). For the other two co-ordinate directions this term is replaced by the term ($-\frac{\partial P}{\partial X_i}$) as indicated by the equation (1).

Energy equation: $$U_j \frac{\partial \theta}{\partial X_j} = \frac{1}{\mathrm{Pr}_D}\frac{1}{\mathrm{Re}_D}\left(\frac{\partial^2 \theta}{\partial X_j \partial X_j}\right) \quad \text{.....(2)}$$

Continuity equation: $$\frac{\partial U_j}{\partial X_j} = 0 \quad \text{.....(3)}$$

The following non-dimensional variables are used in Eqs. (1)-(3):

$$X = \frac{x}{D}, Y = \frac{y}{D}, Z = \frac{z}{D} \; ; \quad U = \frac{u}{U_{in}}, V = \frac{v}{U_{in}}, W = \frac{w}{U_{in}} \; ; \quad \theta = \frac{T - T_C}{T_{in} - T_C} ; P = \frac{p}{\rho U_{in}^2}$$

where T_{in} is the temperature of AH at inlet and T_C is the corneal temperature. The characteristic speed U_{in} is 2.12 μ/s and the characteristic length D is the diameter of the iris surface in the

(a)

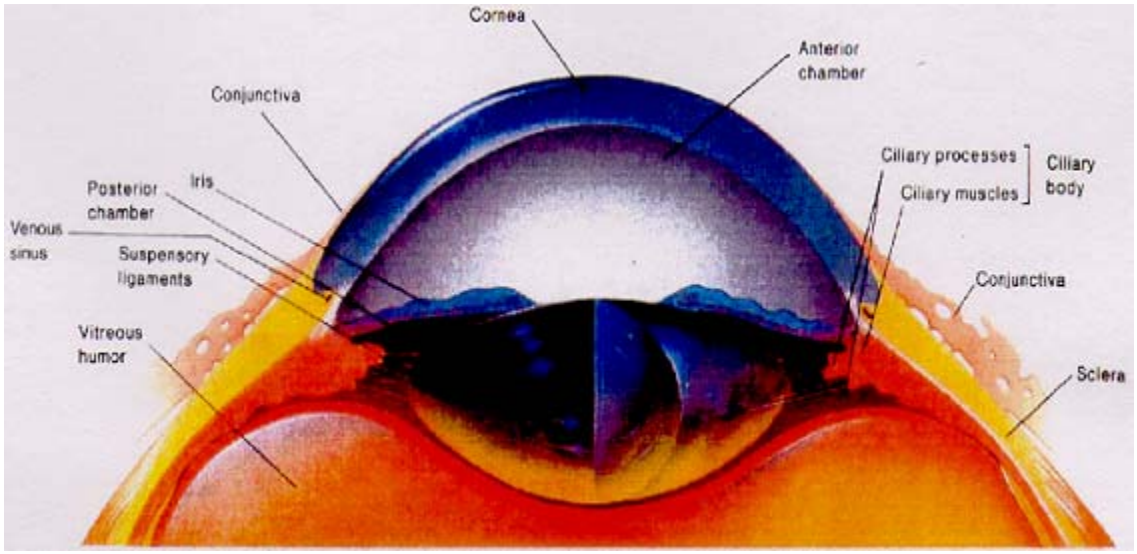

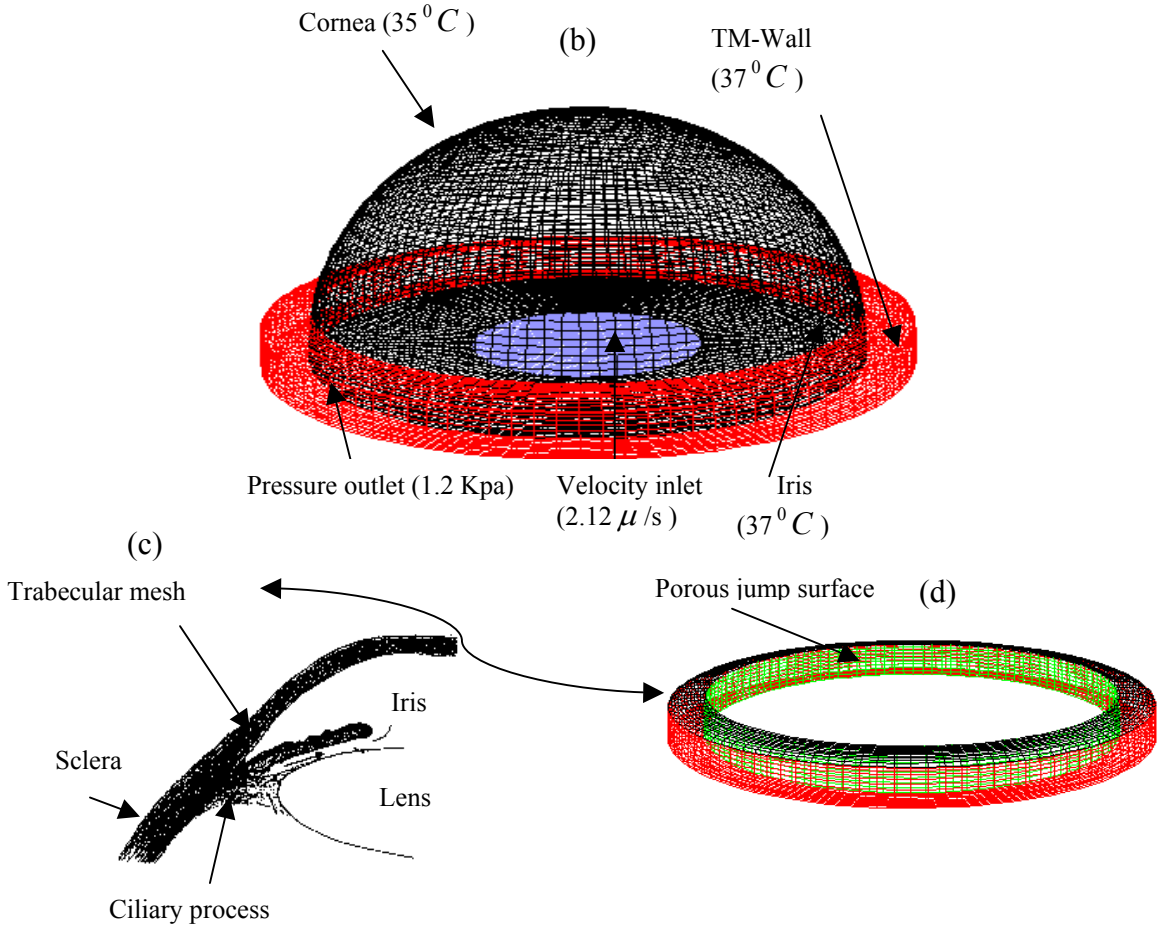

Figure 3-1: (a) Schematic of a Rabbit's eye, (from Mullenax [36]). (b) Geometrical model used for the simulation. (c) Details of the anterior chamber (from Huillier and Sbirlea [37]). (d) Model of TM.

model, which is 12 mm. The important non-geometrical parameters that appear in the governing equations, and their values of interest in the present study are:

Re_D : 0.025 (Reynolds number, Re = $\frac{\rho UD}{\mu}$)

Pr_D : 7.0 (Prandtl number, Pr = momentum diffusivity / thermal diffusivity = $\frac{C_p \mu}{K}$)

Gr_D : $1.017 * 10^2$ -$3.051 * 10^4$ ($\Delta T = 0.02^0 C - 6^0 C$)

(Grashof number, Gr = buoyancy force / viscous force = $\frac{L^3 \rho^2 g \beta \Delta T}{\mu^2}$)

To model the porous regions representing the TM, the momentum sink term (∇P) in the equation (1) is represented by the sum of a viscous loss term (the Darcy term) and an inertial loss term. Thus,

$$\nabla P = \frac{\mu}{\alpha} U_i + C_2 \frac{\rho}{2} |U_i| U_i \quad \text{.....(4)}$$

which is added in momentum equation in non-dimensional form as $P_i = \frac{\mathrm{Re}_D D^2 U_i}{\alpha} + \frac{C_2}{2} D |U_i| U_i$. This term is not included in the momentum equation for non-porous fluidic zone. The momentum sink contributes to the pressure gradient in the porous cell, creating a pressure drop that is proportional to the fluid velocity (or velocity squared) in the cell. The porous media model incorporates an empirically determined flow resistance in the porous region. Since the volume blockage that is present physically is not represented in the model, the velocity inside the porous medium is computed based on the volumetric flow rate, to ensure continuity of the velocity vectors across the porous medium interface. In laminar flows through porous media, the pressure drop is typically proportional to velocity. So, the viscous term (first term) in equation (4) is more important with respect to the inertial resistive term (second term). Here α is the

permeability and C_2 is the inertial resistance factor. To get appropriate values of the constants α and C_2, a semi-empirical correlation, derived from the Ergun equation [38], is used. These correlations for the permeability α and inertial resistance factor C_2 are applicable over a wide range of Reynolds number and for various packing levels, and are given as:

$$\alpha = \frac{D_p^2 \varepsilon^3}{150(1-\varepsilon)^2} \qquad C_2 = \frac{3.5(1-\varepsilon)}{D_p \varepsilon^3}$$

where D_p is the mean particle diameter of the packed bed or pore size and ε is the void fraction. The void fraction ε is defined as the volume of the voids divided by the volume of the packed bed. The range of D_p used in present study is 100-0.6 μm and the value of ε is taken as 0.5 for all simulations.

3.2 Particle Simulation

For the present simulations pigment particles are considered as spherical particles of diameter of 1 μ, RBC as particles of diameter 5 μm and WBC as particles of 10. Density of these small particles is close to water and size in few microns, so for all particle-simulations it is assumed that flow field is unaffected by particle motion, but particle motion is dominantly influenced by the flow filed. Trajectories of these discrete phase particles is predicted by integrating the force balance equations of the particle in Lagrangian reference frame. This force balance equates the particle inertia with the other forces acting on the particle. This force balance is represented in X-direction of Cartesian co-ordinates as:

$$\frac{du_p}{dt} = F_D(u - u_p) + \frac{g_x(\rho_p - \rho)}{\rho_p} \qquad \text{.....(5)}$$

and similarly in other directions, where $F_D = \frac{18\mu}{\rho_p d_p^2} \frac{C_D \,\mathrm{Re}}{24}$

Here Re is relative Reynolds number and C_D is drag coefficient of the particle, which are expressed as

$$\mathrm{Re} = \frac{\rho d_p |u_p - u|}{\mu} \qquad C_D = \frac{24}{\mathrm{Re}}(1 + b_1 \mathrm{Re}^{b_2}) + (\frac{b_3 \mathrm{Re}}{b_4 + \mathrm{Re}})$$

Here u is the fluid phase velocity, u_p is particle velocity, μ is molecular viscosity of the fluid, ρ is the fluid density, ρ_p is the density of the particle and d_p is the particle diameter. For spherical shape of the particles the constants are calculated as b1=0.196, b2=1.921, b3=0.437, b4=7185.35, Heider and Levenspiel, [39]. The first term in right hand side of Eq (5) corresponds to drag force on the particle while the second term is concerned with the gravitational force acting on the particle. The drag force on the particle is three-order magnitude greater than the gravitational force. For a typical case of particle simulation, when the fluid velocity is 1mm/s and the difference in the particle velocity from the fluid velocity is 0.1 mm/sec, the relative Reynolds number Re_P is calculated as 0.1. All the simulations are carried out with the assumption that particles have spherical shape and smooth surface.

Trajectory is predicted as

$$\frac{dx}{dt} = u_p \qquad \text{.....(6)}$$

It is assumed that all body forces acting on the particle is constant and every other force is linearized such that the trajectory equation can be rewritten in simplified form as,

$$\frac{du_p}{dt} = \frac{1}{T_p}(u - u_p) \qquad \text{.....(7)}$$

Equation (6) and (7) are solved simultaneously to determine the velocity and position of the particle at any given time. The length scale (L) for one step of particle simulation is 0.1 mm, which is the distance traveled by the particle before its motion equations are solved again and trajectory is updated. Here L is proportional to the integration time step, which is defined as

$\Delta t = \frac{L}{u_p + u_c}$ where u_p is particle velocity and u_c is the velocity of the continuous phase. The maximum number of time steps used in our simulation is 100000, after which trajectory calculation for the current particle injection is abandoned and its fate is decided as incomplete. The fate 'incomplete' is an indication that the particle is either trapped in the re-circulation region or gets adhered on ocular tissue-surface and is unable to come out from the anterior chamber. For the interaction of the particle with ocular-tissues, reflect boundary wall condition is used on ocular surfaces (corneal, iris and TM surfaces). On these ocular surfaces the constant value of coefficient of restitution (0.5) is used for both normal and tangential directions. This means that if a particle hits any ocular surface, then after the impact its velocity is reduced in magnitude to half of its previous value in both the normal and tangential direction of the wall-surface. The coefficient of restitution plays a crucial role in determining the fate of the particles after they strike the ocular surfaces of the anterior chamber. The value of coefficient of restitution chosen for the present particle simulations takes care that if the particle velocity is small in magnitude at any particular location close to the ocular surface and flow is not able to sweep away these particles, then after few impacts from the ocular surface the magnitude of velocity get reduced to very small value. The movement of the particle at that particular location will be almost negligible and it can be considered as adherence of the particle at that particular location. These are the particles, whose fate is decided as 'incomplete' as they are not capable of escaping from the anterior chamber. The accumulation of these particles is responsible for the formation of some specific structures observed in case of some eye diseases. Some commonly observed structures in the eye are Krukenberg Spindle, Hyphema or Hypopyon. The boundary between the anterior chamber and the TM of the eye is porous jump interior surface, which is used as interior wall for the simulation of small particles (diameter = 1 μm). The interior wall boundary condition facilitates the small pigment particles to enter into the pores of TM from anterior chamber without any obstruction. The pores of the TM have much smaller size (0.6-1.0 μ) compared to

the diameter of the bigger particles (RBC & WBC). So, for the particles of large size (7 μ and 10 μ m), reflect boundary condition is imposed on the interior porous jump surface to prevent the particles to come out from the pores of the TM. Escape boundary condition is imposed on the pressure outlet boundary, so that particles that did not get trapped into the pores of TM while passing through it will escape out from the solution domain. These are the representation of the particles, which escape from the anterior chamber and TM and finally drain out through the aqueous veins.

3.3 Boundary Conditions

The iris and cornea are modeled as stationary rigid boundaries, and no-slip boundary condition is imposed along these surfaces. The normal secretion rate from ciliary body is 2.5 $\mu L/\min$ and to satisfy this inlet flow rate through the pupil, (circular aperture of radius 2.5 mm), a flat inlet flow profile of 2.12 μm /s magnitude is used for all simulations except for the cases where the pupil size is varied. Since most of the flow drains out to aqueous veins passing radially through the TM, and the collector channels, the upper and lower surfaces of the annular TM are assumed to be impermeable walls (no-slip boundary condition). The pressure in the aqueous veins under normal condition is 9 mm of Hg [17], so the outlet boundary is treated as pressure outlet boundary condition with a specified pressure of 9 mm of Hg (1.2 kPa). The inclusion of the TM in the present simulation, and the incorporation of a realistic pressure outlet boundary condition, is a distinct improvement over previously reported efforts [7, 13-23].

For the temperature, the iris and the incoming flow through the pupil are specified to be at the core body temperature ($37^0 C$). The temperature of the cornea is set at constant value, which is varied from $31^0 C$ -$36.98^0 C$ to understand the importance of buoyancy in AH dynamics. The large temperature difference studied ($6^0 C$) reflects the upper end of potential temperature gradients in the eye, and may be reflective of conditions in extremely cold climates. The lowest temperature difference studied ($0.02^0 C$) represents conditions when the eye-lids are

closed, and the corneal surface is not directly exposed to the ambient. Under these conditions, buoyancy effects are likely to be relatively weaker, and the details of the inflow velocity profile through the pupil may play an increasingly important role.

3.4 Numerical Procedure

The numerical procedure is based on a control volume approach where the computational domain is divided into a number of cells or elements, and the governing equations discretized into algebraic equations in each element. The control-volume approach leads to discretization equations, which express the integral conservation of mass, momentum and energy over each control volume. The discrete values of the variables are stored at the cell-centers, but the convection terms in the descretized equation must be interpolated at the cell faces from the cell-center values. A second order upwind scheme is used for deriving the face values of different variables in the momentum and energy equations. For the pressure equation, a second order accurate descretization scheme is used. For preserving second order accuracy, a multidimensional linear construction approach is used to compute the quantities at the cell interfaces. In this approach Taylor-series expansion of the cell-centered solution about the cell centroid is used, and the face value ϕ is computed using $\phi_f = \phi + \nabla\phi.\Delta\vec{S}$ where ϕ is the cell-centered value in the upstream cell and $\Delta\vec{S}$ is the displacement vector from the upstream cell to the face centroid.

A structured multi-block solver is used for the numerical solution. The system of algebraic equations are solved using Gauss-Siedel scheme. Although the Gauss-Siedel scheme rapidly removes the high frequency errors in the solution, low frequency errors are reduced at a rate inversely related to the grid size. For computations with a large number of nodes, the solver and the residual reduction become prohibitively slow. A V-cycle multi-grid scheme is used to accelerate the convergence by applying corrections on the coarser grid-levels. The coupling between velocity and pressure is handled using the SIMPLEC-algorithm [40], which uses the

(a)

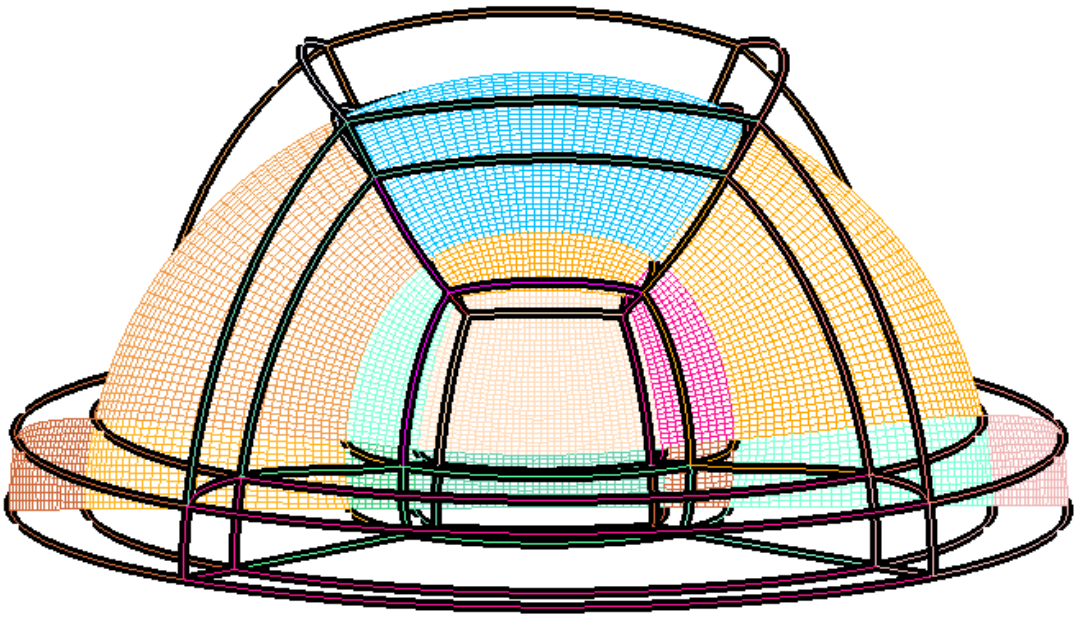

(b)

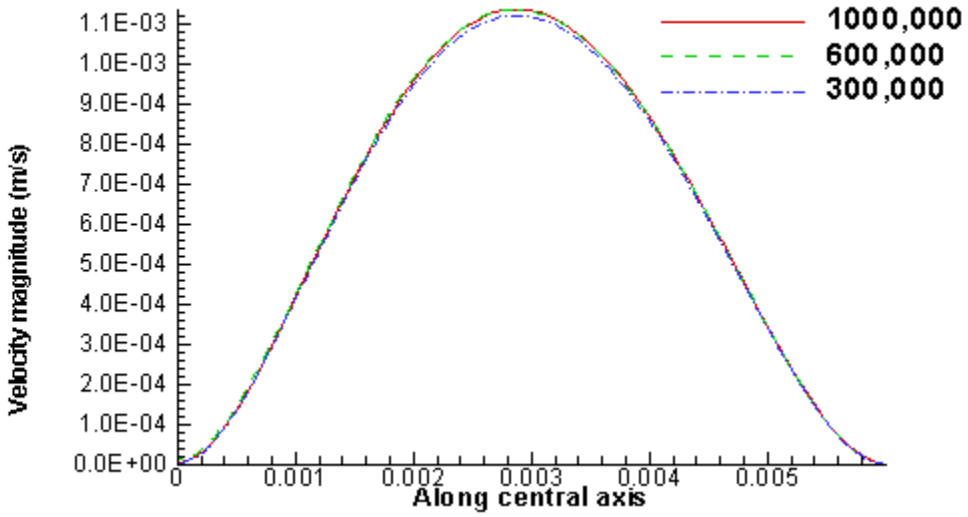

Figure 3-2: (a) Blocks of the topology and mesh in the model in vertical mid-plane (b) Velocity magnitude along the central axis of the anterior chamber for 300,000, 600,000 and 1000,000 hexahedral cells.

conservation of mass equation to derive a pressure corrector equation, and uses a pressure and velocity correction step to yield continuity satisfying velocity fields at each iteration.

In the porous medium region, the pressure drop appears as a momentum source term, which yields a loss of diagonal dominance and poor convergence rates. To avoid exacerbating convergence issues, it is critical to have high quality orthogonal grids with moderate aspect ratios. The commercial package GRIDPRO was used in the grid generation process, and only hexahedral cells of aspect ratio less than three in the computational domain is used. The entire geometry is divided into 29 blocks with 4 blocks representing the porous zone, 5 blocks located in the core of the hemispherical anterior chamber and the remaining 20 blocks defining the periphery Fig. [3-2a]. For the cases reported in this paper, 300,000 hexahedral cells are used. To demonstrate grid independence, simulations are run with 600,000 and 1000,000 cells. Less than 2 % variation in the magnitude of the maximum velocity is observed between the 300,000 cell calculation and the stalls 1000,000 cell calculation Fig. [3-2b], and justifies the use of 300,000 cells for the simulations.

CHAPTER 4. FLOW SIMULATION IN RABBIT EYE

4.1 Role of Buoyancy

In order to confirm the dominance of buoyancy as the driving mechanism for the AH dynamics, three simulations are performed for the horizontal upward-facing eye. These simulations are performed for a $2^0 C$ temperature difference between the iris and the corneal surface and $100\,\mu$ pore size of TM. The three simulations correspond to no-buoyancy, Fig. [4-1a], no inflow through the pupil, Fig. [4-1b], and combined inflow and buoyancy, Fig. [4-1c]. Without buoyancy, the magnitude of the maximum velocity is 2.12 μ m/s (which is the inlet velocity), while with buoyancy alone, Fig. [4-1b], the magnitude of the maximum velocity is 1020 μ m/s, which is nearly 480 times greater than the no-buoyancy case. With combined buoyancy and inflow, Fig. [4-1c], the maximum velocity is nearly the same (within 10%) as with buoyancy alone, Fig. [4-1b], indicating that buoyancy is the dominant driving mechanism for the AH flow. The flow patterns are quite different with and without buoyancy, with an axis-symmetric recirculation pattern in the presence of buoyancy. Without buoyancy, the flow enters through the pupil and leaves through the TM without any recirculation. For the simulation with buoyancy, a small axis-symmetric corner vortex in front of the TM is obtained.

4.2 Effect of Inlet Profile

For analyzing the effect of inlet velocity profile simulations are performed for the flat velocity profile, Fig. [4-2a], and parabolic velocity profile, Fig. [4-2b], at the inlet aperture of the anterior chamber. The line plots of the velocity magnitude along the X-axis located on the iris surface and the inlet aperture show that on the inlet aperture velocity contours follow the specified velocity profile, but no difference in velocity magnitude is observed on the iris surface for two different inlet profiles, Fig [4-2c]. Similarly no significant difference is observed in the velocity magnitude along the central axis of the anterior chamber for the two different inlet profiles. This again shows that flow field inside the anterior

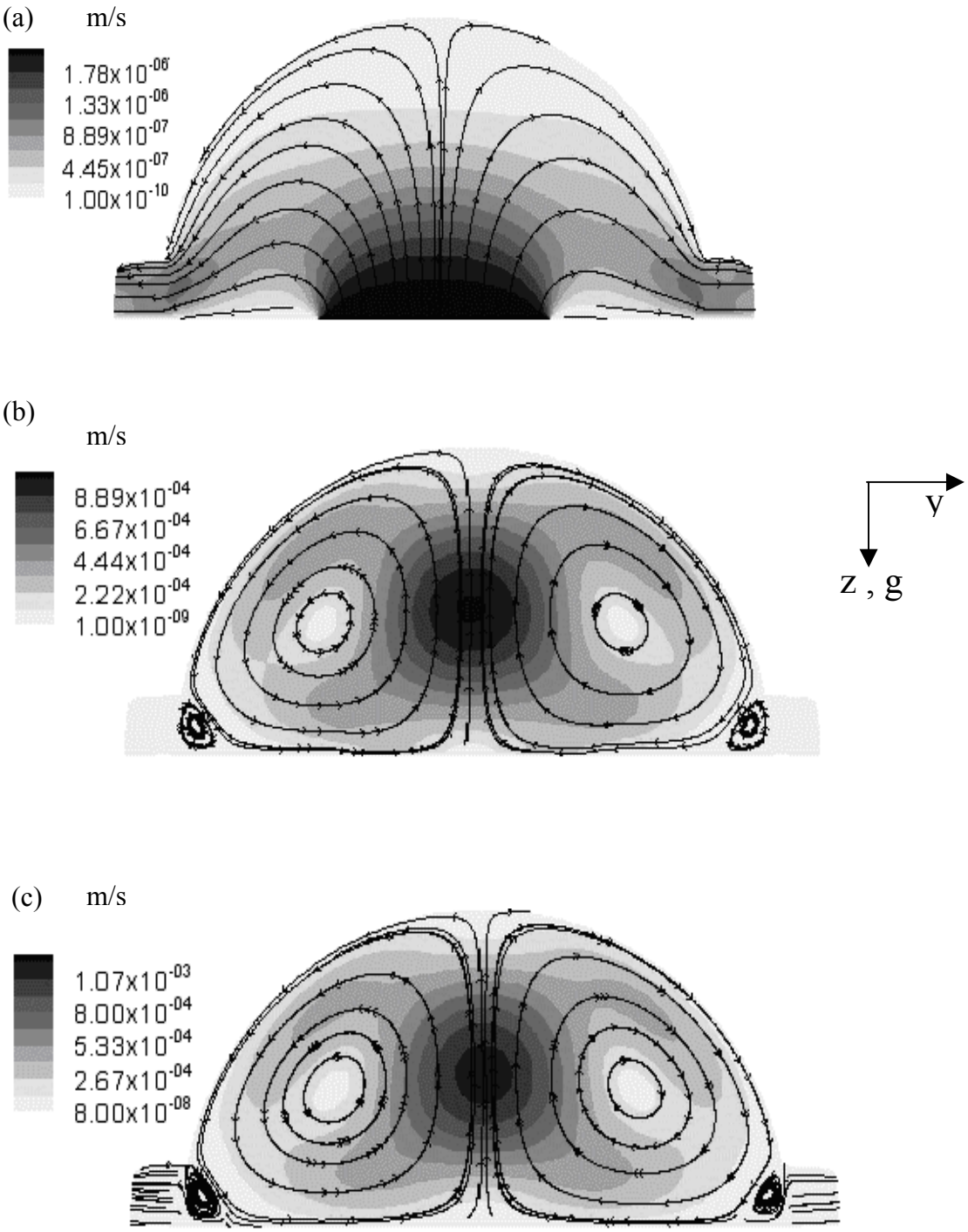

Figure 4-1: Streamlines and contours of velocity magnitude. (a) Without buoyancy (b) With Buoyancy and no inflow (c) With Buoyancy and inflow. $\Delta T = 2\,^{0}C$, Pore diameter = 100 μ .

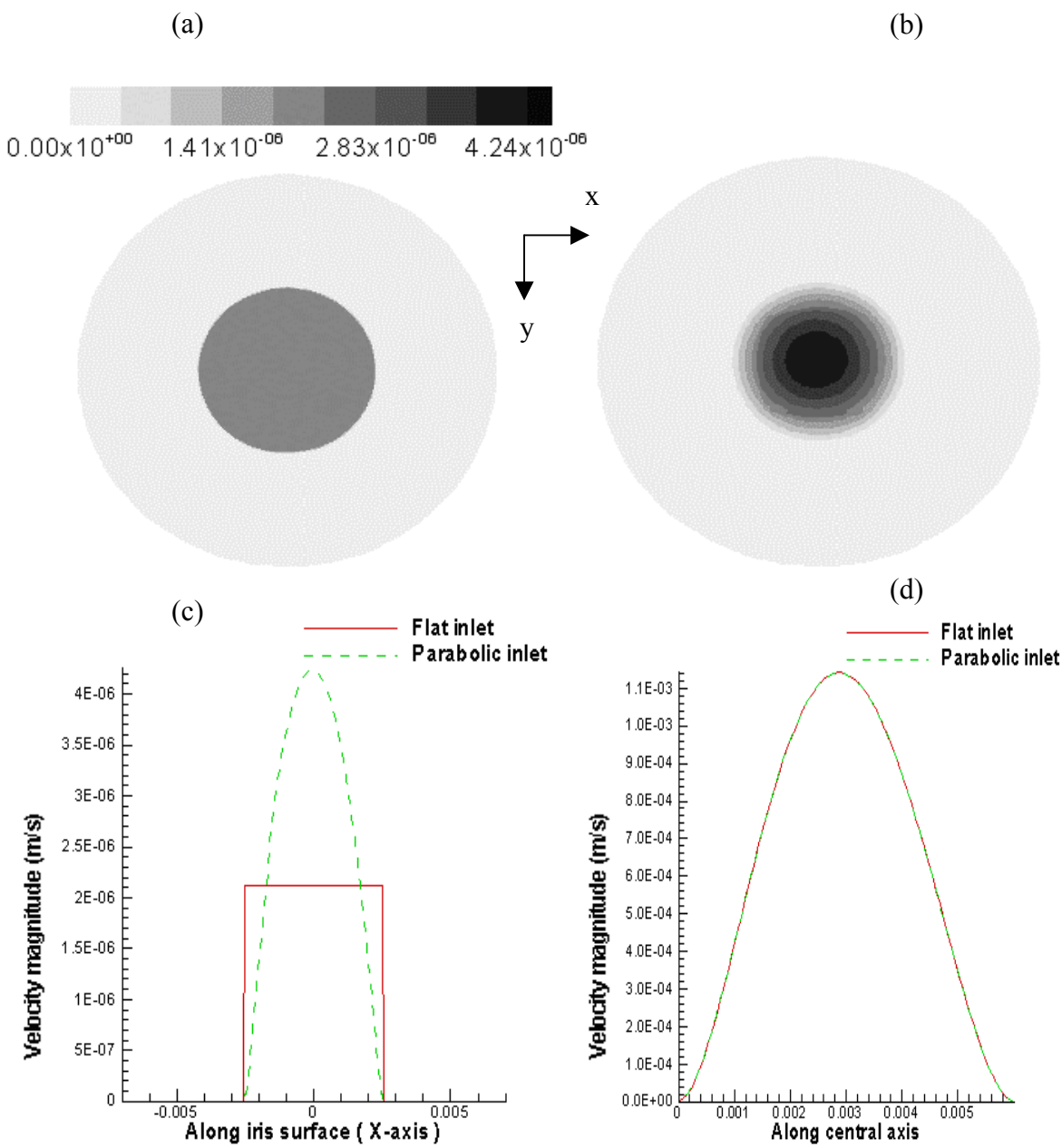

Figure 4-2: Horizontal orientation (a) Contours of velocity magnitude on iris surface and inlet aperture for flat velocity profile on inlet surface (b) Contours of velocity magnitude on iris surface and inlet aperture for parabolic velocity profile on inlet surface (c) Comparison of velocity magnitude along X-axis located on the iris surface and inlet aperture for the flat and parabolic velocity inlet profile (d) Comparison of velocity magnitude along the central axis for the flat and parabolic velocity inlet profile. $\Delta T = 2^{0} C$, Pore diameter = 0.6 μ .

chamber is not much affected by the inlet velocity profile since buoyancy is the dominant flow driving mechanism. This justifies the use of flat velocity profile in the pupillary opening at the inlet to the anterior chamber.

4.3 Effect of Eye Orientation

4.3.1 Velocity Contours

As seen in the preceding paragraph, gravity plays a major role in determining the flow pattern of AH inside the anterior chamber. In the horizontal upward-facing position, Fig. [4-3a], the gravity direction is perpendicular to the iris surface, and the flow field is axi-symmetric. In the vertical orientation, Fig. [4-3b] and Fig. [4-3c], gravity destroys the symmetry in the vertical (Y-Z) plane. For these two orientations, the flow profiles and re-circulation zones are completely different. For the horizontal position, the warmer fluid entering the pupil rises upward, and moves down the corneal surface leading to two large symmetric recirculation zones. The highest velocities (1.14 mm/s) occur midway along the vertical axis of symmetry. Just next to the TM there is a smaller recirculation zone, which shows the effect of the resistance of TM on the outflow. All features of the flowfield are identical about the vertical axis of symmetry including the exit flow rates through the left and right TM. For the vertical orientation of the eye, the warmer fluid rises upward along the iris surface and then turns downwards as it encounters the higher resistance in the upper TM regions. The flow then descends along the corneal surface toward the lower TM. The streamlines plotted in the horizontal mid plane passing through the center of the pupil reflect the flow path of AH, Fig. [4-3c], and show a helical path toward the TM. A portion of the recirculating flow exits through the small pores of the TM. Further, no secondary eddy is observed in the vicinity of the TM as in the horizontal configuration. The highest velocities are located near the middle of the iris surface (0.79 mm/s) and just upstream of the mid-corneal surface (0.627 mm/s). The stagnation zones and regions of large curvature are of special interest because particles or cells in the AH can get trapped in these regions and lead to the development of blockages, which can obstruct the vision or increase the IOP (e.g., as in pigmentary glaucoma). Clearly, in the vertical orientation the iris and the corneal surface are subjected to higher shear stresses than in the horizontal orientation. In order to clarify the difference of flow profiles in TM, the velocity contours and streamlines are plotted separately in the region of TM for both horizontal and vertical orientations of the eye, Fig. [4-4a], Fig. [4-4b] and

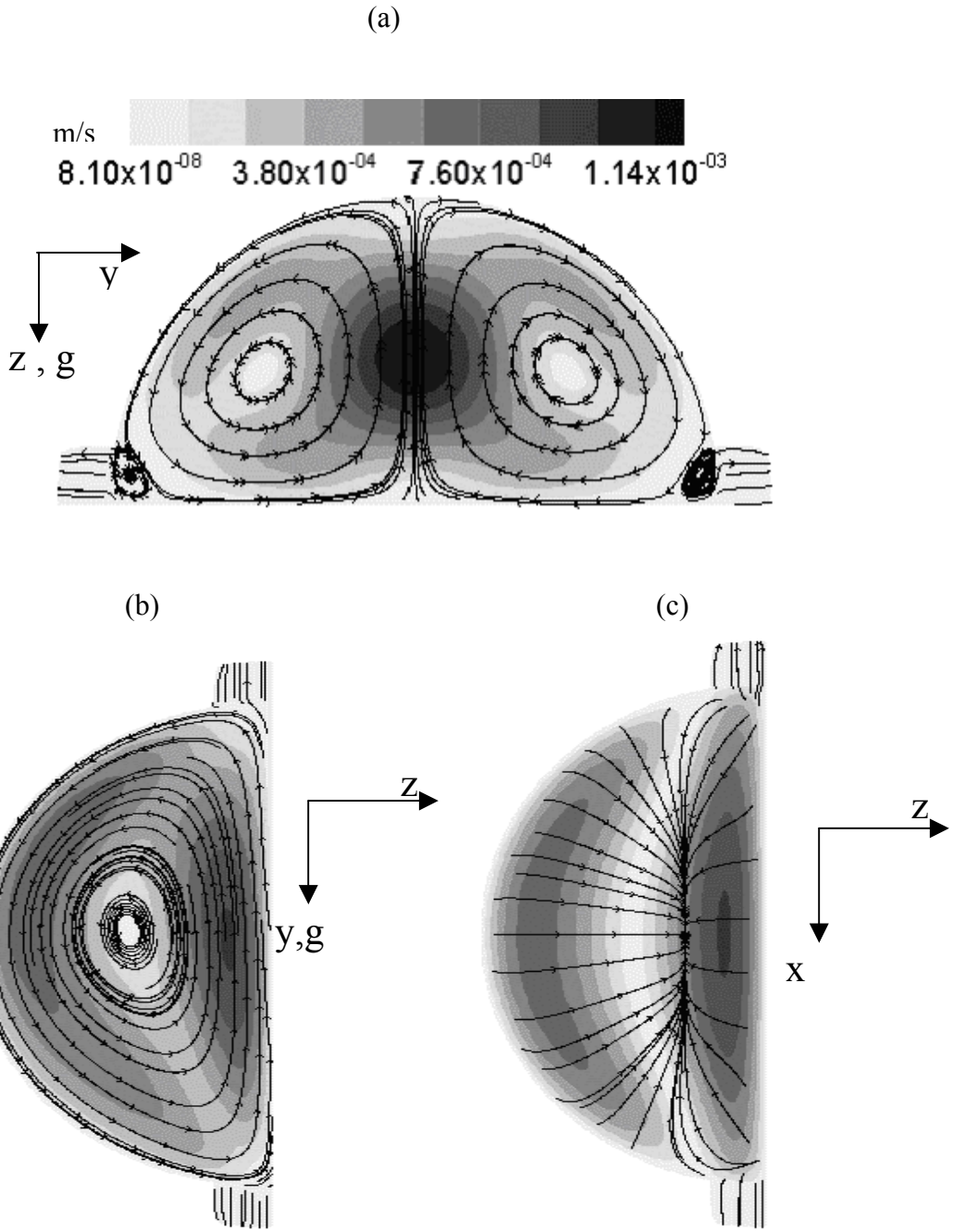

Figure 4-3: Streamlines and contours of velocity magnitude. (a) Horizontal orientation, Vertical mid plane (b) Vertical orientation, Vertical mid plane (c) Vertical orientation, Horizontal plane. $\Delta T = 2^{0} C$, Pore diameter = 0.6 μ .

Fig. [4-4c]). For both the orientations the magnitude of the flow-velocity decreases as the AH flows out from the anterior chamber to the aqueous veins through TM. The velocity magnitude along the center-line

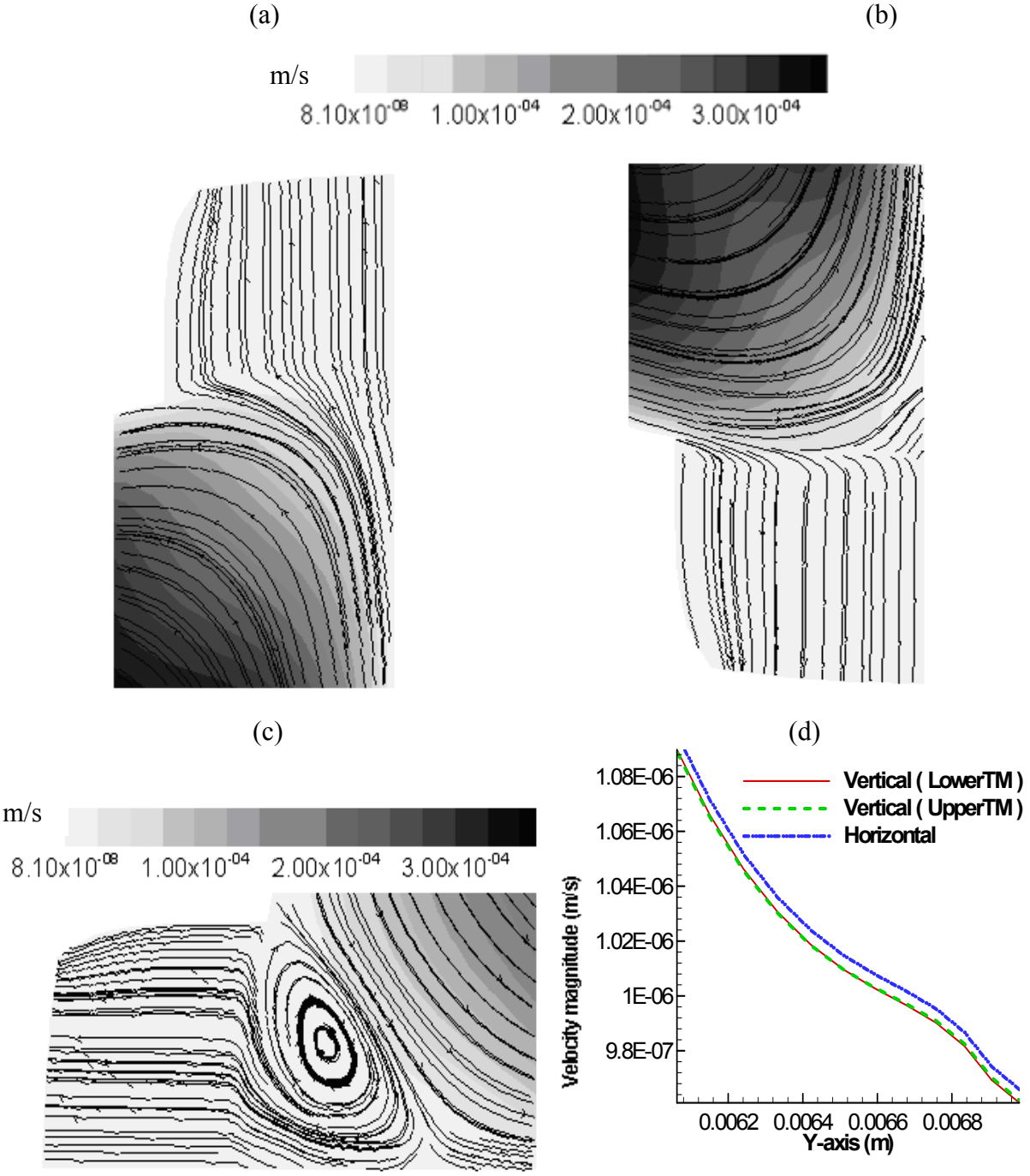

Figure 4-4: Streamlines and contours of velocity magnitude in TM, (a) Upper part of TM, Vertical orientation, Vertical mid plane (b) Lower part of TM, Vertical orientation, Vertical mid plane (c) Horizontal orientation, Vertical mid plane (d) Plot of velocity magnitude along centerline of TM in vertical mid plane for horizontal orientation and vertical orientation (upper and lower part of TM) of the eye. $\Delta T = 2^{0} C$, Pore diameter = 0.6 μ .

of the TM for the horizontal orientation of the eye is approximately 0.5 % greater then the corresponding values of vertical orientation of the eye, Fig. [4-4d]. The difference in exit flow rate through the upper and lower parts of the TM is almost negligible.

4.3.2 Temperature Contours

Contour plots for the temperature are shown in Figure [4-5a & 4-5 b] for both the horizontal and vertical orientations of the eye. The contours for the horizontal configuration clearly show the thermal plume rising in the middle. The AH get heated as it moves towards the center of the pupil along the relatively heated iris surface. Consequently, the temperature gradient keeps on decreasing from the iris root to the pupil center. When the thermal plume rises in the middle of the anterior chamber, the warmer fluid starts getting cooled as it approaches towards the cooler cornea. The largest temperature gradients are located at the stagnation point (mid-point of the corneal surface) and these temperature gradients diminish rapidly as the flow descends along the relatively cooler corneal surface. For the vertical configuration, the temperature gradient is relatively high close to the lower root of the iris, which diminishes as flow rises vertically upwards along the heated iris surface. Along the corneal surface the highest temperature gradient occur close to the upper regions as the flow turns along the cooler corneal surface due to resistance of the upper part of the TM. The flow get cooled while descending along the corneal surface and temperature gradient attains it lowest value on the corneal surface near to the lower part of the TM.

4.3.3 Pressure Contours

The pressure variations in the anterior chamber region are considerably smaller than the pressure drop across the porous TM and therefore the pressure contours in these regions are plotted separately in order to preserve clarity in the contour plots. Heys et al. [7] report in their simulations on eye model that pressure is essentially uniform inside the anterior chamber, which is supported by the present model. The pressure contours in the TM region are plotted in, Fig. [4-6a], for the horizontal eye orientation. Along the TM, from the anterior chamber to aqueous veins, the pressure decreases from the normal IOP of 15mm of Hg (~1.93 Kpa) [17] inside the anterior chamber to 9 mm of Hg (~1.2 Kpa) [17] corresponding to the

pressure in the veins. The pressure variations in the TM are relatively linear along the radial direction in the horizontal planes parallel to the iris surface, and appear to be essentially uniform along the normal to the iris surface. Therefore flow in the TM regions is essentially radially outwards from the anterior chamber to aqueous veins.

The pressure contours in the anterior chamber (excluding the TM-zone) are plotted in Fig. [4-6b] & Fig. [4-6c] for the two different orientations of the eye. For the horizontal position, Fig. [4-6b], the pressure is high close to the TM, which is a consequence of the resistance of the TM to the outflow. The pressure is also high near the mid-point of the cornea, where the AH-velocity reduces as it approaches the stagnation point on the corneal surface. The pressure decreases from the stagnation point as the flow accelerates downward along the corneal surface until it begins to sense the resistance of the TM at which point the pressure begins to rise. In the vertical orientation, Fig. [4-6c], as the flow accelerates upwards along the iris surface, pressure decreases by 0.01 Pa at a distance of 0.5 mm above the pupil center, at which point, the effect of the porous TM is felt and the pressure increases. Thus a region of high pressure is observed at the iris-upper TM juncture. As the AH descends along the corneal surface, the flow accelerates due to buoyancy and the pressure decreases. However, beyond the corneal mid-point, the pressure begins to increase due to the resistance to the outflow across the lower TM. In the lower half of the anterior chamber higher pressures and lower velocities are encountered relative to the upper half. Thus, the lower half is likely to be more susceptible to particle deposition, build up and blockages. The pressure is relatively uniform across the horizontal plane in the vertical orientation.

4.3.4 Shear Stress Contours

The rubbing between the peripheral iris and anterior zonular packets causes most of the pigmentary liberation from the posterior iris surface in Pigment Dispersion Syndrome and Pigmentary Glaucoma [2]. The anterior border layer of the iris is composed of fibroblasts and pigmented melanocytes, both of which are oriented parallel to the iris surface [10] and which could be the secondary source of pigment particles in the anterior chamber. The wall shear stress along the iris surface is analyzed to know the role of shear stress in detaching the pigment granules from the anterior layer of the

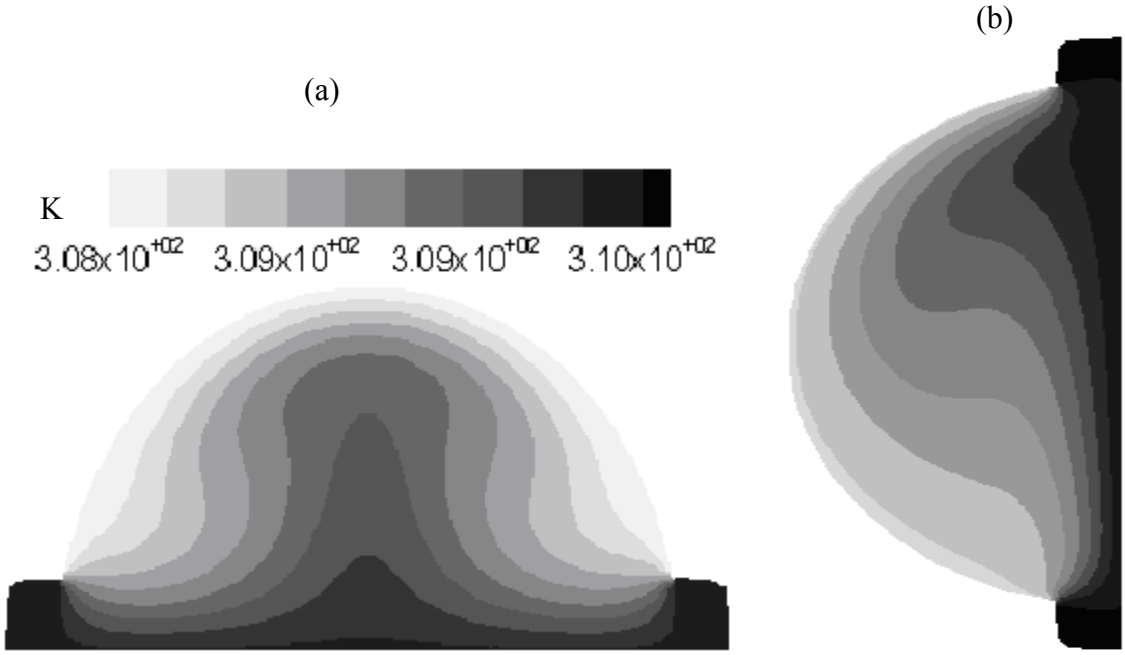

Figure 4-5: Contours of temperature. (a) Horizontal orientation, Vertical mid plane (b) Vertical orientation, Vertical mid plane. $\Delta T = 2^{0} C$, Pore diameter = 0.6 μ .

iris surface. For the two orientations of the eye the wall-shear stress is plotted in, Fig. [4-7], which shows increasing shear stress with increasing temperature difference across the cornea. Canning et al. [22] derived a linear relationship between the wall shear stress at the iris surface and the temperature difference across the anterior chamber. This was given as $\tau_0 \sim 6.7 * 10^{-4} * \Delta T$ Pa for the vertical orientation of the eye. The wall shear stress in the present model also shows an approximately linear relationship with ΔT, but the proportionality constant is $1.0 * 10^{-3}$, which is 1.49 times larger then the constant predicted by Canning et al [22]. This difference may be due to the lot of simplifications applied in the model by Canning et al [22]. in the momentum and energy equation for solving the equations in the closed form and avoiding numerical simulations. The magnitude of the shear stress predicted is much less than that required for the endothelial cell detachment which is in the range between 0.51 and 1.53 Kg/msec^2 as reported by Gerlach et al. [42]. So it is unlikely that fluid shear stress could detach pigments from the anterior iris surface, but the plot of shear stress gives insight about the location on the iris surface from where the probability of detachment of the cells is maximum in case of some specific diseases or

presence of free pigment granules in the anterior iris layer. For the horizontal orientation, the wall-shear stress is highest near the inner periphery of the iris, while for the vertical position the maximum shear stress zone is located in the lower half of the iris surface close to the pupil, Fig. [4-7a] & Fig. [4-7b].

4.4 Effect of TM Pore Size

The resistance of the TM is increased when its pores are clogged with small particles like pigment-granules or protein particles (albumin). The net effect of this clogging process is an increased resistance to the flow imposed by the TM. The increasing resistance of TM to the outflow is modeled here by decreasing its pore size. The justification of this approach rests on the fact that as particles are deposited in the interstitial passages of the TM, the effective porosity of the TM is reduced. Of specific interest in the present study is to understand how a decrease in the pore size of the TM affects the IOP in the anterior chamber.

As shown in Fig. [4-6], the pressure variations in the anterior chamber are small compared to the pressure drop across the TM. Therefore the peak pressure in the anterior chamber can be defined to be a suitable measure of the IOP . For pore size greater than 10 μ pressure drop across the TM is small and resistance of the TM to the outflow is low. For a pore-size of 0.6 μ, which is representative of pore sizes (0.1-1.0 μ) in the JCM, the computed pressure drop across the TM is 730 Pa (~ 6 mm of Hg), which is in agreement with the pressure drop reported by experimental studies [16] on a normal eye. Heys et al. [7] have reported calculations of IOP for different inflow rates using an approximation for the outflow boundary condition that does not incorporate calculations through the TM. They report an IOP of 14 mm of Hg for an inlet flow-rate of 2.0 $\mu L/\min$ and an IOP of 17 mm of Hg for inlet flow rate of 3.0 $\mu L/\min$. Their IOP calculation is based on a linear relation between the AH flow rate and IOP of the eye. The IOP calculated by the present model, which incorporates a porous matrix representation of the TM and calculations in the TM, is 15 mm of Hg for a 2.5 $\mu L/\min$ inlet flow-rate (pore-size = 0.6 μm), which lies within the range of values reported by Heys et al. [7].

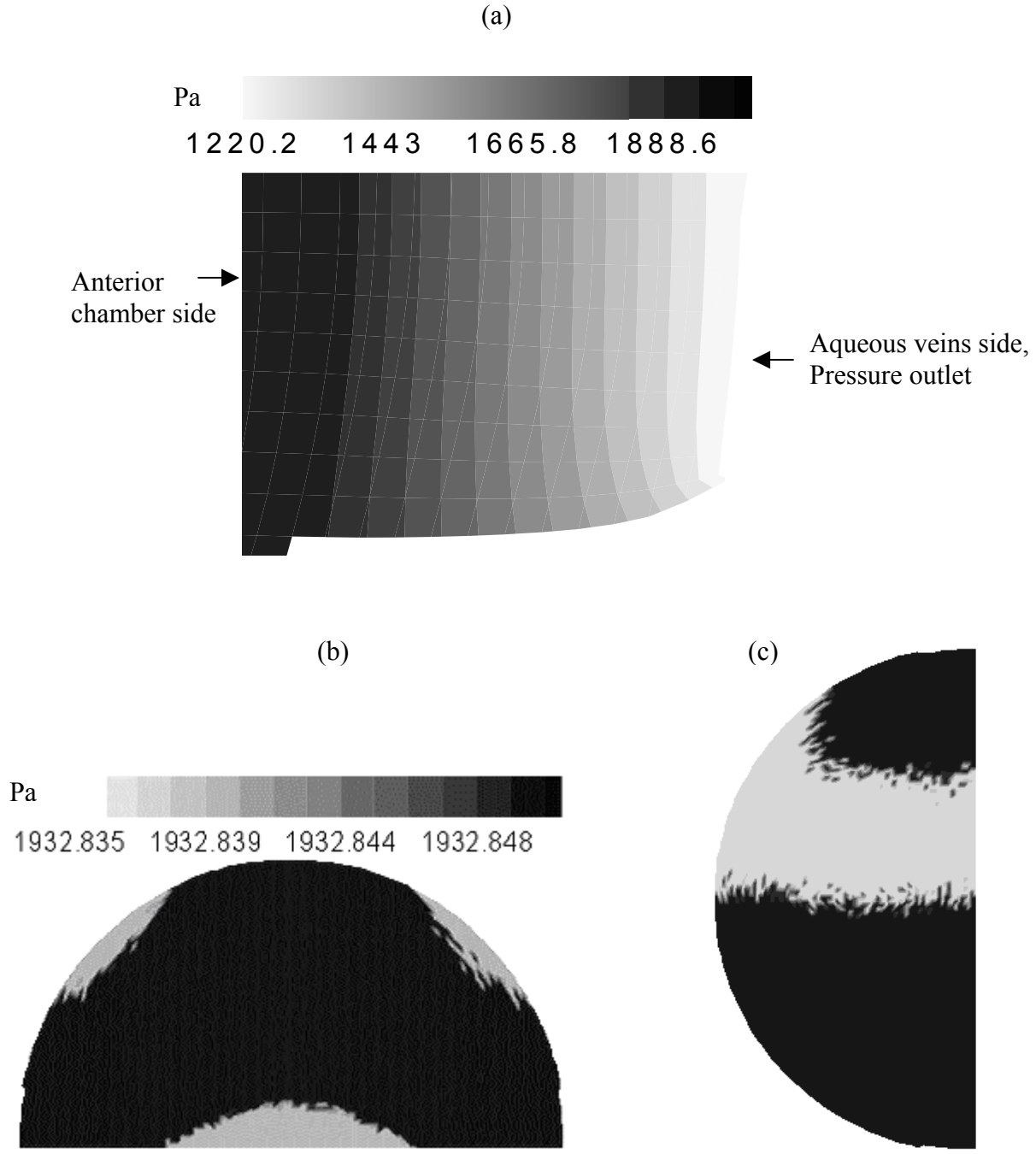

Figure 4-6: Contours of pressure. (a) In the TM (b) Horizontal orientation, Vertical mid plane (b) Vertical orientation, Vertical mid plane. $\Delta T = 2^{0} C$, Pore diameter = 0.6 μ m.

Table [4-1] indicates that an increase in IOP occurs as the pore size is reduced below 2 microns. This implies that pore size of the TM is the governing parameter for resistance to outflow of AH inside

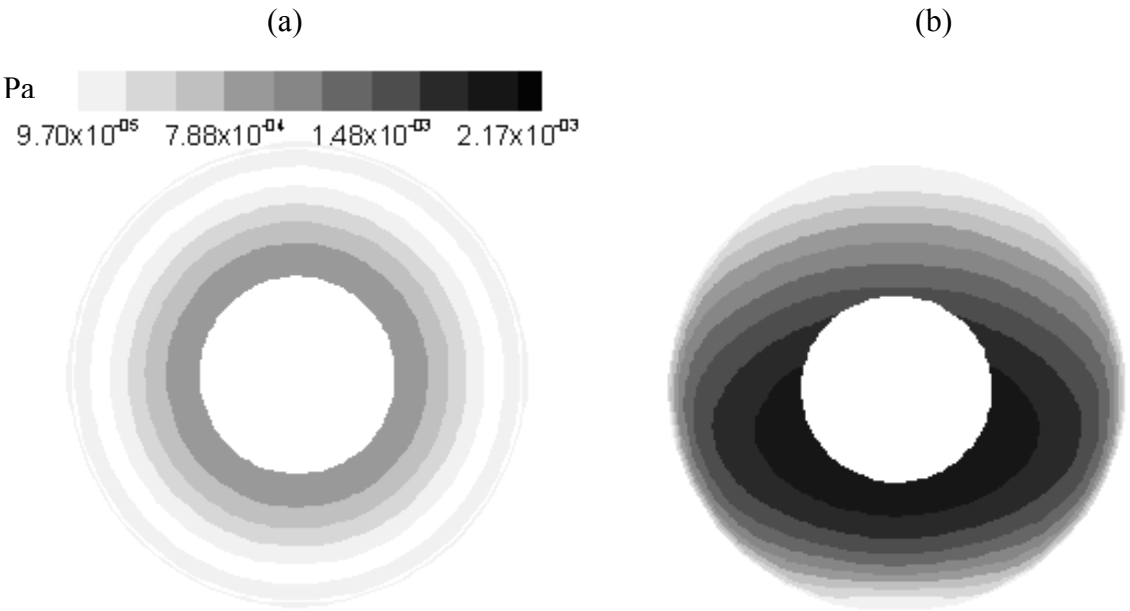

Figure 4-7. Wall shear stress plot for the anterior iris surface. (a) Horizontal orientation, Vertical mid plane (b) Vertical orientation, Vertical mid plane. $\Delta T = 2^0 C$, Pore diameter = 0.6 μ m.

Table 4-1: Trend of IOP with pore size of JCM (ε =0.5).

Pore size (μ)	IOP (KPa)	IOP (mm Hg)
100	1200.029	9.000
40	1200.179	9.002
10	1202.758	9.021
5	1210.528	9.079
2	1265.000	9.488
0.6	1930.000	14.476

the eye. Clogging of the TM pores by small particles (pigment or protein) [29] present in AH is equivalent to the reduction of the effective pore size of TM, which leads to increase in IOP. So this relationship of pore size and IOP provides a basis for analyzing or correlating specific diseases

The effect of porosity (ε) on IOP is analyzed by comparing the results for different porosity and different pore size of the TM. Simulations are performed with different values of porosity reported in the experimental studies. The simulations with porosity of 0.5 and pore size of 0.6 μ m is representative of the studies reported by Lindenmayer et al [43]. Lutjen-Drecoll [44] has reported that the optical clear

space of JCM as 17+-7.7 %, while Ethier et al. [17] has reported it as 23+-4.6 %. The simulations are performed with 0.25 and 0.2 porosity to analyze the porosity values reported by Lutjen-Drecoll [44] and Ethier et al [17]. It is observed that for porosity of 0.25 and pore size of 0.9 μ m, the IOP of eye is 14.206 mm of Hg, which is close to the IOP with the porosity of 0.5 and pore size of 0.6 μ . For porosity of 0.2 and pore size of 1.0 μ m the IOP is 140.063 mm of Hg, which is again close to the IOP of eye observed in simulations with porosity of 0.5 (pore size = 0.6 μ m) and porosity of 0.25 (pore size = 0.9 μ m), Table [4-2]. The pore size of TM for which achieved IOP of eye is close to IOP of normal eyes (14-15 mm of Hg) lies in the range of 0.1-1 μ , which is representative of the pore size of JCM reported by experimental studies [15]. So the effect of TM is similar for all the three simulations. Achievement of realistic IOP of eye and realistic pressure drop across the ocular drainage system for the pore size and porosity values lying in the range reported by the experimental studies validates the capability of model to predict the realistic ocular dynamics.

Table 4-2: Trend of IOP with porosity of JCM.

Porosity (ε)	Pore size (d)	Pore diameter (D_p)	IOP (KPa)	IOP (mm Hg)
0.5	0.6	0.6	1930.000	14.476
0.25	0.9	2.7	1894.000	14.206
0.2	1.0	4.0	1875.000	14.063

Porosity of the TM can be changed by using some drugs eg. pilocarpine. The above simulations with different porosity values can be utilized to understand the effect of these drugs by including some other specific features and outcomes of drugs in the eye model.

4.5 Effect of Temperature Gradient Across the Anterior Chamber

As noted earlier, the driving mechanism for the AH is the temperature difference across the anterior chamber. A reasonable temperature difference between corneal and iris surface is $\Delta T = 2^0 C$, but conditions such as the outside ambient temperature, and whether the eye is open or closed, can cause variations in the corneal temperature. In this study, the temperature difference across the anterior chamber

has been varied from 0.02^0C to 6^0C, with 0.02^0C corresponding to the case when the eye-lid is closed and the corneal temperature is close to the body temperature, Fig [4-8a]. The flow patterns and the velocity magnitudes are quite different between the 0.02^0C and the 2^0C cases. In the horizontal orientation of the eye, for the 0.02^0C case, the center of the primary recirculation is shifted towards the iris surface and the magnitude of the maximum velocity is close to the inlet velocity through the pupil. Since the flow velocities are small the secondary re-circulation zone near the TM is not present any more. When the temperature difference is increased to 4^0C, Fig. [4-8c], the profile is similar to the normal temperature difference (2^0C) case but the magnitude of the maximum velocity is increased by a factor of 2. A similar profile is observed even for a temperature difference of 6^0C with 2.57 times larger magnitude of maximum velocity compared to the 2^0C temperature difference case.

For the vertical orientation of the eye, at a low ΔT of 0.02^0C, the streamlines are skewed inwards close to the iris surface, Fig. [4-8d]. This is because at this low ΔT, the buoyancy-induced flow is weak and comparable in magnitude to the inflow that enters the anterior chamber orthogonal to the iris surface. As a consequence, the resulting velocity vector near the pupil aperture is at an angle to the iris surface. When ΔT is increased to 2^0C or 4^0C, Fig. [4-8e] & Fig. [4-8f], the buoyancy induced flow directed upwards along the iris is considerably stronger (by an order of magnitude) than the inflow, and consequently the flow near the iris surface is essentially parallel to it. By increasing the temperature difference from 2^0C to 4^0C, the increase in magnitude of the maximum velocity is 1.5 times, which is

Table 4-3: Non-dimensional velocity, Average Nusselt Number and Iris shear stress variation with temperature difference (Horizontal position).

	0.02^0C	2^0C	4^0C	6^0C
$U_{\max} / U_{inlet}$	2.12	538	1024	1387
Nu (Nusselt Number)	4.54	5.56	6.18	6.56
Wall shear stress (Iris, Pa)	$7.0*10^{-6}$	$1.16*10^{-3}$	$2.12*10^{-3}$	$2.94*10^{-3}$

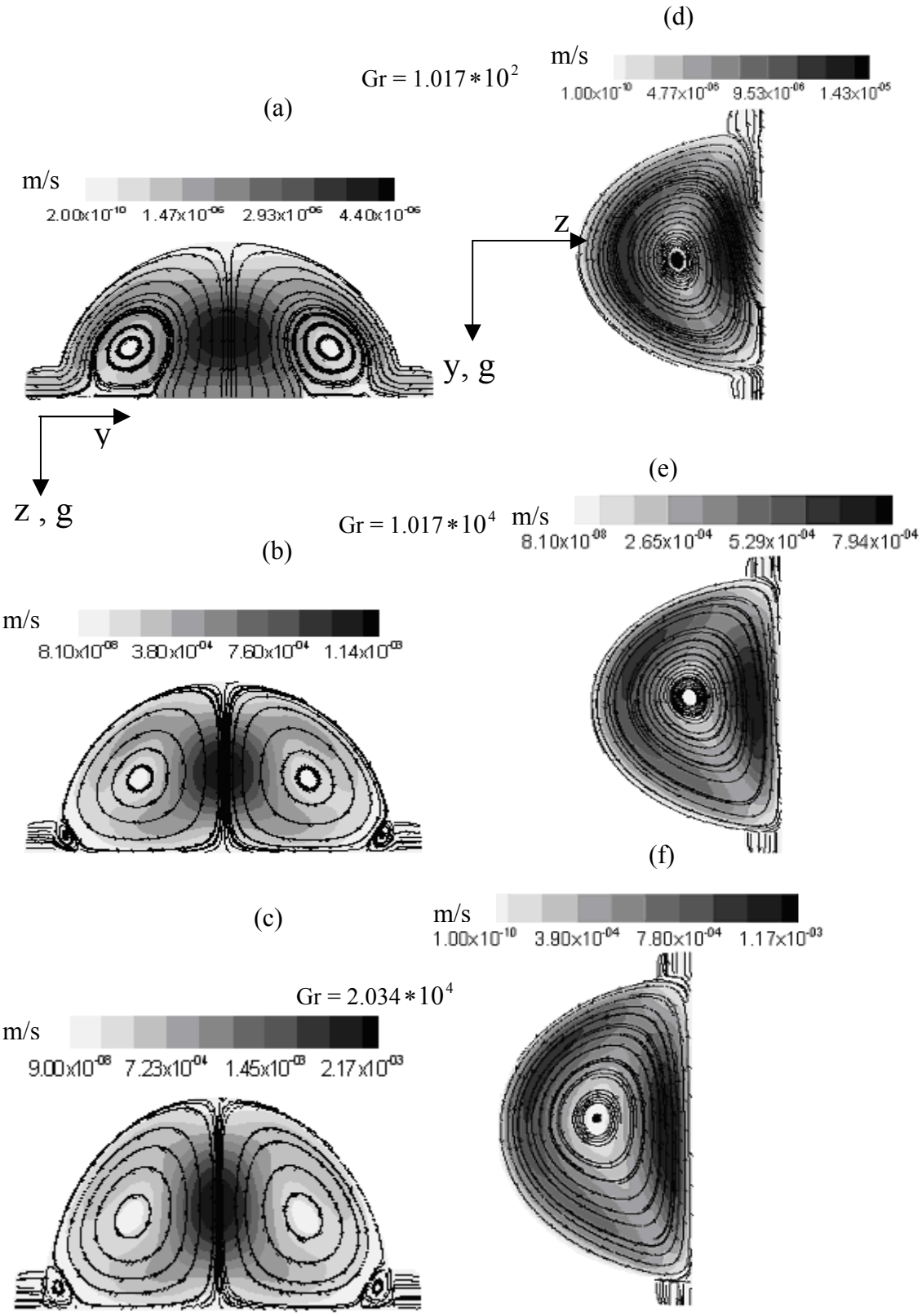

Figure 4-8: Velocity contour plot in vertical mid plane. Horizontal orientation, (a) $\Delta T = 0.02\,^{0}C$ (b) $\Delta T = 2\,^{0}C$ (c) $\Delta T = 4\,^{0}C$. Vertical orientation, (d) $\Delta T = 0.02\,^{0}C$ (e) $\Delta T = 2\,^{0}C$ (f) $\Delta T = 4\,^{0}C$.

less than the 2 times increase for the horizontal orientation. Heys & Barocas [23] found that the velocity increased by 1.5 times when the temperature difference across the anterior chamber increased from $3\,^0C$ to $7\,^0C$, but the flow pattern itself was not significantly affected by this temperature increase. Thus, their observations are generally consistent with our predictions.

Table 4-4: Non-dimensional velocity, Average Nusselt No and Iris shear stress variation with temperature difference (Vertical position).

	$0.02\,^0C$	$2\,^0C$	$4\,^0C$	$6\,^0C$
$U_{\max}/U_{inlet}$	6.7	373	552	680
Nu (Nusselt Number)	4.54	5.49	6.12	6.56
Wall shear stress (Iris, Pa)	$2.0*10^{-5}$	$2.17*10^{-3}$	$3.79*10^{-3}$	$5.17*10^{-3}$

The average heat flux across the cornea for $\Delta T=2\,^0C$ is 550 W/m^2 and for $\Delta T=4\,^0C$ is 1230 W/m^2, which is in agreement with the results of Heys & Barocas [23], who report the average heat flux of 800 W/m^2 for $\Delta T=3\,^0C$. For the horizontal and vertical orientation respectively, Tables [4-3] and [4-4], shows the non-dimensional maximum velocity, the average Nusselt number and the shear stress for different values of ΔT across the anterior chamber. There is a difference of two orders of magnitude in maximum velocity inside the anterior chamber when ΔT is increased from $0.02\,^0C$ to $6\,^0C$, this shows the dominance of buoyancy on AH flow inside the eye. The non-dimensional heat transfer coefficient (Nusselt number, Nu) at the corneal surface shows increases with increasing temperature differences. For both orientations of the eye, Nu has the same value (4.56) at $\Delta T=0.02\,^0C$ (expected since buoyancy does not play a major role) and increases to 6.56 for $\Delta T=6\,^0C$. The similar values for Nu for the two orientations at ΔT of $6\,^0C$ is somewhat unexpected since buoyancy is important at this ΔT, and the flow patterns are different. However, these are average values and while the averages are close, significant differences in the local values are obtained. The wall shear stress on the iris surface has approximately linear relationship with ΔT. The constant of proportionality for horizontal orientation of

the eye is $0.53*10^{-3}$ ($\tau_0 \sim 0.5*10^{-4}*\Delta T$) while for the vertical orientation it is $1.0*10^{-3}$ ($\tau_0 \sim 1.0*10^{-4}*\Delta T$). Clearly the shear stress values are significantly influenced by the orientation of the eye, with values for the vertical orientation that are nearly two times those of the horizontal orientation.

4.6 Effect of Pupil Size

Since the size of the pupil opening varies with the intensity of the light in the surroundings, we simulated the flow for two different diameters of the pupil-5mm and 3mm. The same flow rate and depth of the anterior chamber was maintained. No major change in the IOP or velocity profile of the AH is observed. This behavior of the flow is a consequence of almost negligible effect of inlet velocity on the flow profile and the dominance of buoyancy.

4.7 Concluding Remarks

A three-dimensional model for the anterior chamber of the eye is developed in order to investigate the flow and pressure distribution inside the eye. The computational model includes a model for the complex Trabecular Meshwork. The IOP predicted inside the anterior chamber and the pressure drop across the TM (corresponding to real pore size of the JCM) are found to be close to experimental observations for a normal eye. The following major observations are made from the computed results.

1. Predictions verify the dominance of the buoyancy as the driving mechanism for the AH flow.
2. The two orientations of the eye, horizontal and vertical, lead to different flow patterns and temperature distributions.
3. The pressure drop mostly occurs across the TM. Within the anterior chamber, the variations in pressure are relatively small.
4. The IOP begins to increase for TM openings of 2 microns or less. Blockages in the TM at this level will be detected in the anterior chamber pressure, and indicate a physiological problem with the eye.

5. The surface shear is higher in the vertical orientation (by a factor of nearly 2). The surface shear is correlated with pigmentary cell removal. The average Nusselt number is not significantly influenced by the orientation of the eye.
6. The temperature gradient across the anterior chamber is the key parameter controlling velocity magnitudes, and shear rates. Increasing the temperature difference from $0.02^{0}C$ to $6^{0}C$ produces increases in the velocity magnitudes by greater than {2_26} 2 orders of magnitudes and comparable increases in shear stress.
7. The pupil opening has little or no influence on the AH flow pattern or velocity magnitudes.

CHAPTER 5. PARTICLE SIMULATION IN RABBIT EYE

5.1 Particle Trajectories

Figure [5-1] shows the trajectories of 1 μ diameter particles released from the various circumferential positions at different radii located on the pupil surface or the iris surface. For the vertical orientation of the eye, particles released from the pupil surface rises against gravity along the iris surface with the flow. When it encounters higher resistance while approaching the upper part of TM, it descends along the corneal surface. Most of the particles come out from the lower part of the TM, but some again rises up to the middle portion of the anterior chamber and then comes out from TM in the mid horizontal plane, Fig. [5-1a]. The average time spent by most of the particles is around 2200 s (37 min), Table 3a. Particles released from the central portion of the pupil surface spend more time in the anterior chamber compared to the other particles. As the radius of the circles on the pupil surface from where particles are released, is increased, the time spent by the particles in the anterior chamber decreases, Table [5-1a]. Particles released from the iris surface have trajectories similar to the particles released from the pupil surface except that a number of particles exit from the top of the TM, Fig. [5-1b]. This difference between pupil and iris released particles is observed because the particles released from the pupil surface circulate in the vicinity of the vertical mid plane passing through the central axis, while particles released from the iris surface circulate in the planes parallel to the vertical mid plane. Due to strong flow in the vertical mid plane particles released from the pupil surface keep on circulating and do not come out from the upper TM, while the iris released particles come out through the pores of upper TM as in other vertical planes flow has low strength. As the distance of point of release of the particles from the pupil center is increased, their residence time inside the anterior chamber decreases. The particles released from the root of the iris show completely different behavior. Some of these particles spent a minimum time of 867 s and other particles spent maximum time of 6064 s inside the anterior chamber, Table [5-1b]. This is in agreement with the flow field

observed next to TM. This is the region where flow has sharp curvature and magnitude of flow velocity is very low, so some particles keep on moving randomly near to the TM in the anterior chamber before entering the pores of the TM and correspondingly spend maximum time inside the anterior chamber. While some particles enter early into the pores of the TM in their random motion next to the TM and escapes from the anterior chamber in the minimum time, Table [5-1b]. Most of the pigment particles have maximum residence time at the lower portion of the cornea or inside the pores of TM, Fig [5-1a & 5-1b]. This reflects the possibility of these particles to get adhere on the endothelium layer at the lower corneal surface, which could lead to the formation of spindle like structure at lower part of the cornea (KS), Fig. [2-4b] or they could clog the pores of TM and can lead to elevation in IOP of the eye.

For horizontal orientation of the eye, the particles released from the iris surface rises against gravity along axial direction towards the central portion of the cornea and after encountering the resistance from corneal surface they descend along the cornea. Due to the small vortex next to the TM, these particles do not descend along the cornea up to the iris root, but follow the vortex streamlines and strikes the iris surface in a circular band of radius 5 mm from the pupil center, Fig. [5-1c]. The average residence time of these particles is 1700 s (28 mins), Table [5-1a]. The trajectories of these particles show high residence time near to the central portion of the cornea and inside the pores of TM, which shows the possibility of adherence of these particles to central corneal endothelium or TM walls. When the particles are released from the iris surface, they follow the trajectories almost similar to the particles released from the pupil surface except that they come closer to the portion of the cornea next to the central region before descending along the corneal surface, Fig. [5-1d]. There is stagnation region on the iris surface next to the small vortex at the bottom of the anterior chamber, which is located approximately at a distance of 5 mm from the iris center. So the particles released from this location spend maximum time (1803 s) inside the anterior chamber. Particles released outside the region of 5 mm radius is

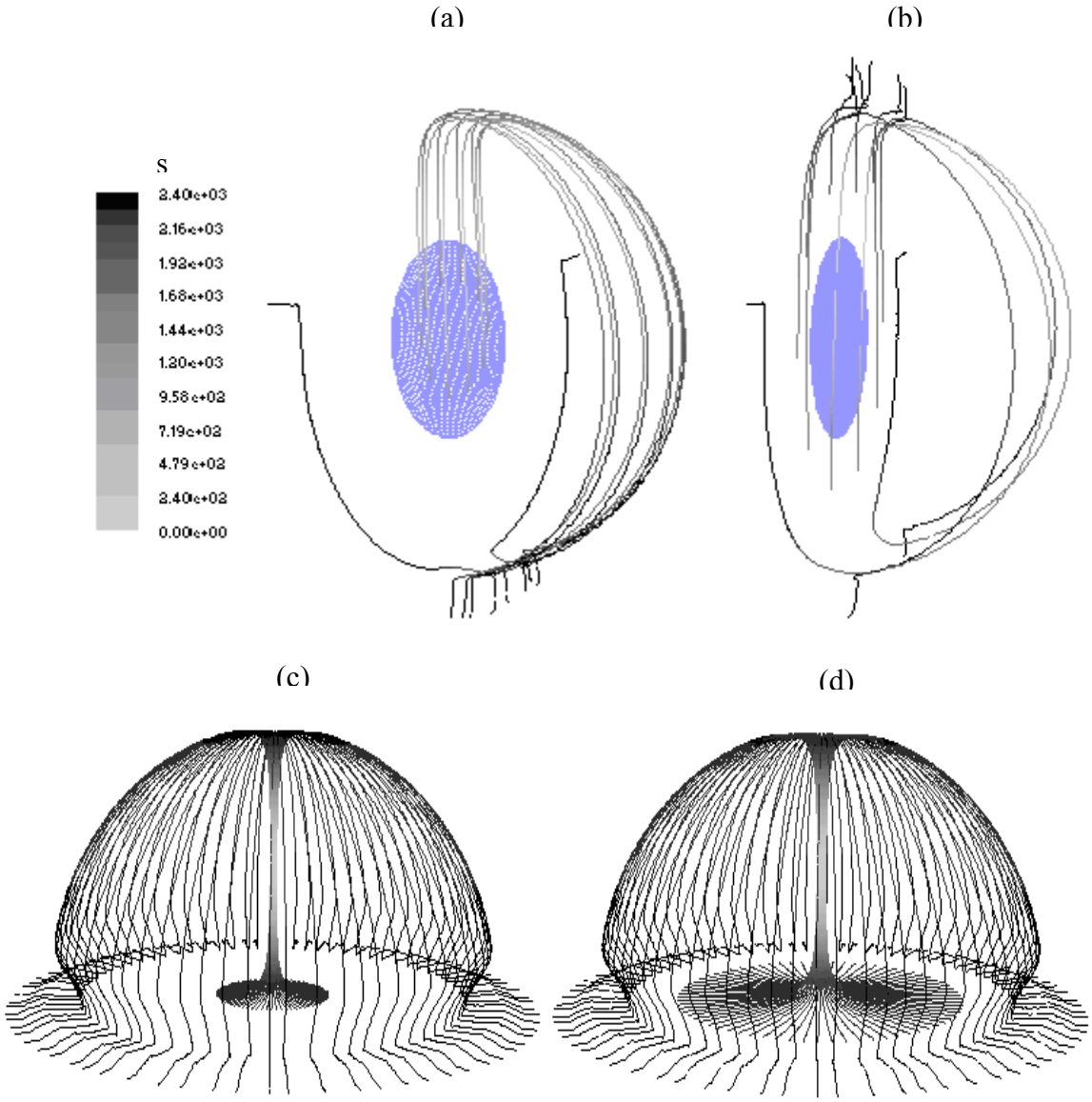

Figure 5-1: Pigment Granules (a) Particles released from the pupil surface located on the circumference of radius 1.5 mm, Vertical orientation. (b) Particles released from the iris surface located on the circumference of radius 3.8 mm, Vertical orientation. (c) Particles released from the pupil surface located on the circumference of radius 1.5 mm, Horizontal orientation. (d) Particles released from the iris surface located on the circumference of radius 3.8 mm, Horizontal orientation.

affected by the small corner vortex next to TM and show different behavior from the particles released within the radius of 5 mm. When the particles are released from the region inside the radius of 5 mm, the minimum residence time (1690 s) belongs to the particles released from the

iris-tip, which increases with the radius of point of release as shown in Table [5-2b]. Particles released from the iris root do not circulate inside the anterior chamber and come out through the TM in the shortest time (1458 s).

For analysis of erythrocytes and leucocytes, particles of diameter 7 μm and 10 μm are released from iris and pupil surface and both of them follow almost similar trajectories inside the anterior chamber. For the vertical orientation of the eye, particles released from the pupil surface rises along the iris surface and then descends along the corneal surface after facing high resistance from upper part of TM. These particles are not able to sweep away by the flow when they reach at the bottom of the anterior chamber and get deposited on the ocular tissues, Fig. [5-2a & 5-2b], which is evident from the high residence time of these particles at the bottom portion of the anterior chamber and end of the particle trajectories. The deposition of these particles gives insight for the possibility of the formation of layered Hyphema or Hypopyon at the bottom of the anterior chamber.

For the horizontal orientation of the eye, the particles released from the pupil surface move toward the center of the pupil. These heavier particles are not able to rise against gravity with flow and show tendency of getting accumulated in the central region, Fig. [5-2d]. Particles released from the iris surface within the radius of 3.8 mm move towards the center, but particles released from locations outside this region move around their point of release, which is indication of getting trapped on the iris surface, Fig. [5-2e]. Particles released from the center of the anterior chamber in vertical mid plane keep on circulating inside the anterior chamber in the vertical mid plane with increasing diameter. When it come closer to the ocular tissues at the bottom of the anterior chamber, it get deposited there, Fig. [5-2c]. This behavior of the particle released from the center is in agreement with the results of Heys & Barocas [23].

5.2 Formation of Krukenberg Spindle

The deposition of pigment particles on the corneal surface leads to the formation of vertical spindle like structure known as Krukenberg Spindle. There are few locations inside the

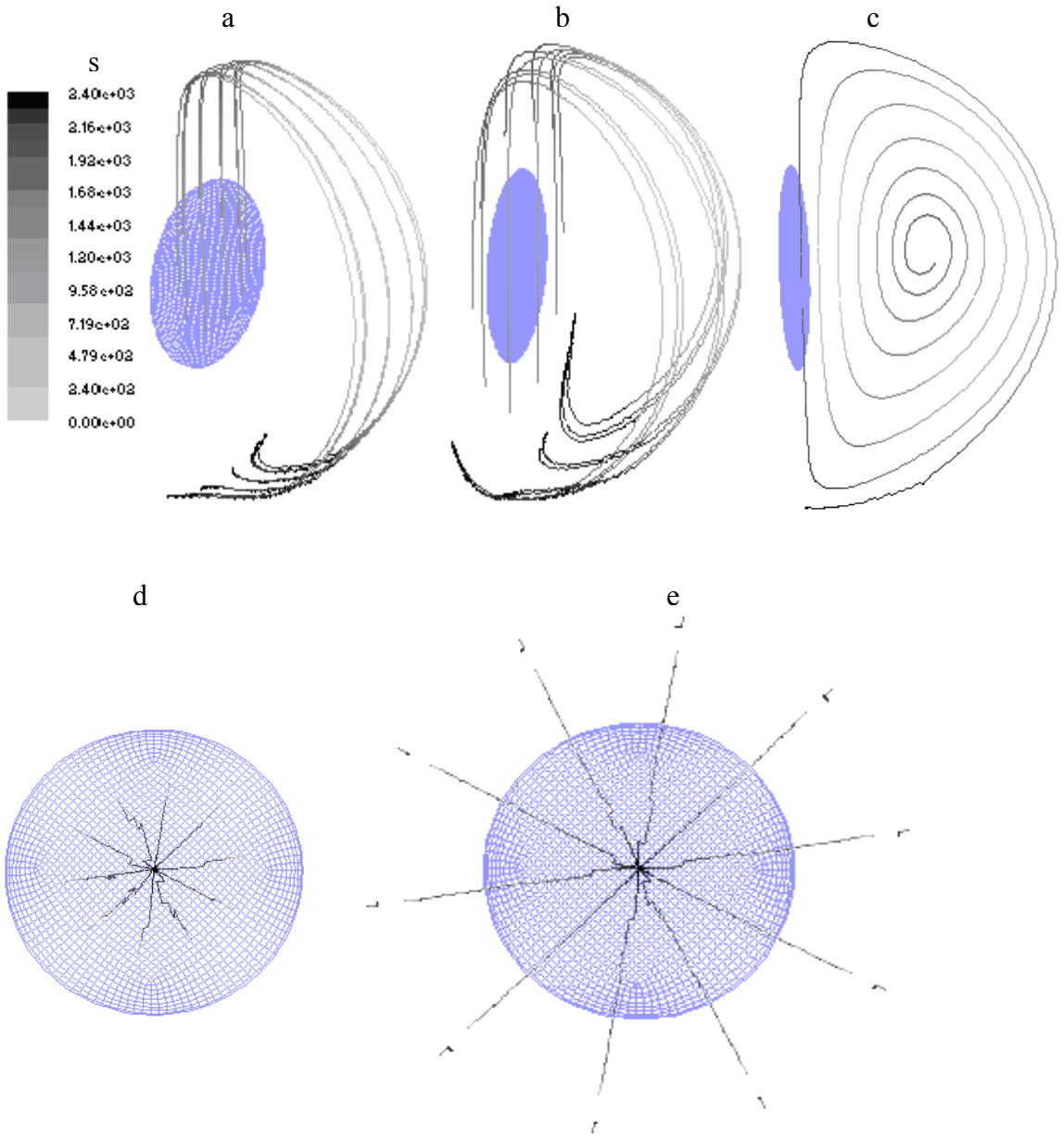

Figure 5-2: Erythrocytes (a) Particles released from the pupil surface located on the circumference of radius 1.5 mm, Vertical orientation. (b) Particles released from the iris surface located on the circumference of radius 3.8 mm, Vertical orientation. (c) Particle released from the center of the anterior chamber, Vertical orientation. (d) Particles released from the pupil surface located on the circumference of radius 1.5 mm, Horizontal orientation. (e) Particles released from the iris surface located on the circumference of radius 3.8 mm and 4.4 mm, Horizontal orientation.

anterior chamber, where the flow takes sharp bend and stagnates due to the resistance of the ocular tissues. These are the regions where the deposition of the particles is likely to occur, as once the particles get adhered to the ocular tissue at that location; flow is unable to sweep away

Table 5-1(a). Time spent by particles inside anterior chamber when released from circumference of different radii on pupil surface (Vertical Orientation, Particle dia = 1 μ).

Radius(r) mm	Minimum (s)	Maximum (s)	Average (s)
0.7	2083	2399	2197
1.0	2068	2446	2188
1.5	2079	2545	2197
2.0	1994	2396	2185
2.4	1895	2424	2151

Table 5-1(b). Time spent by particles inside anterior chamber when released from circumference of different radii on iris surface (Vertical Orientation, Particle dia = 1 μ).

Radius(r) mm	Minimum (s)	Maximum (s)	Average (s)
2.6	1976	2347	2131
3.2	1873	2296	2109
3.8	1817	2334	2095
4.4	1769	2348	2045
5.0	1800	2440	2054
5.8	867	6064	2423

Table 5-2(a). Time spent by particles inside anterior chamber when released from circumference of different radii on pupil surface (Horizontal Orientation, Particle dia = 1 μ).

Radius(r) mm	Average (s)
0.7	1737
1.0	1710
1.5	1694
2.0	1692
2.4	1688

Table 5-2(b). Time spent by particles inside anterior chamber when released from circumference of different radii on iris surface (Horizontal Orientation, Particle dia = 1 μ).

Radius(r) mm	Average (s)
2.6	1690
3.2	1700
3.8	1711
4.4	1724
5.0	1803
5.8	1458

those particles. Particles keep on accumulating on those regions and spindle shaped structure is formed on the ocular surface.

There are two sources of pigment granules inside the anterior chamber- (a) particles shedded from the pigmentary layer of posterior iris surface [2, 44] that enter into the anterior chamber through the pupil, (b) pigment particles that may be present on the anterior iris surface [45] and are released directly into the anterior chamber. For analyzing the behavior of particles entering the anterior chamber through the pupil with AH, particles are released from the points evenly spaced on the circumference of the circles of different radii located on the circular inlet aperture. Kuchle et al. [25] has reported in their experimental results on eye with PDS that 2.5 μl of the AH contains approximately 100 pigment granules. Particles are released from the circular aperture at 409 different locations and their mass flow rate is kept constant such that the concentration of the pigment granules entering the anterior chamber would be in agreement with the experimental results of Kuchle [25]. Pigment particles generated from the anterior surface of the iris are modeled by releasing 72 particles from the circumference of every circle of radii varying from 2.6mm to 5.8mm (r = 2.6, 3.2, 3.8, 4.4, 5.5, 5.8 mm).

For the vertical orientation of eye, when the particles are released from the pupil surface, the concentration of the particles is high at the mid-lower portion of the corneal surface, Fig. [5-3a]. The concentration of the particles on the iris surface is almost negligible except at the lower half of the TM, where the particles are coming out from the anterior chamber, Fig. [5-3b]. The high concentration of the particles on the mid-lower corneal surface is consequence of the sharp bend of flow at the junction of the corneal and iris surface near to the TM zone. The flow has lower velocities as it approaches the lower part of TM and therefore the light pigment particles sediment on the lower corneal surface as reflected by the high concentration of particles in that region. Accumulation of pigment particles on the lower portion of the corneal surface leads to formation of KS –structure, which is observed in certain defective eye, Fig. [2-4b]. The above

simulation of the pigment particles supports this. When the particles are released form the iris surface, three patches of higher concentration of pigment granules on the corneal surface is observed, Fig. [5-3c]. The vertical patch of high concentration at the mid part of the cornea supports the formation of the KS structures sometimes observed in a diseased eye with PDS and manifests itself as a vertical spindle like structure on the mid corneal surface, Fig. [2-4a]. Kampik et al. [44] have reported the picture of deposit of pigment granules on the corneal endothelium as a vertical spindle like structure from their results of microscopy on the eyes with PDS. Their observation resembles the mid patch of high concentration in the present model and validates the capability of model to predict the behavior of deposition of pigment granules on ocular tissues. High concentration of particles on the upper part of iris surface is also observed, which reflects the tendency of flow to deposit particles in that portion when flow is rising upward along the iris surface and flow strength is reduced as it encounters the resistance from the upper TM-region and then fall down along the corneal surface. The concentration plot on the corneal surface is in agreement with the time residence plot by Heys and Barocas [23] on the corneal surface. They observed three vertical bands of high residence time on the corneal surface, which indicates probability of high concentration of pigment particles on the corneal surface however their central band is divided into two parts, which are little separated different from each other.

For the horizontal upward facing eye orientation, when the particles are released from the pupil surface, Fig. [5-4a], the particles entering with AH rise upward against gravity and approaches the central portion of the cornea. High concentration of particles is observed on the central corneal surface, where the flow stagnates due to sharp bend in the flow direction. This high concentration of pigment particles on the corneal surface is in agreement with the numerical simulation of KS formation resulting from flow through pupil aperture reported by Canning et al. [22]. On the iris surface, a circular band of high pigment concentration is observed close to the TM region, Fig. [5-4b]. The high concentration of pigment granules in a circular band is consequence

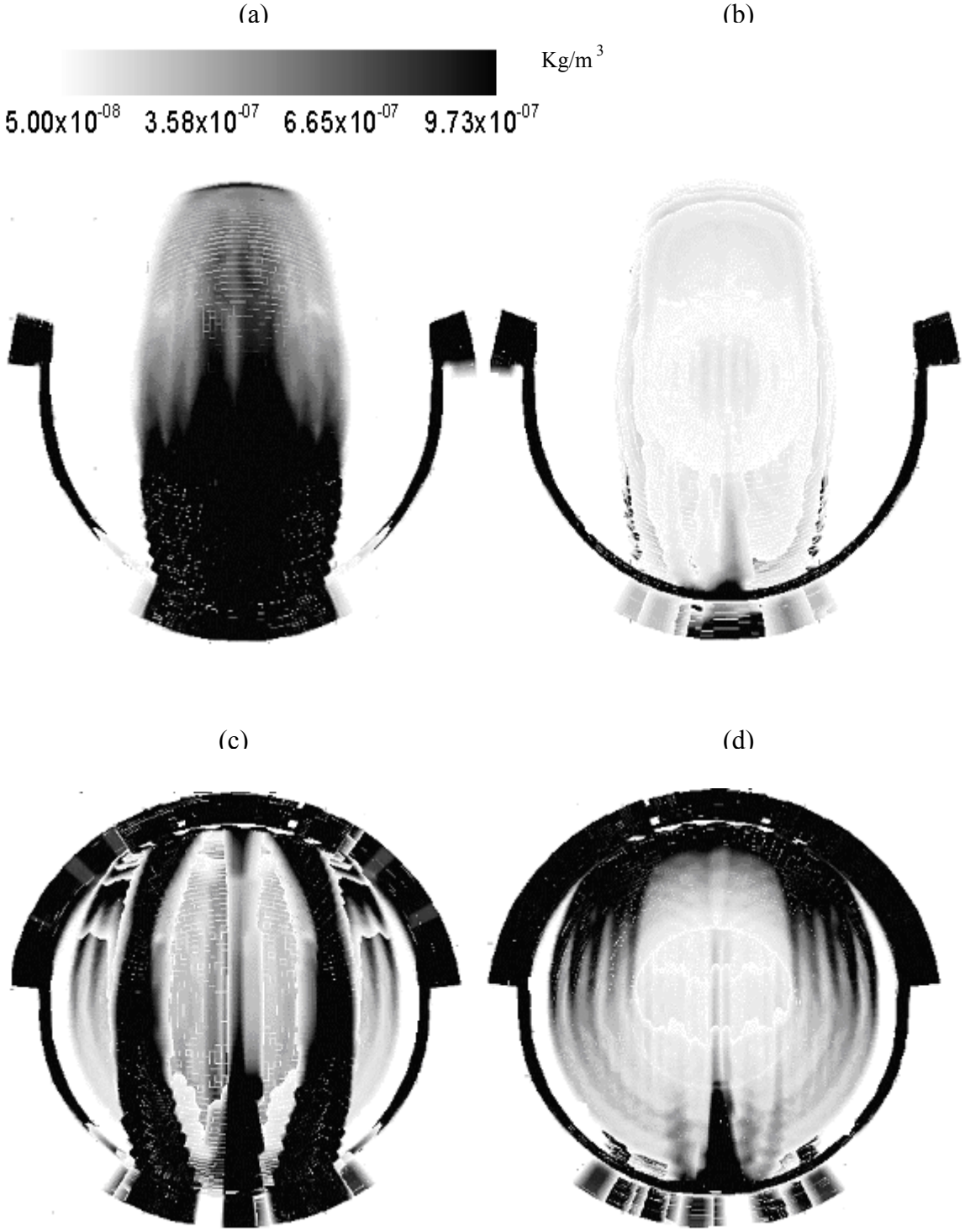

Figure 5-3: Vertical orientation (Pigment particles) (a) Particles released from the pupil surface, View from corneal surface. (b) Particles released from the pupil surface, View from iris surface. (c) Particles released from the iris surface, View from corneal surface. (d) Particles released from the iris surface, View from iris surface.

of small corner vortex next to the TM-region. The small re-circulation zone force the pigment particles falling down along the corneal surface to come close to the iris surface at the location where the flow in small corner vortex takes sharp bend towards the TM. The circular band of high pigmentation on the iris surface close to the TM region is supported by the experiments of Kampik et al. [44]. They found substantial amount of pigment particles in the anterior chamber angle of eyes with PDS. The particles released from the iris surface has possibilities of coming close to the corneal region next to its central portion, which is reflected by high concentration of particles in this region, Fig. [5-4c]. Again, on the iris surface next to the TM, a circular band of high particle concentration is found which is similar to the simulation of particles released from pupil surface, Fig. [5-4d]. For all simulations with horizontal upward facing orientation, the particles encounter high resistance while passing out through the pores of the TM and have more probability to get tucked there, which is in agreement with high concentration of particles observed in entire TM for the axis-symmetric case of horizontal upward facing orientation. Electron microscopy of TM by Kampik et al. [44] shows pigmented macrophages and pigmented endothelial cells within the TM, which supports the observation of high concentration of pigment granules in the entire TM region in the present model.

5.3 Formation of Hyphema and Corneal Blood Staining

Hyphema is a common manifestation of accumulation of blood inside the anterior chamber of eye. Any trauma of eye globe may result in tears in the anterior face of the ciliary body, disruption of arterial circle of iris or its branches or rupture of choroidal arteries. These are the major sources of bleeding inside the eye [46], which may leads to the accumulation of blood inside the anterior chamber and formation of Hyphema. In eyes with traumatic Hyphema following closed-globe injury, a secondary hemorrhage is associated with a worse visual outcome [47]. Recurrent bleeding increases the risk of vision threatening complications, including corneal bloodstaining, secondary glaucoma and optic atrophy [46]. One of the goals of the present model

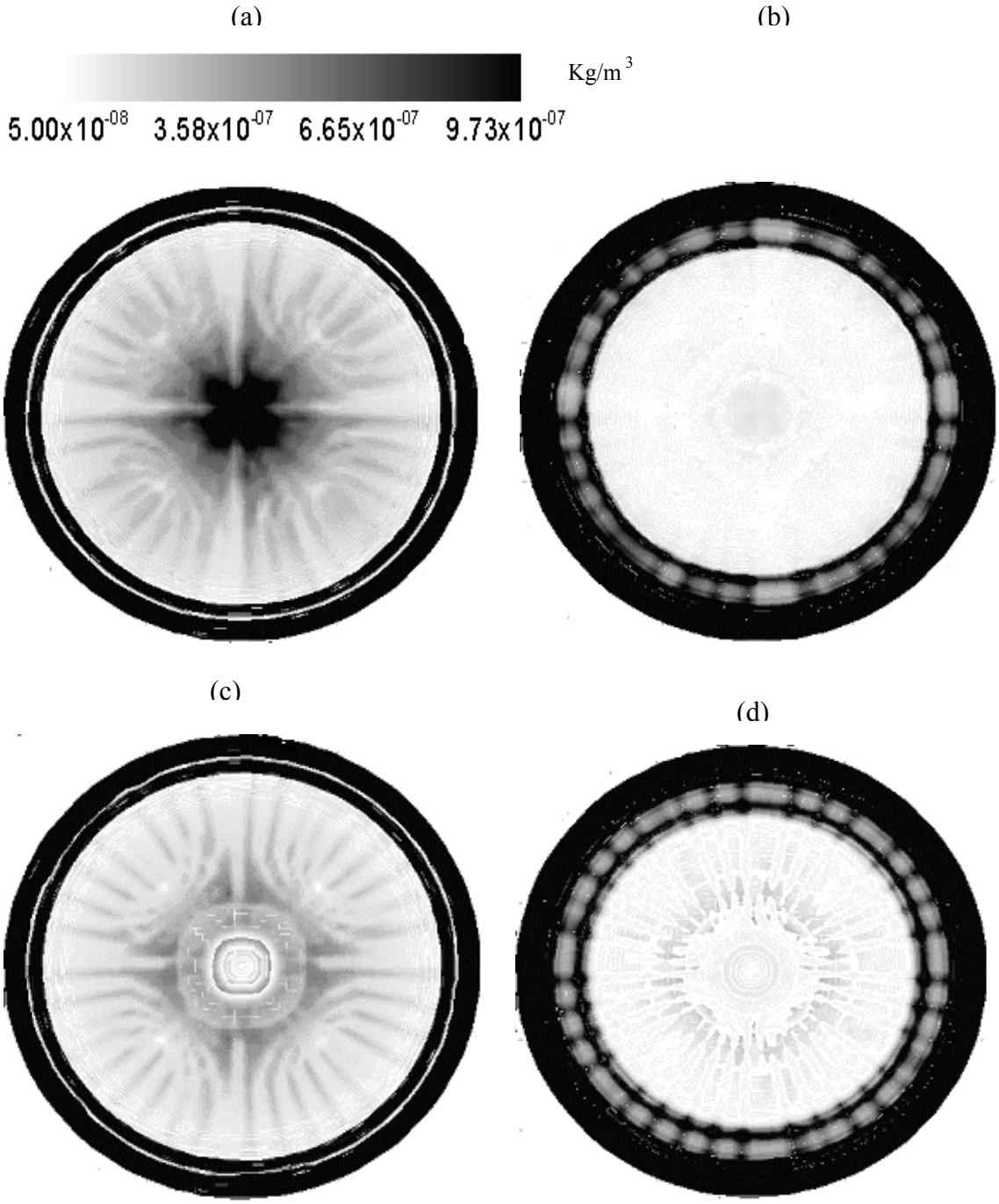

Figure 5-4: Horizontal upward facing orientation (Pigment particles) (a) Particles released from the pupil surface, View from corneal surface. (b) Particles released from the pupil surface, View from iris surface. (c) Particles released from the iris surface, View from corneal surface. (d) Particles released from the iris surface, View from iris surface.

is to simulate the accumulation of blood in the anterior chamber and analyze the formation of Hyphema structure.

For all simulations performed on the present geometrical model concerned with blood accumulation, it is assumed that the main constituent of blood, i.e. erythrocytes, represents it completely. The ghost erythrocytes are rigid cells and not much pliable to come out from the pores of TM. So, analyzing the sedimentation of erythrocytes, the diameter (7 μ m) and density (1500 Kg/m^3) of the particles is considered as that of ghost cells. For analyzing the erythrocytes generated from the sources located in the posterior chamber of eye and entering into the anterior chamber through the pupil with AH, particles are released from the points evenly spaced on the circumference of circles of different radii located on the circular aperture of inlet. Like the simulation of pigment particles, 409 particles representing the erythrocytes are released from different locations on the circular aperture with constant mass flow rate. For considering the bleeding sources of disrupted blood arteries or vessels of iris, ciliary body or TM from which blood is directly released into the anterior chamber, the erythrocytes are modeled by releasing 72 particles from the circumference of every circle located on iris surface of radii varying from 2.6mm to 5.8mm (r = 2.6, 3.2, 3.8, 4.4, 5.5, 5.8 mm).

The erythrocytes are much heavier than the pigment particles and show completely different behavior of deposition from the light pigment granules. For the vertical orientation of eye, particles released from the circular inlet aperture sediment at the bottom of the anterior chamber, Fig. [5-5a]. There is almost negligible concentration of particles on the rest part of the corneal or iris surface, Fig. [5-5a & 5-5b]. The particles released from the pupil surface circulate in the region close to the central vertical plane and do not show tendency to get deposited on the ocular tissues of the upper portion of anterior chamber. They gravitate inside the anterior chamber and give rise to the formation of layered Hyphema. The shape of the layered structure formed by the sedimentation of particles is in close agreement with the shape of commonly observed Grade-1 Hyphema, when blood occupies less than one third of the anterior chamber, Fig. [2-4c]. The shape of Hyphema formed inside the anterior chamber resembles with the pictures reported by Lai et al. [48] and Komaromy et al. [49]. Particles released simultaneously from different

locations on the iris surface shows the same tendency of sedimentation at the bottom of the anterior chamber, but in this case high concentration is also observed on the mid part of the corneal and iris surface near to the junction of these two surfaces, Fig. [5-5c & 5-5d]. Near to the junction of corneal and iris surfaces the strength of the flow is less and flow is not able to carry away the erythrocytes approaching this region. This behavior of particles resembles with the case of blood clotting on the iris surface or corneal blood staining in some cases of Hyphema. Generally corneal blood staining occurs primarily in patients who have a total Hyphema and associated prolonged elevation of IOP or if corneal endothelium has been damaged [4], but in some rare cases it may also occur in Hyphema that are not Grade-4, Fig. [5-5e]. This is the special case, when eye is severely damaged and sources are more distributed or releasing the blood at high rate [4]. The present case when erythrocytes are released from the entire iris surface is representation of this case and able to predict the possible corneal blood staining or clotting on the iris surface. Wilson, F. M. [50] reported the pictures of mild and severe corneal blood staining in cases of Traumatic Hyphema, which is in agreement with the results of corneal blood staining in the present model. Crouch and Crouch [4] reported a picture of corneal blood staining, which again resembles with the present simulation results.

For the horizontal orientation of the eye, particles released from the pupil surface has tendency to move towards the center of the pupil and get accumulated there. The particles released from the different locations on the pupil surface follow the flow profile and move towards the pupil center along the streamlines of the circulation vortex. When the flow rises against gravity along the axial direction, it is not strong enough to carry away these heavy particles against the gravity and particles sediment at the center, Fig. [5-6a]. Particles released from the iris surface get deposited on the iris surface in random fashion, but not able to rise against gravity, Fig. [5-6b].

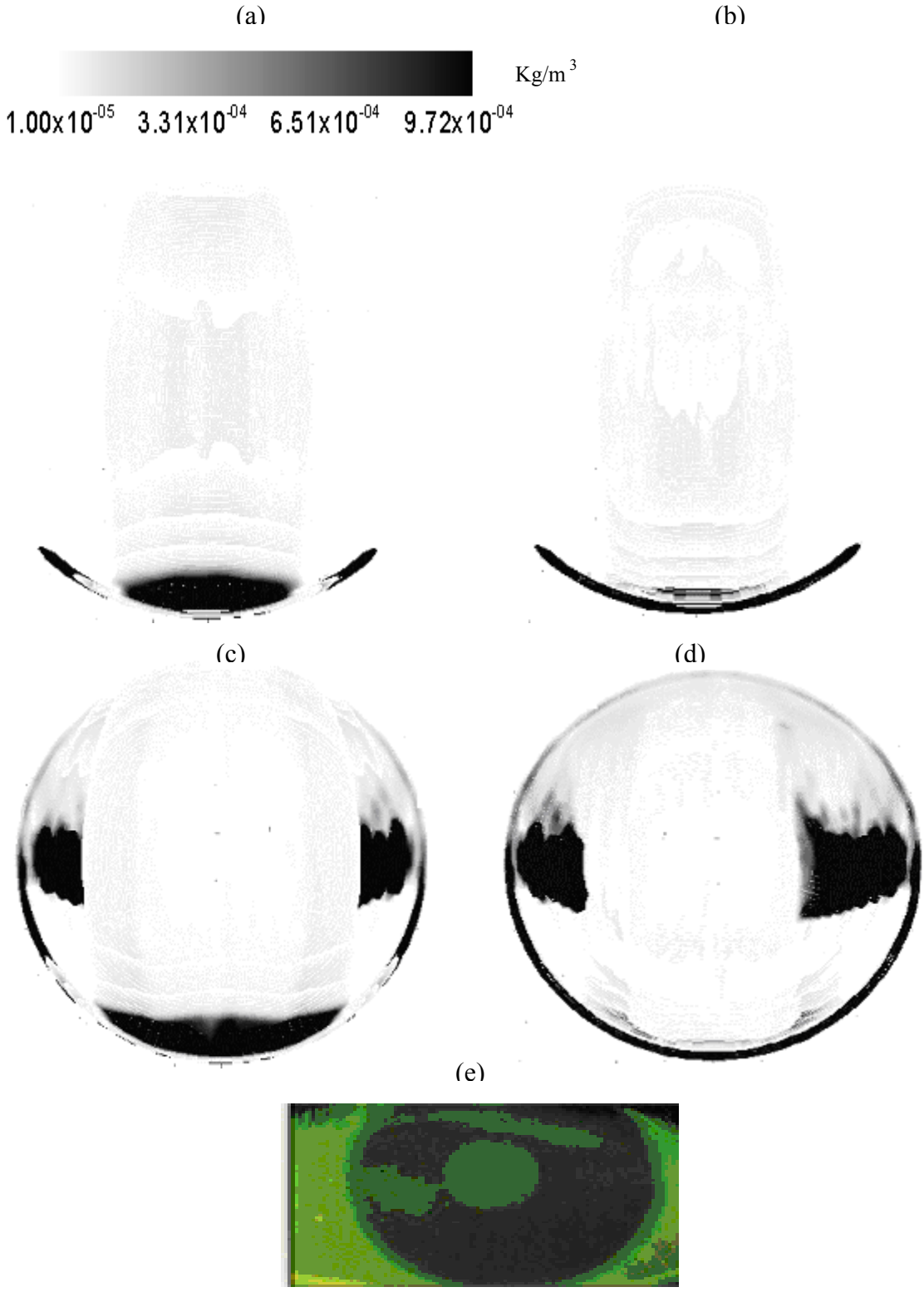

Figure 5-5: Vertical orientation (RBC) (a) Particles released from the pupil surface, View from corneal surface. (b) Particles released from the pupil surface, View from iris surface. (c) Particles released from the iris surface, View from corneal surface. (d) Particles released from the iris surface, View from iris surface (e) Corneal Staining (showed using the same fluorescein dye), Rosedale Vision Center, Kansas City, KS [51].

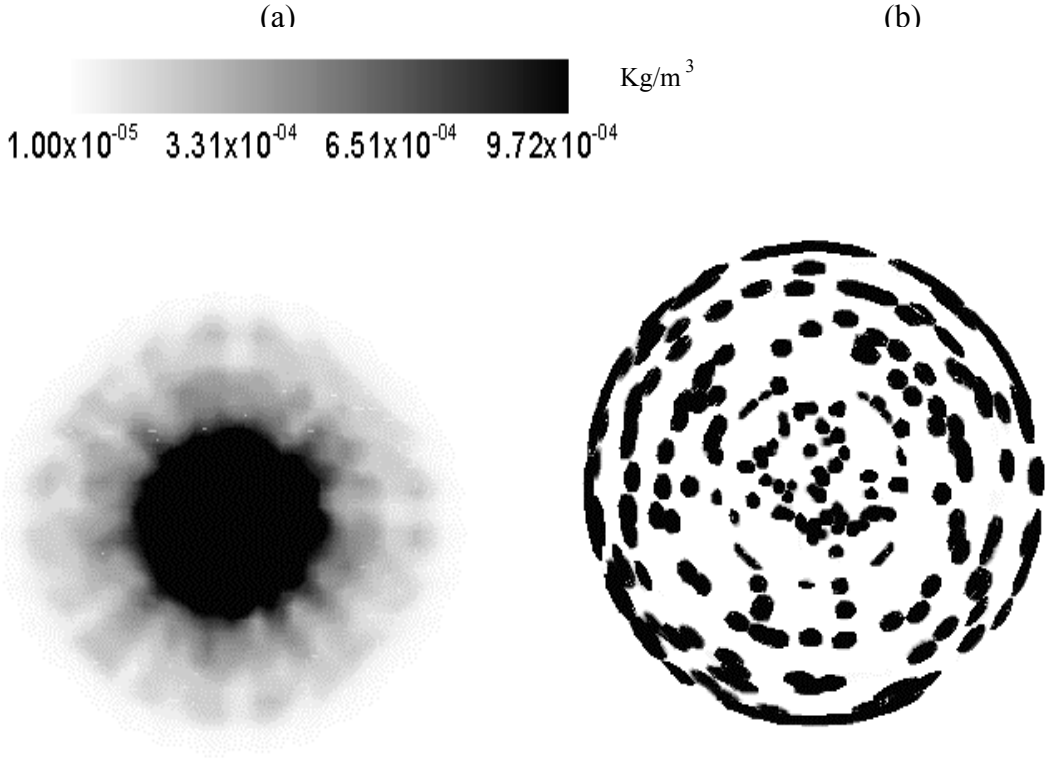

Figure 5-6: Horizontal upward facing orientation (RBC) (a) Particles released from the pupil surface, View from iris surface. (b) Particles released from the iris surface, View from iris surface.

5.4 Formation of Hypopyon

Accumulation of leucocytes inside the anterior chamber leads to the formation of layered structure commonly known as Hypopyon. These structures are not commonly observed in normal eyes, but when present are the indications of inflammation of anterior chamber which could be consequence of some detrimental disease and need serious diagnosis and treatment. One of the objectives of the present model is to analyze the behavior of leucocytes by representing them as spherical particles of diameter 10 μ m and density 1500 Kg/m^3.

For analysis of Hypopyon formation, the simulations are performed for two different sources of leucocytes. One of the sources of leucocytes is anterior surface of the iris, but they may enter into the anterior chamber through pupil from the posterior chamber. The number and rate of release of particles are kept constant similar to the simulations of erythrocytes. For the

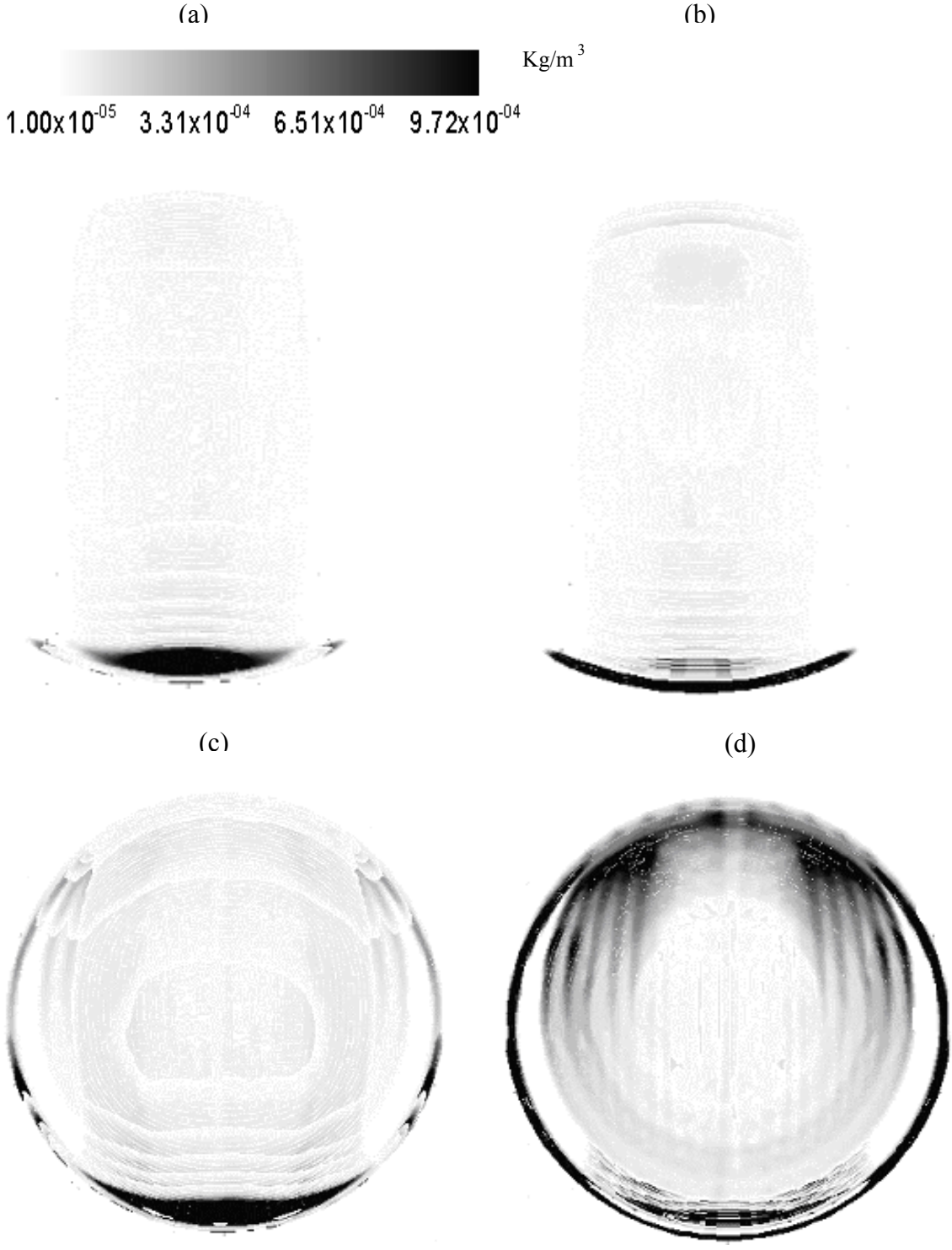

Figure 5-7: Vertical orientation (WBC) (a) Particles released from the pupil surface, View from corneal surface. (b) Particles released from the pupil surface, View from iris surface. (c) Particles released from the iris surface, View from corneal surface. (d) Particles released from the iris surface, View from iris surface.

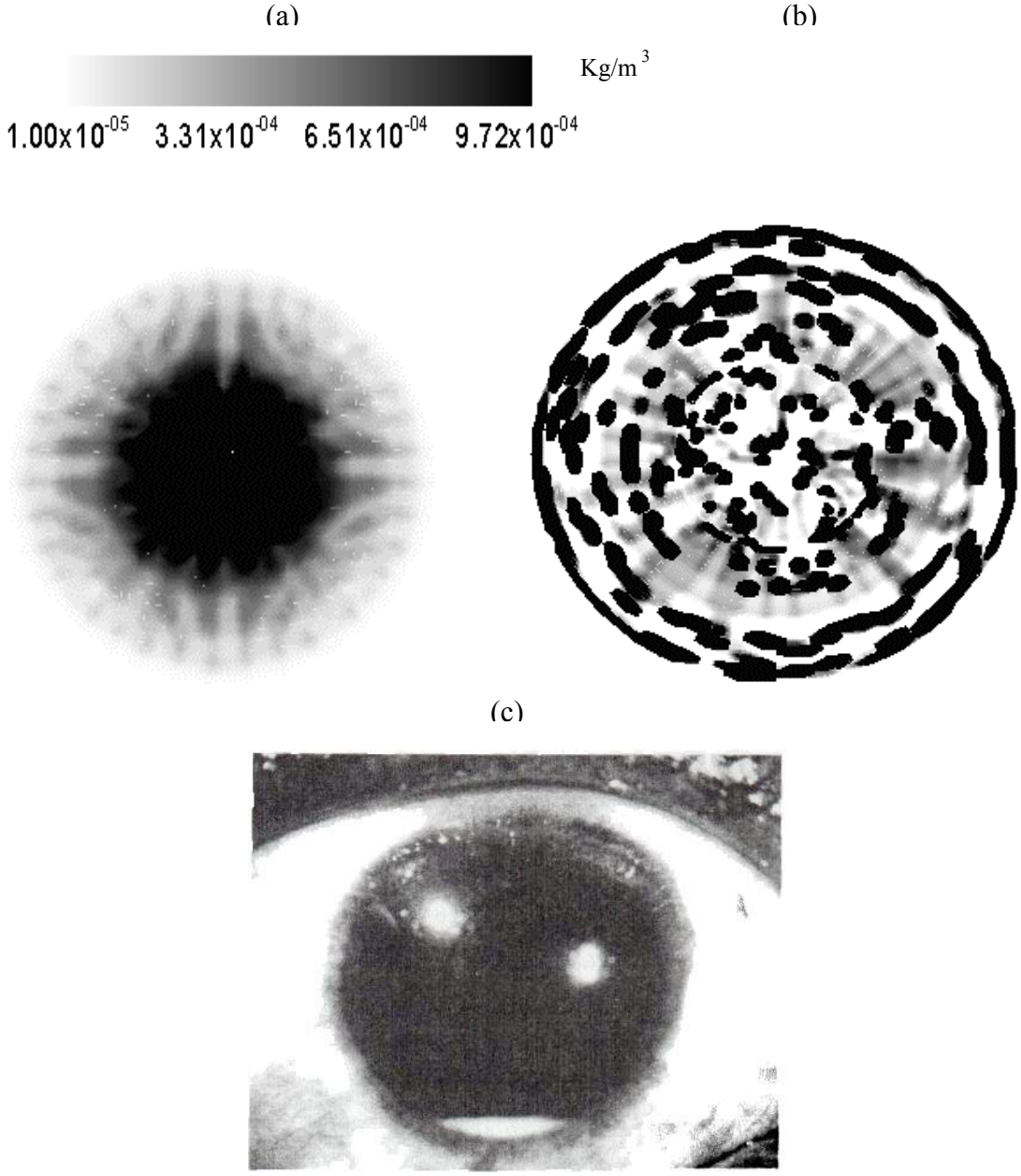

Figure 5-8: Horizontal upward facing orientation (WBC) (a) Particles released from the pupil surface, View from iris surface. (b) Particles released from the iris surface, View from iris surface. (c) A typical Hypopyon [5].

vertical orientation of the eye, the particles released from pupil surface get sedimented at the bottom of the anterior chamber like Red Blood Corpuscles, but they do not show any tendency to get deposited on other ocular tissues, Fig. [5-7a & 5-7b]. Particles released from the iris surface again show the same tendency to gravitate inside the eye Fig. [5-7c]. The shape of the Hypopyon predicted by the present model resembles with the pictures reported by Alessandro et al. [5], Fig.

[5-8c] and Olsen et al. [52]. High concentration of particles is also observed on the upper part of the iris surface, which is consequence of low strength of the flow when it rises against the gravity along the iris surface and approaches towards the upper part of the TM, Fig. [5-7d]. There is no sign of deposition of particles on the mid corneal or iris surface like in the case of erythrocytes.

For the horizontal orientation of the eye, the simulations show that WBC behave like RBC. When they are released from different locations on the pupil surface, they move towards the pupil center and get accumulated there. When they are released from different locations on the iris surface, they get distributed randomly on the iris surface, Fig. [5-8c & 5-8d].

5.5 Concluding Remarks

Simulations are performed on a three-dimensional model for the anterior chamber of eye to investigate the behavior of particles found in different pathological conditions of eye. The complex drainage system, TM, is included in the geometrical model and flow field and pressure distribution is obtained inside the anterior chamber. IOP attained inside the anterior chamber for the real pore size of the TM resembles with the IOP of normal eyes. The particle simulations are performed using this flow field and pressure distribution. The achievement of present computational model is that while simulating the particles effect of TM is included, which resists the particles to come out from the anterior chamber and plays a major role in determining the fate of these particles. This makes the simulations more realistic, which is not attempted in any previous particle simulation inside anterior chamber.

Formation of three important structures (i.e., KS, Hyphema & Hypopyon) is analyzed by using particles of appropriate size. The interaction of particles with ocular tissues is modeled by imposing different wall boundary conditions on the surfaces of geometrical model. The present model predicts the accumulation of pigment granules on the corneal surface in a particular location and specific shape, which shows close resemblance with the observed pigmentation on corneal surface in cases of some defectives eyes. Simulation of heavier particles representing erythrocytes and leucocytes give good insight about the formation of structures like Hyphema and

Hypopyon. The shapes of Hyphema and Hypopyon predicted by the sedimentation of these particles at the bottom of anterior chamber are in close agreement with the observed accumulation of blood in cases of bleeding or inflammation inside the anterior chamber. Corneal blood staining and formation of clot on iris surface is well predicted by the current model. The resemblance of most of the predicted structures by the model with the experimentally observed structures in the defective eyes reflects that model represents the real physiology of eye. The model provides the capability to further analyze the different aspects of diseases with the proper application of their particular traits and imposing right boundary conditions.

The different particles circulating inside the anterior chamber possess different sticking properties. So they interact with the ocular tissues in different manner, which is ignored in the present simulations. Some particles have tendency to clump with each other; some are more prone to get stick with the ocular tissues and some are hydrophilic in nature. Including these specific properties for the particle simulations need serious consideration. The Juxtacanalicular Meshwork (JCM) is filled with matrix gel and interaction of this part of the drainage network with AH-particles is one of the major issues, which could give valuable insight about the clogging of pores of the TM and related elevation of IOP. This is the area where detailed study is required and simulating the concerned mechanism could have good impact to the field of Ophthalmology.

Finding the circumstances, which could lead to the disruption of Hpyhema structure, will be a big help to the Medical Society. A relevant suggestion is that using cold patch treatment to eyes increases the circulation and could be helpful for the disruption of Hyphema. There is need to discover other possibilities which could be a good remedy for the Hyphema Problem. Some patients with sickle cell trait are at higher risk for developing ocular complications in case of ocular bleeding and formation of Hyphema. Mechanical obstruction of the TM by sickled erythrocytes increases the possibility of high IOP elevations in these patients. Furthermore, these eyes are more likely to develop artery occlusion and optic nerve damage. Including the specific

traits of these eyes in the numerical simulation and understanding the difference of Hyphema formation and IOP rise from normal eyes is a worth pursuing issue for future research.

Surgical intervention is needed if the Glaucoma or Hyphema problem is not resolved by the medication treatment. There are lots of surgical treatments used in Medical Science for the evacuation of sedimented and clotted particles inside the anterior chamber, which includes Vitrectomy Instrumentation, Iridectomy, Trabculectomy etc. These treatments are mostly associated with ocular incision in iris or TM to reduce the outflow resistance of eye drainage system and release the high pressure developed inside the anterior chamber to acquire the normal IOP. All these surgical treatments could be modeled to some extent of accuracy for a proper visualization of readjustment in flow field and pressure distribution, which is difficult to understand by experiments.

In, conclusion the three-dimensional model presented in this paper provides capability to analyze the AH-particles movement, their interaction with ocular tissues and formation of some structures associated with specific eye diseases.

CHAPTER 6. SIMULATION IN HUMAN EYE

6.1 Geometrical Model of the Human Eye

In this section attention is focused on human eye, whose shape and geometry is slightly different from that of the rabbit eye. The depth of the anterior chamber of human eye is approximately 3 mm [10] and diameter in the plane of the iris root is 11-12 mm [10]. The anterior chamber is modeled as part of a sphere of radius 7.2 mm [10] and thickness along the central axis as 3 mm, Fig [6-1b]. The anterior chamber is surrounded by the inner surface of the cornea and by the inner surfaces of the trabecular meshwork. The cornea is modeled as rigid shell with thickness of 0.6 mm along the central axis and thickness of 1.0 mm towards the periphery where it merges with sclera, Fig [6-1a]. On the posterior side, the anterior surface of the iris and the pupillary portion of the anterior lens surface bound the anterior chamber. The iris, which is a front extension of the ciliary body, has a slightly elliptical shape with a vertical axis of 11-12 mm long. It is perforated by a pupil, which changes its diameter depending on the amount of the light falling on the eyeball. The iris is modeled as a rigid elliptical disc of uniform thickness of 0.4 mm with a circular hole of radius 2 mm [23] at the center, Fig [6-1c]. The circular aperture at the center represents the pupil from which flow enters into the anterior chamber from the posterior chamber. The anterior and posterior surfaces of the iris are modeled as part of spherical surfaces of radius 21.6 mm and 22.1 mm respectively.

The posterior chamber is located at the back of the anterior chamber, which is bound posteriorly by the zonular fibers; anteromedially by the contact of the iris with the lens; anteriorly by the pigment epithelium of the posterior iris surface and anterolaterally by the junctional zone of the iris and ciliary body. The zonular fibers are treated as a plane surface bounding the posterior chamber from the vitreous side. The biconvex crystalline lens located at the back of the anterior chamber is modeled as an ellipsoid of equatorial diameter 9 mm and with the dimensions of other two diameters being 4 mm. The AH secreted in the posterior chamber by the ciliary body

enters the anterior chamber through the small gap between the iris and lens which is estimated to be few microns ($\approx$10-25 μm) wide [23]. The curved boundary surrounding the posterior chamber is treated as ciliary body, which secrets the fluid at constant volume flow rate of 2.5 $\mu L/\min$. The gap between the iris and lens surface is 25 μm at the iris tip for all the simulations performed in normal eyes, while for the simulations concerned with the pupillary block it is taken as 3 μm.

As noted earlier, the TM is treated as annular porous zone at the bottom of the anterior chamber. It is assumed to have a thickness of 0.4 mm along the axial direction and an annular radius of 1.2 mm. The part of the TM immediately adjacent to the anterior chamber is the Uveal meshwork followed by the Corneoscleral meshwork. This part of the meshwork has negligible resistance to outflow due to its bigger pore size. We treat this part of TM as a porous jump interior surface at the entry of the annular porous zone with 0.2 mm thickness and a resistance coefficient corresponding to 100 microns pore size. The porous jump interior surface is a thin porous medium of finite thickness over which the pressure change is defined as a combination of Darcy's Law and an additional inertial loss term. The pressure gradient across the porous jump surface is given by equation (4) and the coefficients of the equation are used corresponding to porous bed of 0.5 void fraction and 100 microns mean particle diameter. The remaining part of TM is treated as a porous zone (packed bed) with a specified average pore size and a void fraction of 0.5.

The cornea is a vascular and transparent tissue with thermal properties close to that of water. It is kept a constant temperature (T_C) of 308 K in the present model. The temperature drop between the iris and the cornea (generally considered to be in the 2-4 ^0C for the open eye) provides the buoyant force mechanism to drive the AH. The AH is assumed to be linear viscous liquid with properties close to those of water.

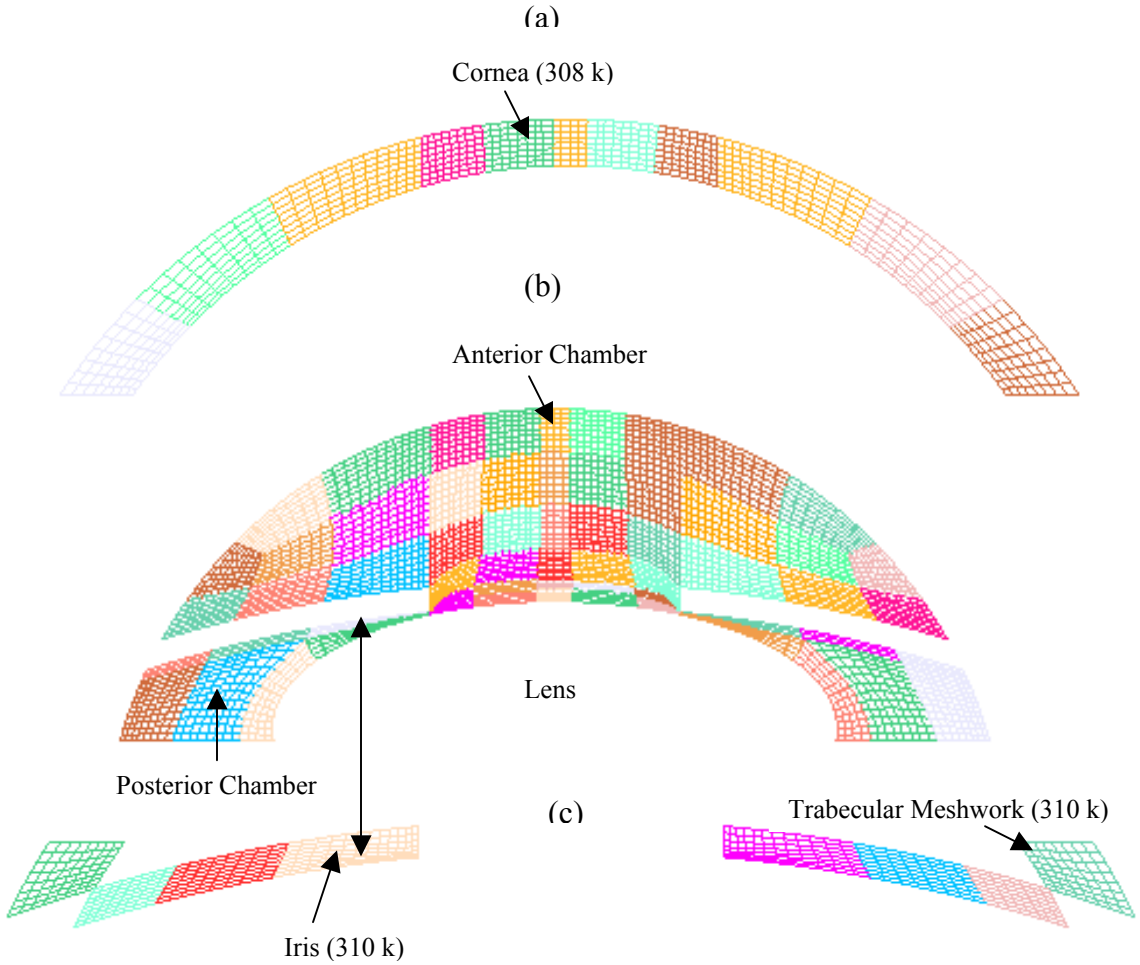

Figure 6-1: Cross-section of mesh in vertical mid-plane of the eye-model. (a) Cornea (b) Anterior chamber (c) Iris and TM.

The commercial package GRIDPRO was used in the grid generation process, and only hexahedral cells of aspect ratio less than five in the computational domain is used. The entire geometry is divided into 800 blocks. For the cases reported in the present study, 500,000 hexahedral cells are used. To demonstrate grid independence, simulations are run 1000,000 cells. Less than 1 % variation in the magnitude of the maximum velocity is observed between the 500,000 cell calculation and the 1000,000 cell calculation and justifies the use of 500,000 cells for the simulations.

6.2 Boundary Conditions

The iris disc and corneal shell are modeled as stationary rigid tissues and no-slip boundary conditions are imposed on the boundaries of these tissues. The curved lens surface and the plane zonular fiber surface are also treated as walls with no-slip boundary conditions imposed. To satisfy the normal secretion rate from the ciliary body into the posterior chamber, the mass flow inlet condition is imposed on the ciliary body surface. The mass flow rate is kept constant at $4.167 * 10^{-8}$ (= 2.5 $\mu L / \min$) and flow direction is kept normal to the boundary of the ciliary surfaces. Since most of the flow drains out to aqueous veins passing radially through the TM, and the collector channels, the upper and lower surfaces of the annular TM are assumed to be impermeable walls (no-slip boundary condition). The pressure in the aqueous veins under normal condition is 9 mm of Hg [17], so the outlet boundary is treated as pressure outlet boundary condition with a specified pressure of 9 mm of Hg (1.2 kPa). The inclusion of the TM in the present simulation, and the incorporation of a realistic pressure outlet boundary condition, is a distinct improvement over previously reported efforts [7, 16-23].

The surfaces of TM, iris, ciliary body, lens and zonular fibers are treated as constant temperature walls at core body temperature ($37^0 C$). The temperature of the cornea is set at constant value of 308 K, which is used in the previous simulations on the eye model.

6.3 Flow Simulation

6.3.1 Velocity Contours

Gravity plays a major role in determining the flow pattern of AH inside the anterior chamber. In the horizontal upward-facing position, (Fig [6-2a]) the gravity direction is perpendicular to the iris surface, and the flow field is axis-symmetric. In the vertical orientation (Fig [6-2b & 6-2c]), gravity destroys the symmetry in the vertical (Y-Z) plane. For these two orientations, the flow profiles and re-circulation zones are completely different. For the horizontal position, the warmer fluid entering the pupil rises upward, and moves down the corneal surface

leading to large symmetric re-circulation zone. The highest velocities (133 μm /s) occur midway along the vertical axis of symmetry. All features of the flow field are identical about the vertical axis of symmetry including the exit flow rates through the left and right TM. For the vertical orientation of the eye, the warmer fluid rises upward along the iris surface and then turns downwards as it encounters the higher resistance in the upper TM regions. The flow then descends along the corneal surface toward the lower TM. The streamlines plotted in the horizontal mid plane passing through the center of the pupil reflect the flow path of AH, (Fig [6-2c]), and show a helical path toward the TM. A portion of the recirculating flow exits through the small pores of the TM. The highest velocities are located near the middle of the iris surface (0.321 mm/s) and just upstream of the mid-corneal surface (0.325 mm/s). The stagnation zones and regions of large curvature are of special interest because particles or cells in the AH can get trapped in these regions and lead to the development of blockages, which can obstruct the vision or increase the IOP (e.g., as in pigmentary glaucoma). Clearly, in the vertical orientation the iris and the corneal surface are subjected to higher shear stresses than in the horizontal orientation.

6.3.2 Pressure Contours

The pressure variations in the anterior and posterior chamber region are considerably smaller than the pressure drop across the porous TM. In the horizontal orientation, the variation in the pressure of the anterior chamber is less than 0.01 Pa, which indicates that the anterior chamber pressure is nearly constant, Fig [6-3a]. Heys et al. [7] also report in their simulations of an eye model that the pressure is essentially uniform inside the anterior chamber; the present model supports this observation. Along the TM, from the anterior chamber to the aqueous veins, the pressure decreases from the normal IOP of 15mm of Hg (~1.94 Kpa) [17] inside the anterior chamber to 9 mm of Hg (~1.2 Kpa) [17] corresponding to the pressure in the veins. The pressure variations in the TM are relatively linear along the radial direction in the horizontal planes parallel to the iris surface, and appear to be essentially uniform along the normal to the iris surface. Therefore the flow in the TM regions is essentially radially outwards from the anterior

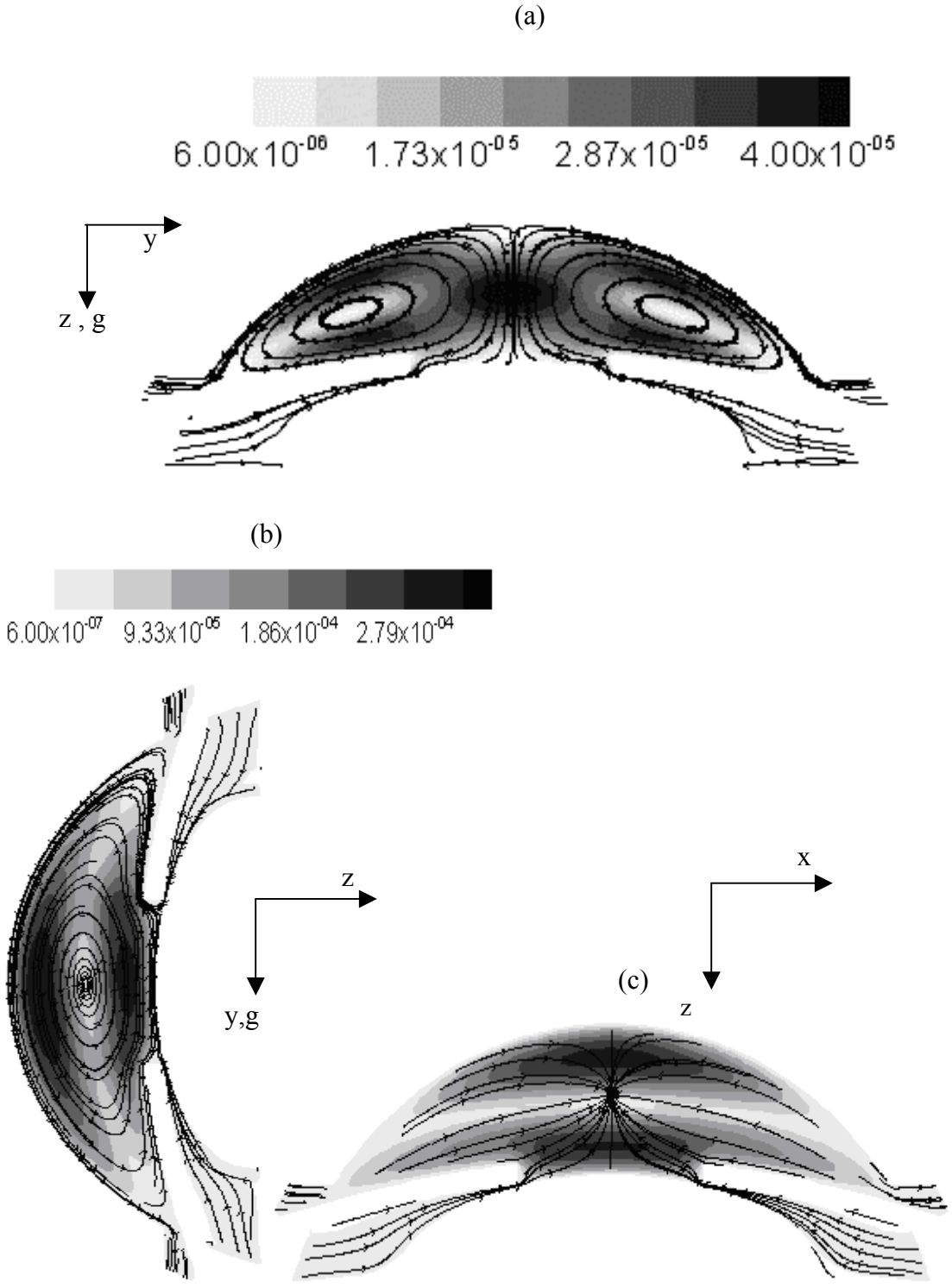

Figure 6-2: Streamlines and contours of velocity magnitude. (a) Horizontal orientation, Vertical mid plane (b) Vertical orientation, Vertical mid plane (c) Vertical orientation, Horizontal plane. $\Delta T = 2^{0} C$, Pore diameter = 0.9 μ .

chamber to the aqueous veins. There is no significant variation in the pressure in the posterior chamber.

For the vertical orientation, pressure contours are plotted over a small range to investigate the pressure distribution in the anterior and posterior chambers, Fig [6-3b]. Like the horizontal orientation, the pressure in anterior chamber is nearly constant and the pressure drops linearly across the TM from 15 mm of Hg to 9 mm of Hg. The gradual decrease of pressure from the upper portion to the lower portion in the posterior chamber is the consequence of buoyancy. As flow in the upper half stagnates, high pressure is observed in the upper part of the posterior chamber.

6.3.3 Temperature Contours

Contour plots for the temperature are shown in Figure [6-3c & 6-3d] for both the horizontal and vertical orientations of the eye. For the horizontal orientation, the AH is heated as it moves upwards towards the center of the pupil along the heated iris surface. Consequently, the temperature gradient decreases from the iris root to the pupil center. In the anterior chamber the AH rises against gravity in the middle towards the cornea and as it moves down the corneal surface, it is cooled, Fig [6-3c]. The largest temperature gradients are located at the stagnation point (mid-point of the corneal surface) and these temperature gradients diminish rapidly as the flow descends along the cooler corneal surface. For the vertical configuration, the temperature gradient is relatively high close to the lower root of the iris, which diminishes as flow rises vertically upwards along the heated iris surface, Fig [6-3d]. Along the corneal surface the highest temperature gradient occur close to the upper regions where the flow turns toward the cooler corneal surface due to resistance of the upper part of the TM. The flow is cooled while descending along the corneal surface, and temperature gradients attain the lowest values near the lower part of the TM.

6.4 Formation of Krukenberg Spindle

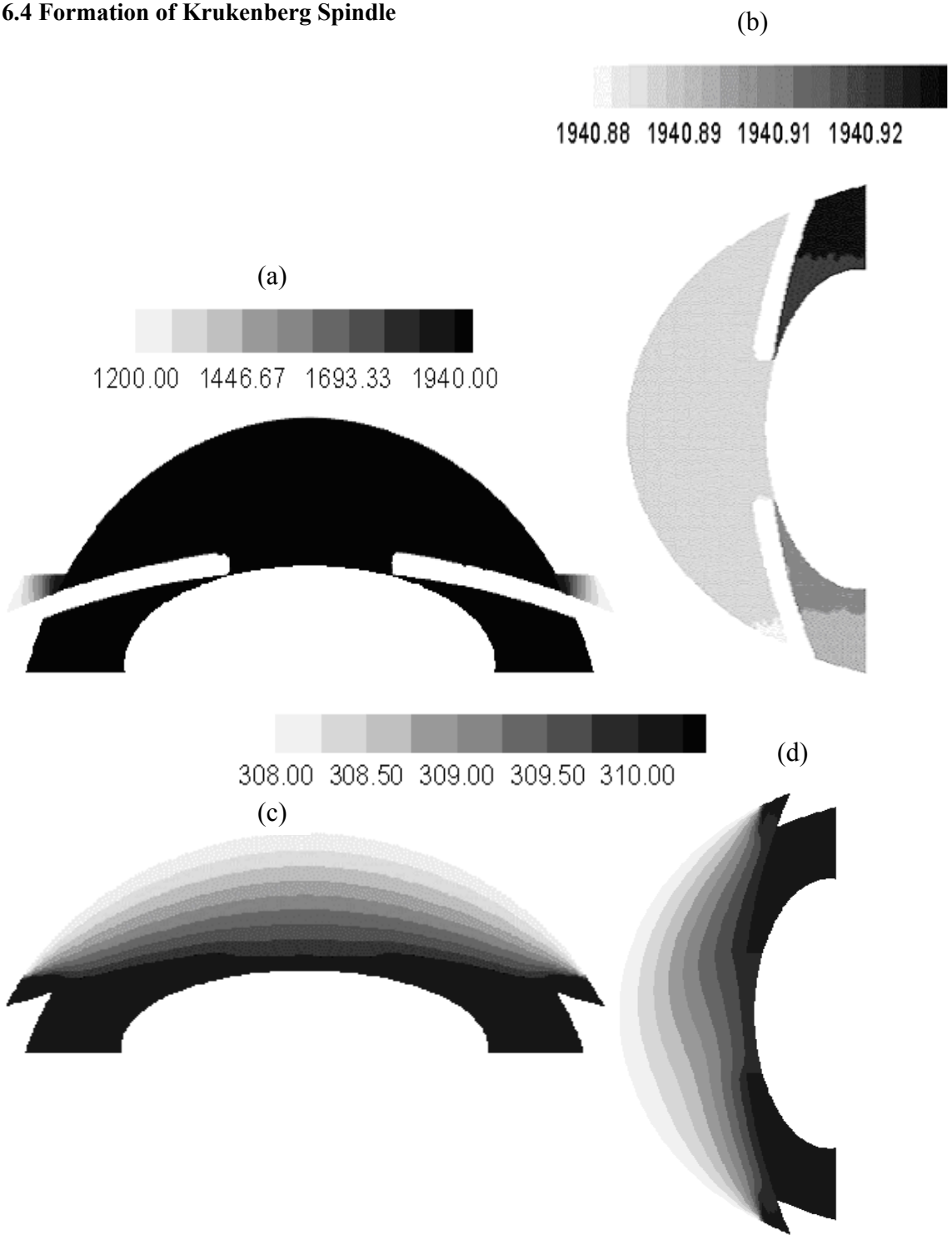

Figure 6-3: Pressure contours in the vertical mid plane. (a) Horizontal orientation (b) Vertical orientation. Temperature contours (c) Horizontal orientation. (d) Vertical orientation, $\Delta T = 2^{0} C$, Pore diameter = 0.9 μ.

As in the simulations for the rabbit eye, pigment granules are released from two different sources located inside the human eye geometry. (a) For considering the pigment granules shedded from the pigmentary layer of posterior iris surface, particles are released from the points evenly spaced on the circumference of the circles of different radii located on the posterior surface of the iris at different horizontal planes (xy-planes). Particles (72) are released from the circumference of every circle of radii varying from 3.20 mm to 4.00 mm (r = 3.20, 3.36, 3.52, 3.68, 3.84, 4.00 mm) in the posterior chamber, which are entrained into the AH and enter the anterior chamber through the pupil. (b) Pigment particles generated from the anterior surface of the iris are modeled by releasing 72 particles from the circumference of every circle of radii varying from 3.70 mm to 4.50 mm (r = 3.70, 3.86, 4.02, 4.18, 4.34, 4.50). The mass flow rate of these particles is kept constant such that concentration of the pigment granules inside the anterior chamber would be in the agreement with the experimental results of Kuchle [25].

For the vertical orientation of eye, when the particles are released from the posterior iris surface, three patches of high concentration pigment granules is observed on the corneal surface, Fig [6-4a]. The concentration of particles is relatively high at the portion of patches close to the lower corneal surface. High concentration of particles on the posterior iris surface is observed as some of the particles released from posterior iris surface remain close to the posterior iris surface for long residence time and are not able to enter into the anterior chamber, Fig [6-4b]. When the particles are released from the anterior iris surface, high concentration of particles is observed along the mid lower corneal surface regions, Fig [6-4c]. High concentrations are also observed along the mid and upper portions of the cornea, Fig [6-4c], but these concentrations are smaller relative to those observed in the lower portion. High concentration of the particles on the mid-lower corneal surface is consequence of the sharp bend of flow at the junction of the corneal and iris surface near to the TM zone. The flow has lower velocities in the region. So there is a tendency for the lighter pigment particles to sediment on the lower corneal surface. These concentration plots are in agreement with the observed trend in the rabbit eye and also supports

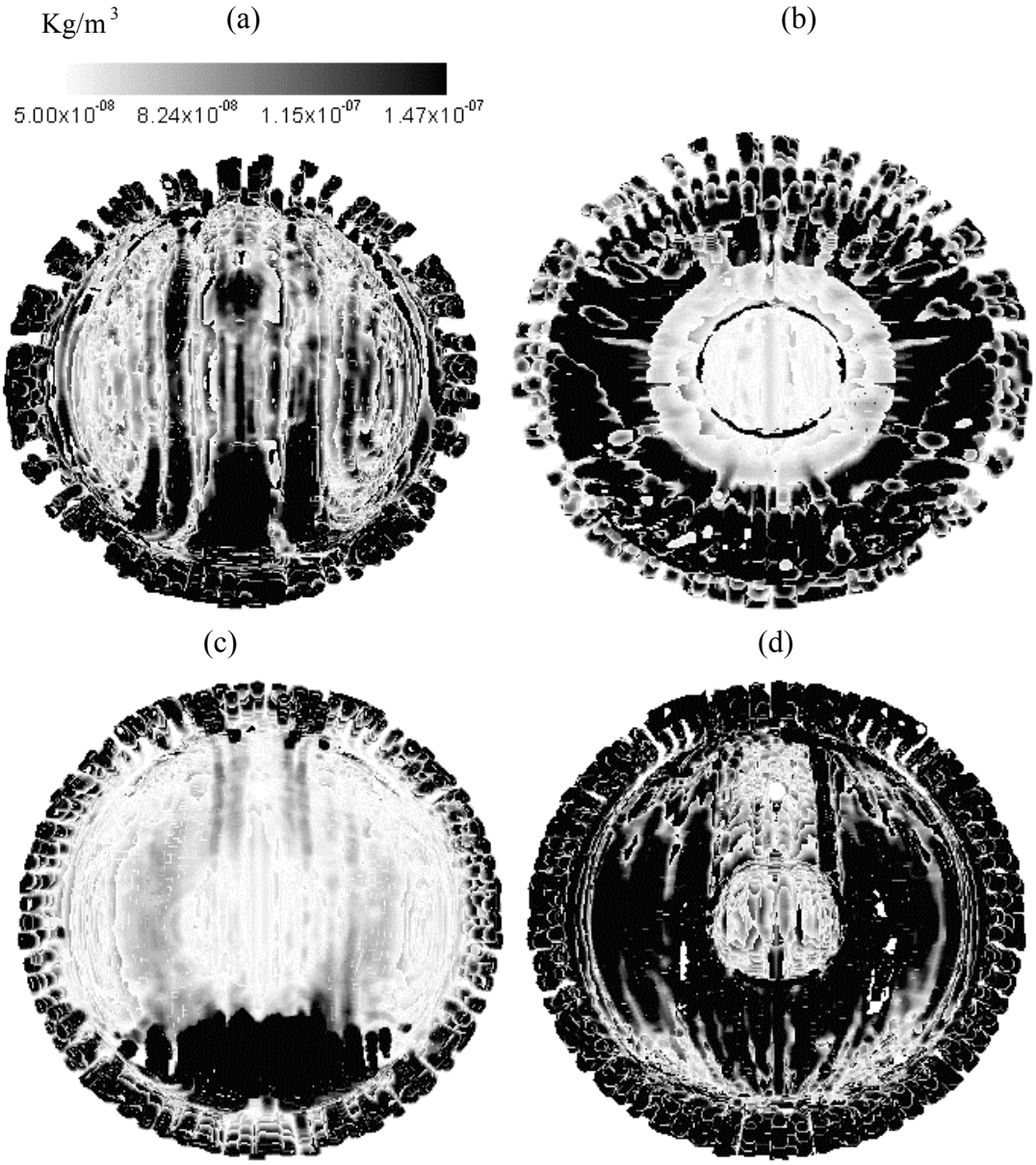

Figure 6-4: Vertical upward facing orientation (Pigment particles) (a) Particles released from the posterior iris surface, View from corneal surface. (b) Particles released from the posterior iris surface, View from iris surface. (c) Particles released from the anterior iris surface, View from corneal surface. (d) Particles released from the anterior iris surface, View from iris surface.

the formation of the KS structures sometimes observed in the diseased eye with PDS as a vertical spindle like structure on corneal surface, Fig [6-4a & 6-4b]. High concentrations of particles are also observed on the anterior iris surface along the mid portion of the iris surface on both sides of pupil, Fig [6-4d]. This is consequence of the convex shape of the anterior iris surface. Some of the particles released from the lower and mid regions of the anterior surface near to iris root are

not swept upwards by the weak flow in this region and therefore have long residence times in the vicinity of the anterior surface. For both sources of pigment particles (posterior or anterior), high concentrations are observed in the region of TM as particles escaping from the anterior chamber pass through the TM. Therefore, there is a high probability of pigmentation of TM since pigment granules pass through the pores of TM and are deposited on the TM tissues.

For the horizontal upward facing eye orientation, when the particles are released from the posterior iris surface, Fig [6-5a], the particles entering into anterior chamber with the AH rise upward against gravity and approach the central portion of the cornea. High concentration of particles is observed on the central corneal surface, where the flow stagnates due to the corneal resistance. On the iris surface, a circular band of high pigment concentration is observed close to the TM region, Fig [6-5b]. The high concentration of pigment granules in a circular band is consequence of the sharp flow turn next to the TM-region leading to a corner vortex. This small corner vortex next to the TM recirculate the pigment particles falling down along the corneal surface and bring them come close to the iris root where the particles deposit. The particles released from the anterior iris surface are transported upwards to the corneal region, and this is reflected by the high concentration of particles in this region, Fig [6-5c]. On the iris surface the circular band of high particle concentration next to TM is found, and is similar to that observation when the particles are released from posterior iris surface, Fig [6-5c]. For all simulations with horizontal upward facing orientation, the particles encounter high resistance while passing out through the pores of the TM and have more probability to deposit. This is in agreement with high concentration of particles observed in the entire TM for the symmetric case of horizontal upward facing orientation.

For both the horizontal and vertical orientations of eye, the concentration plot of pigment particles on the corneal surface resemble the simulations inside the rabbit eye, but the

concentration plot on the iris surface shows different behavior. This is due to the concave shape of the iris in human eye model.

6.5 Formation of Hyphema

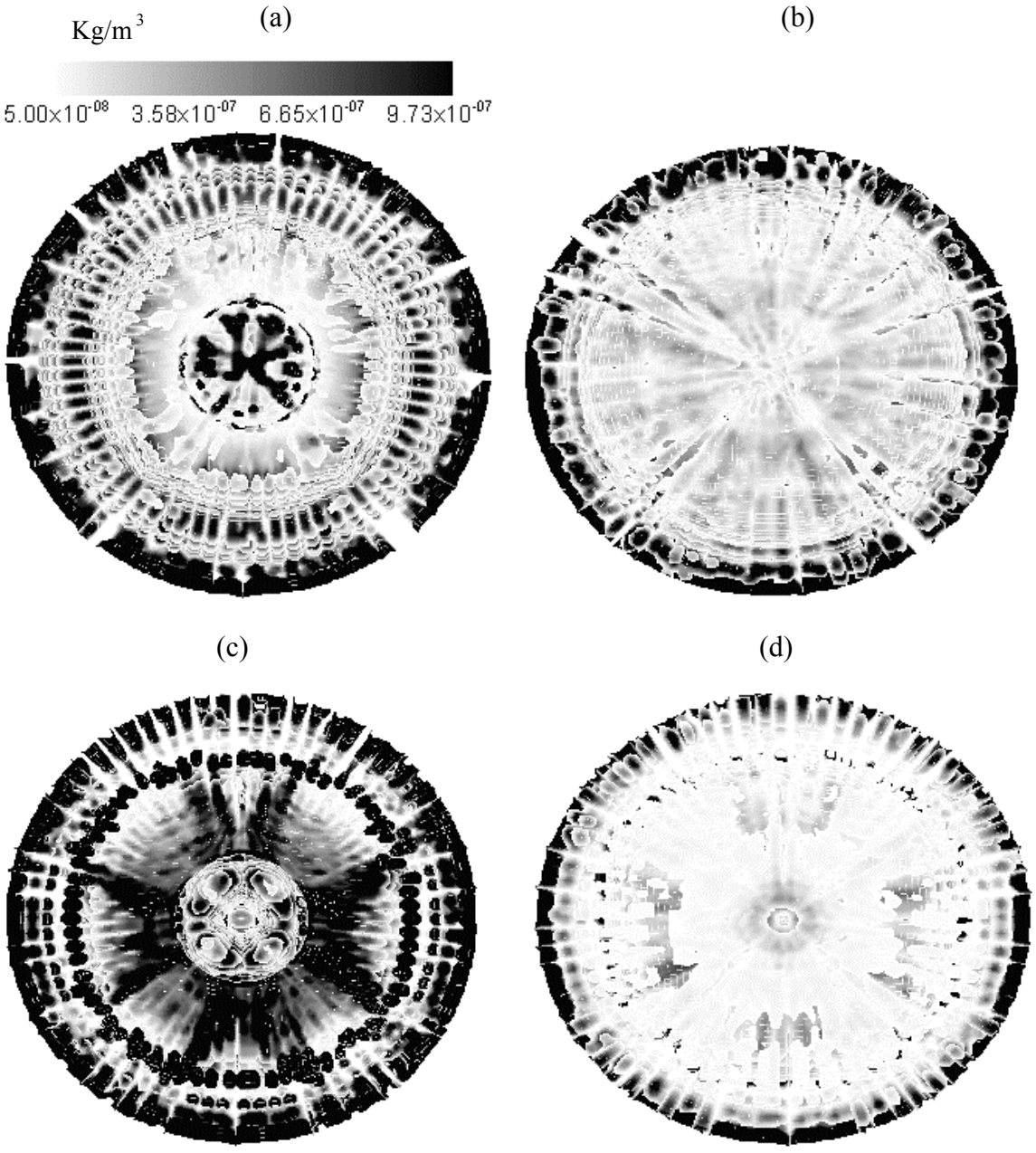

Figure 6-5: Horizontal upward facing orientation (Pigment particles) (a) Particles released from the posterior iris surface, View from corneal surface. (b) Particles released from the posterior iris surface, View from iris surface. (c) Particles released from the anterior iris surface, View from corneal surface. (d) Particles released from the anterior iris surface, View from iris surface.

There are two different sources of erythrocytes (posterior and anterior) inside the eye. For the erythrocytes generating from the sources located in the posterior chamber of eye, particles of 7 μ m diameter are released from the points evenly spaced on the circumference of the circles of different radii located on the posterior surface of the iris at different horizontal planes (xy-planes). Particles (72) are released from the circumference of circles of radii varying from 3.20 mm to 4.00 mm (r = 3.20, 3.36, 3.52, 3.68, 3.84, 4.00 mm) in the posterior chamber.

For sources of erythrocytes arising from disrupted blood arteries or vessels of iris, ciliary bodies or TM from which blood is directly released into the anterior chamber, the erythrocytes are modeled by releasing 72 particles from the circumference of every circle located on anterior iris surface of radii varying from 3.70 mm to 4.50 mm (r = 3.70, 3.86, 4.02, 4.18, 4.34, 4.50).

For the vertical orientation of the eye, particles released from the posterior iris surface sediment at the bottom of the anterior chamber, Fig [6-6a]. There is almost negligible concentration of particles on the rest part of the corneal surface, Fig [6-6b]. The heavy particles released from the posterior iris surface do not come close to central portion of the cornea while circulating inside the anterior chamber. These particles gravitate inside the anterior chamber like the particles released from the pupil surface in the rabbit eye model. The shape of the layered structure formed by the sedimentation of particles is in close agreement with the shape of commonly observed Grade-1 Hyphema, Fig 2 [c]. High concentration of particles on the lens surface is also observed, which reflects the possibilities of blood staining of the lens when the source of erythrocytes are located in the posterior chamber, Fig [6-6b]. There are patches of low concentration of blood particles on the part of the iris just above the pupil aperture, Fig [6-6b]. The particles coming from posterior chamber through the pupil rises against the gravity along the iris surface with the flow and few of them get deposited at the upper part of the iris next to the pupil aperture. This supports the observation of blood clotting on the iris surface in some cases of Hyphema. Particles released simultaneously from different locations on the anterior iris surface show the same tendency of sedimentation at the bottom of the anterior chamber, but in this case

high concentration is also observed on the mid part of the corneal surface close to TM, Fig [6-6c]. The flow velocities are low close to the junction of iris and corneal surface. Thus the flow is not able to carry away the erythrocytes approaching this region, which leads to the deposition of particles in this region. This behavior of the particles resembles with the case of corneal blood staining in some cases of Hyphema. A similar trend is also observed for rabbit eye simulations.

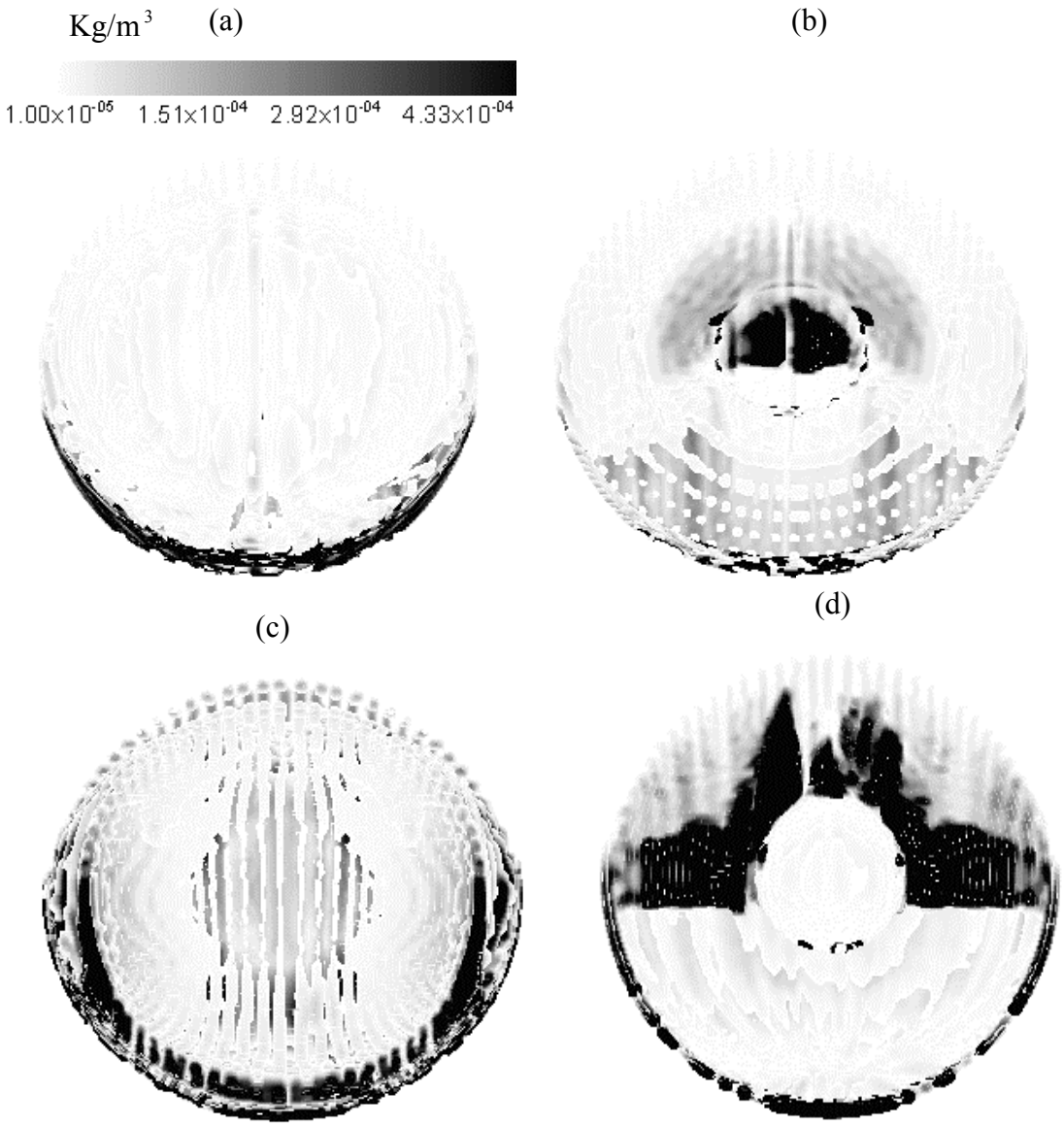

Figure 6-6: Vertical upward facing orientation (Erythrocytes) (a) Particles released from the posterior iris surface, View from corneal surface. (b) Particles released from the posterior iris surface, View from iris surface. (c) Particles released from the anterior iris surface, View from corneal surface. (d) Particles released from the anterior iris surface, View from iris surface.

High concentration of particles is observed on the iris surface on both sides of the pupil aperture and above the pupil aperture, which is representation of the blood clotting on the iris surface, Fig [6-6d].

For the horizontal orientation of the eye, particles released from the posterior iris surface move in the vicinity of the iris surface in the posterior chamber. Most of them are not able to

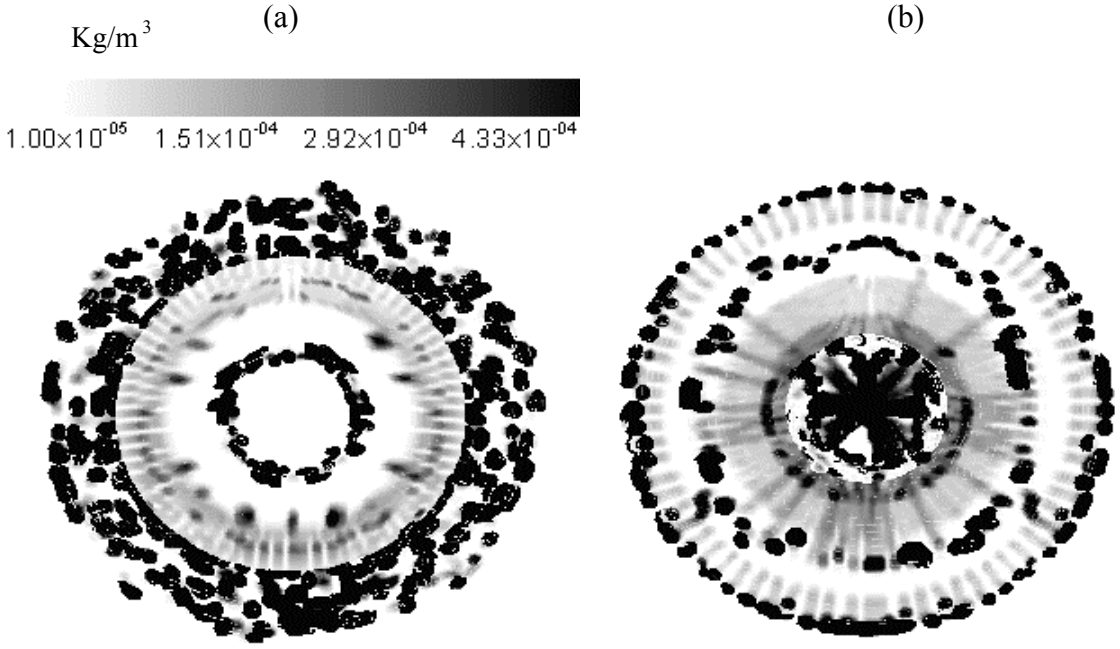

Figure 6-7: Horizontal upward facing orientation (Erythrocytes) (a) Particles released from the posterior iris surface, View from iris surface. (b) Particles released from the anterior iris surface, View from iris surface.

enter into the anterior chamber, which is reflected by high concentration of particles on the posterior iris surface, Fig [6-7a]. Some of the particles entering into the anterior chamber are not transported by the flow into the anterior chamber and get deposited either on lens surface or near to the peripheral iris tip, Fig [6-7a]. The particles released from the anterior iris surface in the region close to TM get deposited on the iris surface, Fig [6-7a], while the particles released from the region close to the pupil aperture follow the flow profile and move towards the center of the iris surface along the streamlines of the circulation vortex. When the flow rises against gravity along the axial direction, it is not strong enough to carry away these heavy particles against the

gravity and particles sediment at the center, Fig [6-7b], which is reflected by high concentration of particles at the center (lens surface).

CHAPTER 7. IRIDECTOMY

7.1 Pupillary Block and Angle-Closure Glaucoma

Pupillary block is defined as anterior convexity of the iris, Fig. [7-1a & 7-1b]. This leads to a degree of resistance at the irido-lenticular interface sufficient to produce a pressure differential across the iris. Pupillary block is the most common form of angle-closure glaucoma. Resistance to aqueous movement from its site of production by the ciliary epithelium within the posterior chamber through the pupil produces a pressure gradient across the iris, which forces the iris anteriorly, into the trabecular meshwork [53]. This results in closing the anterior chamber angle and blocking the access of the AH to the main drainage area TM, Fig. [7-1a & 7-1b]. The blockage of the anterior chamber angle leads to rise in IOP depending on the degree of iris bulging and angle closure. In an acute attack, complete blockage of the access to the trabecular meshwork occurs and the intraocular pressure rises rapidly, often to very high levels. Vision may be lost altogether because the high pressure cuts off the blood supply to the optic nerve.

In the present model, the pupillary block is modeled by decreasing the gap between the iris and lens from 25 μ to 3 μ. For 25 μ opening of the pupil the pressure difference between the anterior and posterior chamber is order of 0.05 Pa, while when the gap size is reduced to 3 μ, the pressure of the posterior chamber is elevated to approximately 60 Pa (~0.45 mm of Hg), Fig. [7-8a & 7-9a] with respect to the anterior chamber. In some cases of pupillary block pressure difference between the two chambers rises to very high values, which could be order of 10-15 mm of Hg. This is the case when contact length between the iris and the lens increases to very high value. Iris bombe is one of the examples when iris is sealed to the lens surface near the pupil, which results in an extreme bulging of the iris. These cases are not considered here.

The present model of 3 μm gap between the iris and pupil surface is representative of a mild pupillary block, which is useful in understanding the effect of increased resistance to flow

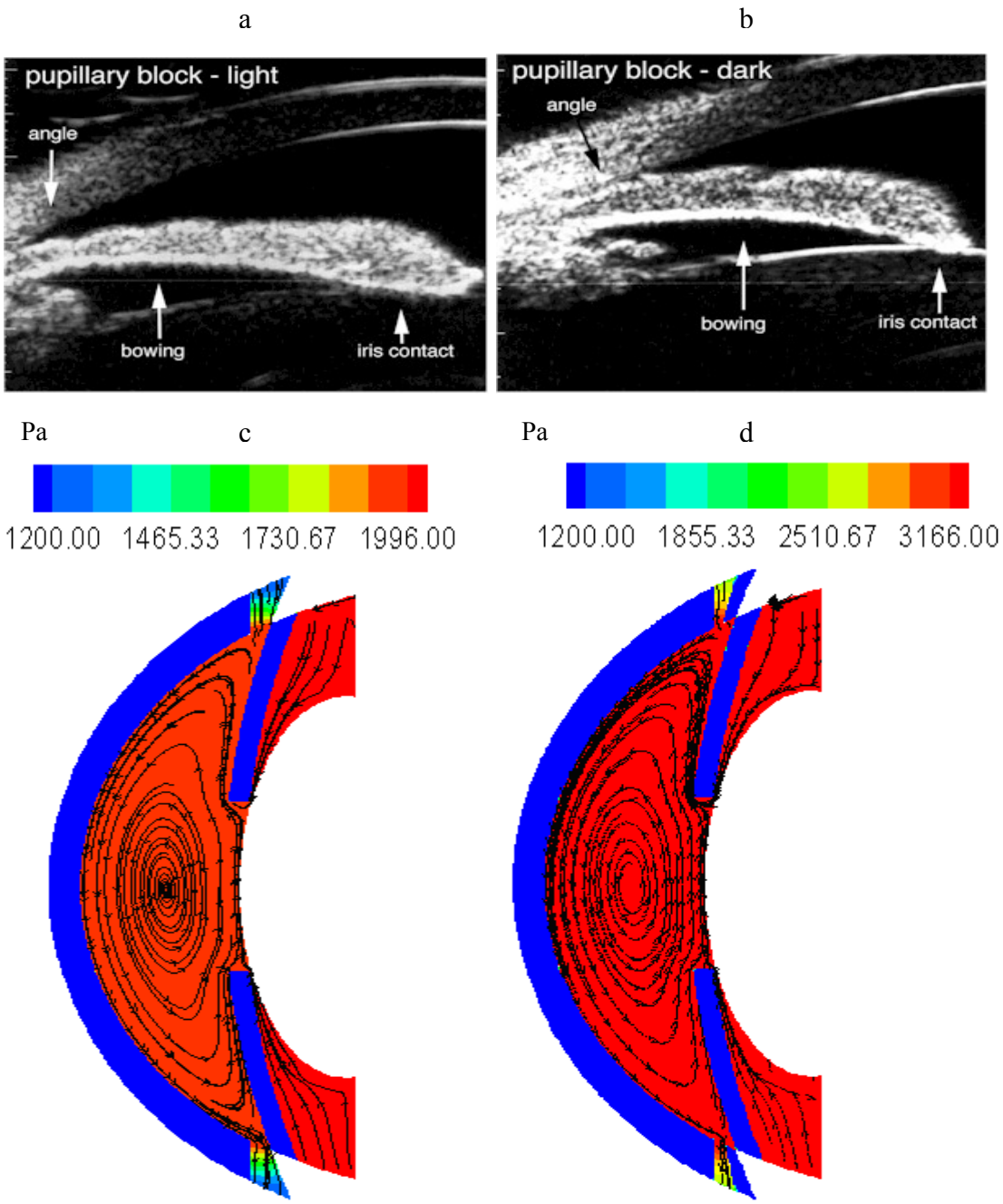

Figure 7-1: (a) Pupillary Block, Mild [54]. (b) Pupillary Block, Severe [54]. Contours of pressure and streamlines in vertical mid plane of eye, Vertical orientation. (c) Pupillary block, 3 μm iris-lens distance. (c) Angle Closure Glaucoma with lower half portion of the TM located next to anterior iris surface is closed, 3 μm iris-lens distance.

due to decrease in the iris-lens distance. In this model the iris is treated as a rigid tissue, so the bulging of iris due to pressure differential across its surfaces is not incorporated in the present

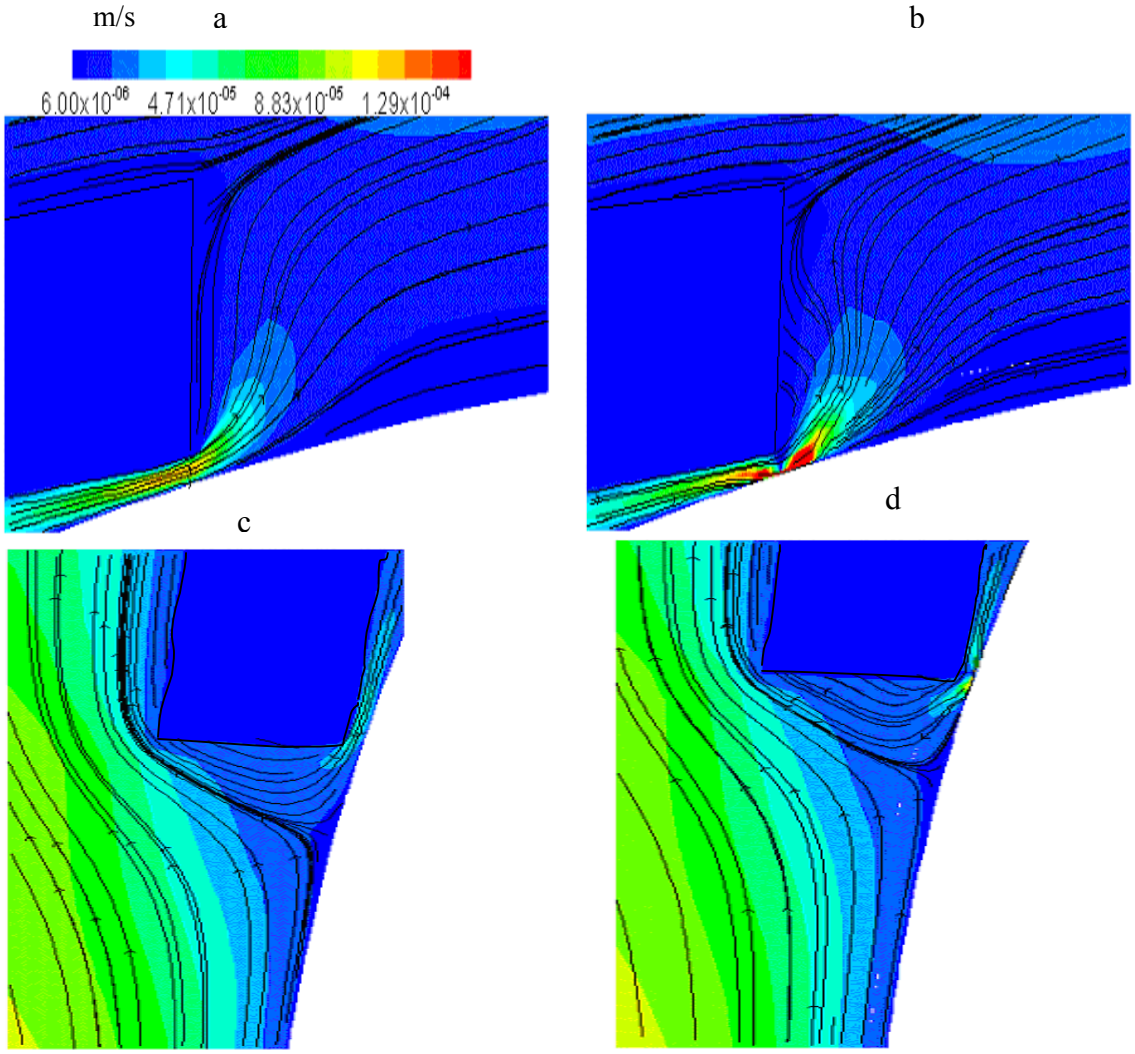

Figure 7-2: Contours and streamlines next to the irido-lenticular interface (a) 25 μm iris-lens distance, Horizontal orientation. (b) 3 μm iris-lens distance, Horizontal orientation. (c) 25 μm iris-lens distance, Upper portion of iris-tip, Vertical orientation. (d) 3 μm iris-lens distance, Upper portion of iris-tip, Vertical orientation.

simulations. The closure of anterior chamber angle and blockage of the access to the TM is modeled separately by closing the lower half portion of the TM located next to the anterior iris surface. This is an approximation to analyze the effect of anterior convexity of the iris and corresponding obstruction in outflow, which is a representation of the angle closure glaucoma. This leads to very high elevation in IOP of the anterior chamber from 1940 Pa (14.5 mm of Hg) to 3200 Pa (24 mm of Hg), Fig. [7-1d & 7-9a]. The pressure difference between the posterior and anterior chamber remains similar to the pupillary block simulation without TM-blockage as

blocking the part of TM elevates both the posterior and anterior chamber, Fig. [7-9a].

For the horizontal orientation, the maximum value of velocity magnitude is 133 μm /s for 25 μm gap, which increases to 475 μm /s for 3 μm gap. For the vertical orientation, the maximum value of velocity magnitude increases from 325 μm /s to 475 μm /s when gap size is reduced from 25 μm to 3 μm . The sharp increase in the velocity magnitude of flow between the irido-lenticular gap is shown in Fig. [7-2a & 7-2b] for the horizontal orientation and in Fig [7-2c &7-2d] for the vertical orientation. These maximum values of velocity magnitude are not affected by closing the part of TM, since the pressure difference across the iris is not separately changed by the TM blockage. The streamlines bend towards the annular surface of the iris-tip in pupillary block simulation for both the horizontal and vertical orientation due to obstruction of flow near the iris tip, Fig [7-2a-d]. Closing the part of TM leads to change in flow pattern in the vicinity of the TM, but no significant difference is observed in the other part of the anterior chamber when compared with the pupillary block simulation, Fig. [7-1c & 7-1d].

7.2 Iridectomy

Iridectomy is a surgical operation used in the treatment of closed angle glaucoma where a small hole is created in the iris to connect the posterior chamber and anterior chamber of the eye. This allows the aqueous fluid to pass easily to the anterior chamber and the bulging iris to fall back, thus opening the angle of the anterior chamber so that drainage of fluid is again possible through the TM. Nowadays laser iridectomy is mostly used instead of surgical iridectomy to create holes in the iris. The common complications encountered with the laser surgery are iritis, posterior synechiae, hemorrhage, closure of iridectomy, lens opacity, corneal epithelial and endothelial burns, retinal burn, pupillary distortion and hypopyon [53]. The proper location of the iridectomy-site on the iris surface is very important to avoid the unwanted consequences of this operation. The present work is aimed to explore the readjustment in flow and pressure

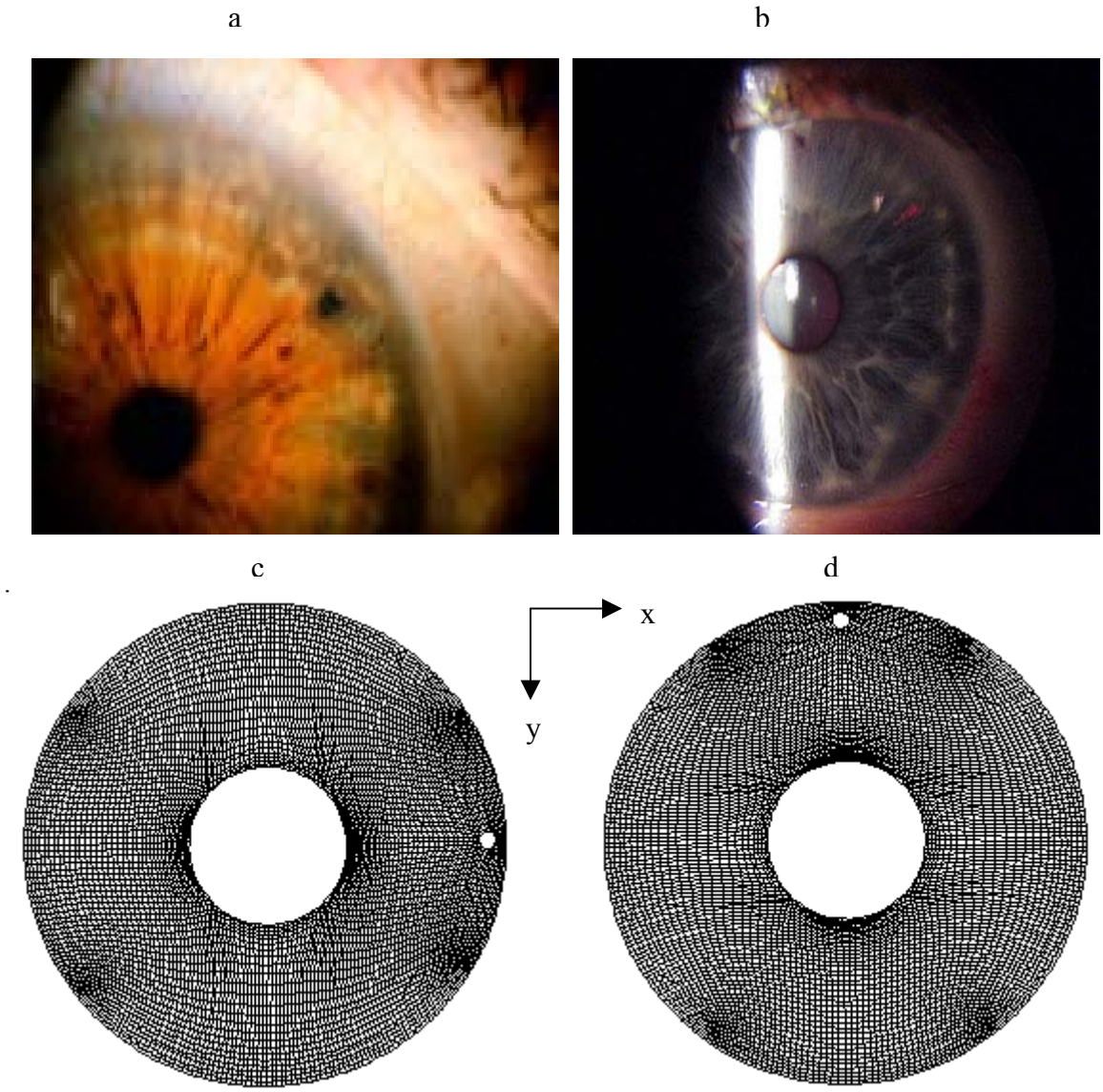

Figure 7-3: (a) Peripheral Iridectomy near 3 o'clock [55] (b) Peripheral iridectomy at 12 o'clock [56] (c) Grid on the iris surface for 3 o'clock iridectomy (d) Grid on the iris surface for 12 o'clock iridectomy.

distribution after iridectomy, this is difficult to visualize with the present medical-experimental tools. The focus of the work is to predict the optimal location of holes for the iridectomy based on the analysis of the pressure distribution, the symmetric flow profile and nature of the proper nutrition of ocular tissues.

7.2.1 Peripheral Iridectomy in Vertical Orientation

In peripheral iridectomy the hole is created at the root of the iris surface. A peripheral location is desirable for several reasons: (1) To avoid the impairment of the central vision in case of corneal or lenticular opacity. (2) The possibilty of the laser beam being directed towards the posterior pole is less; this is desirable to protect the retinal surface. (3) There is greater separation between the posterior iris surface and anterior lens capsule in the area peripheral to the anterior lens curvature [53]; this will protect the lens. The disadvantage is the possibility of the corneal burn near the iris-root by the iridectomy procedure [53] due to overheating by the laser beam.

The iridectomy is generally performed between the 9 and 11 o'clock position or between the 1 and 3 o'clock position [53], Fig [7-3a]. This is an especially convenient region to treat because it is easily viewed from the bio-microscope through a contact lens and laser beam can be directed away from the posterior pole. In some cases of iridectomy the hole is created at 12 o'clock position, Fig [7-3b]. In the present model for comparing the effect of peripheral iridectomy at different locations, holes are created at 12, 6 and 9 o'clock position, Fig [7-3c & 7-3d].

Fig. [7-4] shows the streamlines and velocity magnitude contours for the various cases considered. After the creation of hole on the iris surface most of the flow enters into the anterior chamber through the hole and there is negligible flow through the pupil. For 12 o'clock iridectomy, flow entering the anterior chamber through the hole passes along the surface of the TM next to the anterior chamber and then it descends along the corneal surface, Fig [7-4b, 7-5b]. Plot of velocity magnitude along a line parallel to Y-axis (Z=4.6 mm, X=0mm) located inside the anterior chamber near the iris periphery shows that the magnitude of velocity is high (50 %) just next to the drilled hole near the upper TM in comparison to the pupillary block simulation, Fig. [7-7a]. For the pupillary block the highest magnitude of velocity (475 μm /s) is observed in the pupillary gap, while after the iridectomy the highest velocity (454 μm /s) is observed in the iris

hole. Any significant velocity differences are not observed in the mid or bottom portion of the anterior chamber. The high velocity in the vicinity of upper TM and upper corneal surface suggests that the iris pigments and debris produced after the iridectomy will not get deposited at those locations. The stronger flow along the corneal surface could be better for the nutrition of the corneal endothelium.

When the iridectomy site is located at 6 o'clock position, strong flow is observed along the surfaces of lower TM and lower portion of the iris, Fig. [7-4c & 7-5d]. On the lower portion of the cornea, the flow is directed upwards, which is opposite in direction compared to the pupillary block simulation, Fig. [7-4a & 7-4c]. This flow pattern is likely to hinder the deposition of particles present in AH at these locations, which have general tendency to gravitate at bottom of the anterior chamber under normal condition. The plot of the velocity magnitude along a line parallel to Y-axis (Z=4.6 mm, X=0mm) located inside the anterior chamber near to the iris periphery show that the magnitude of velocity is slightly less along this line in the vicinity of the lower portion of cornea in comparison to the pupillary block simulation, Fig. [7-7a]. This is consequence of the strong flow coming from the hole which compel the flow descending along the corneal surface to take sharp bend towards the iris surface at a higher location on the corneal surface compared to the location of sharp bend in pupillary block simulation, Fig. [7-4a & 7-4c]. No significant difference in flow is observed in the upper and mid portions of the anterior chamber.

For the iridectomy site at 9 o'clock position, flow enters the anterior chamber through the hole in the mid horizontal plane of the anterior chamber and rises against the gravity in the vertical planes passing through the hole, Fig. [7-4d & 7-5d]. The flow circulates in this vertical mid plane and finally moves towards the center of the anterior chamber, Fig. [7-4e & 7-5e]. No significant difference in the flow pattern and in the velocity magnitude is observed in the vertical mid plane passing through central axis, Fig. [7-4d] when compared with the pupillary block simulation, Fig [7-4a & 7-7a].

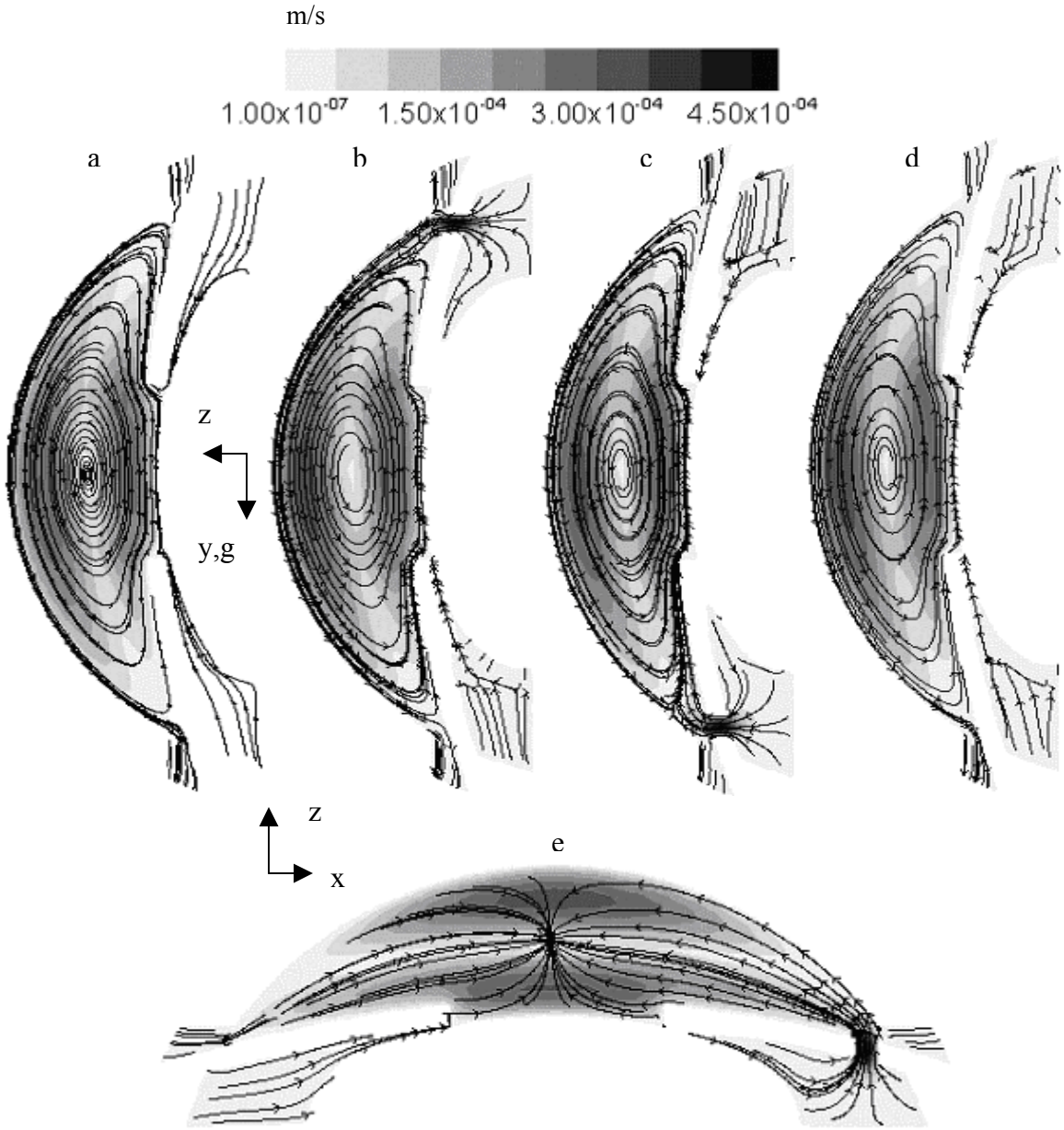

Figure 7-4: Comparison of streamlines and contours of velocity magnitude in vertical mid plane for the case of iridectomy when hole is located next to the iris root. (a) Pupillary block (b) Hole located at 12 o' clock position (c) Hole located at 6 o' clock position (d) Hole located at 9 o' clock position (e) Horizontal plane, Hole located at 9 o' clock position.

Fig. [7-6] shows the velocity contours and streamlines in the horizontal plane passing through the hole for 12 o'clock and 6 o'clock iridectomy and in vertical plane for 9 o'clock iridectomy. For 12 o'clock and 6 o'clock iridectomy a portion of the flow coming from the hole moves towards the corneal surface in the horizontal plane after entering into the anterior chamber,

Fig. [7-6a]. For the 6 o'clock iridectomy, however the major part of the flow rises upward along the iris surface in the vertical plane For the 9 o'clock iridectomy, the flow entering the anterior chamber through the hole moves along the iris surface against the gravity direction (Y-axis) towards the upper portion of the anterior chamber and finally comes out through the pores of TM, Fig. [7-6c]. This destroys the symmetry in the flow.

There is no change in the velocity magnitude along a line parallel to X-axis (Y=0mm, Z=4.6mm) located inside the anterior chamber close to the anterior iris surface for any position of iridectomy, Fig. [7-7b]. This shows that creating hole close to the iris root does not produce any change in the flow profile inside the anterior chamber in the horizontal plane. There is sharp change in the flow in the vicinity of hole-location for all positions of iridectomy, Fig. [7-7b], but any significant change is not observed in the rest part of the anterior chamber. When velocity magnitude is plotted along a line parallel to Z-axis (X=0mm, Y=-2.5mm), it is observed that for pupillary block simulation the flow passes into the anterior chamber through the pupillary gap, which is reflected by high velocity magnitude (40 $\mu m / s$) along the part of the line (Z=3.8 mm to 4.2 mm, Fig. [7-7c]) located in the posterior chamber. For all positions of iridectomy, there is negligible flow through the pupillary gap (Z=3.8 mm to 4.2 mm, Fig. [7-7c]) as most of flow rushes towards the location of the hole on the iris surface. No difference is observed in velocity magnitude along the portion of this line located inside the anterior chamber (Z=4.4 mm to 7.0 mm, Fig. [7-7c]) for all positions of the iridectomy.

For the 12 and 6 o'clock iridectomy flow pattern are symmetrical across the vertical mid plane, while 9 o'clock iridectomy produces asymmetry across the vertical mid plane, Fig. [7-4 d & 7-5e]. The asymmetric flow profile for the single-hole iridectomy at 9 o'clock can introduce asymmetry in nutrition of the ocular tissues, which can lead to some significant ocular changes in long run. The 6 o'clock iridectomy is generally not preferred to avoid the other complicacies

associated with the laser iridectomy. So most preferred iridectomy could be in the vicinity of 12 o'clock as far as flow distribution and maintenance of symmetry is concerned.

To compare the pressure distribution between the baseline configurations with pupillary block and the iridectomy simulations, the pressure contours are plotted in a vertical mid plane for

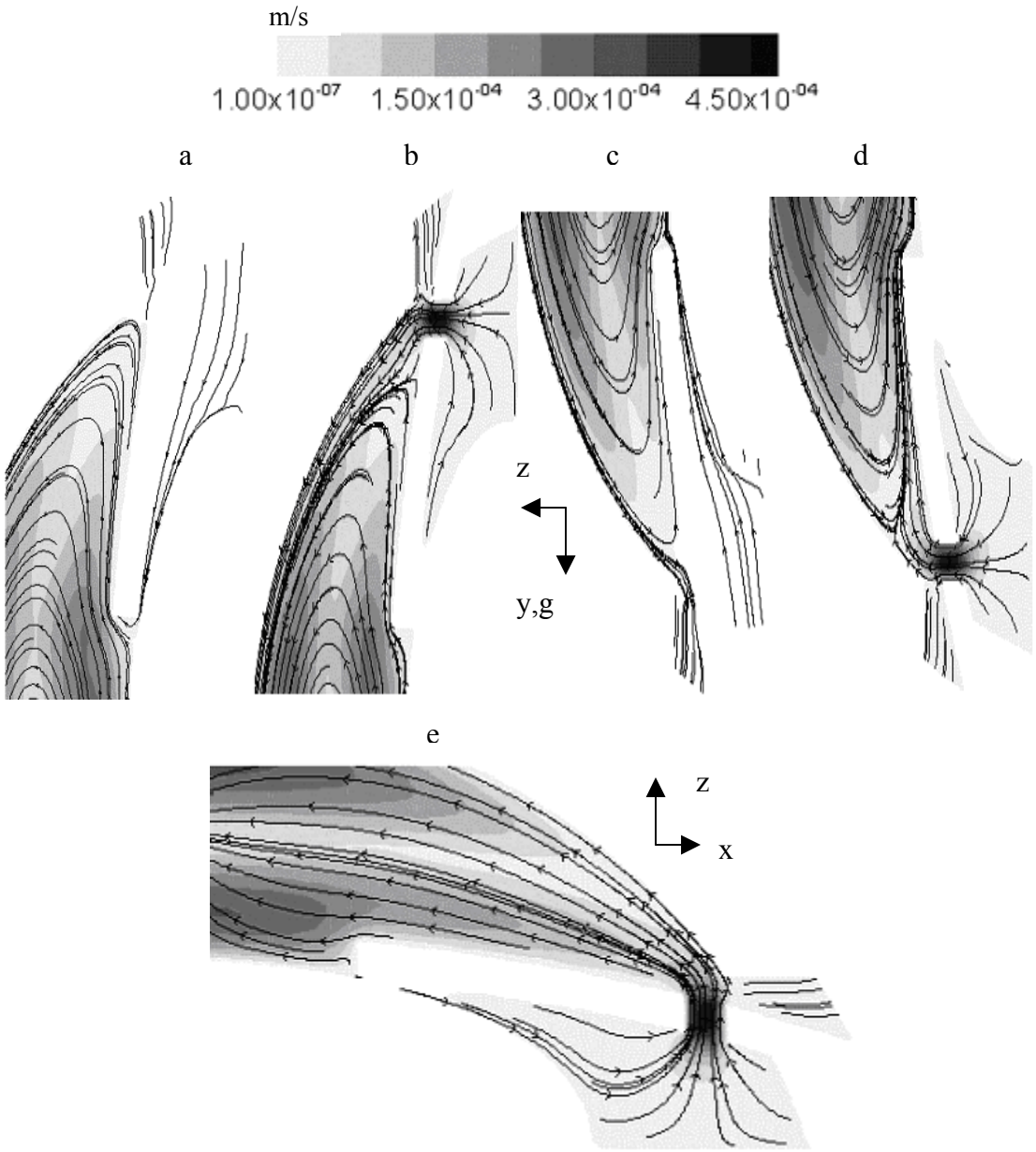

Figure 7-5: Extended view of streamlines and contours of velocity magnitude in vertical mid plane for the case of iridectomy when hole is located next to the iris root. (a) Pupillary block (b) Hole located at 12 o' clock position (c) Hole located at 6 o' clock position (d) Hole located at 9 o' clock position. (e) Horizontal plane, Hole located at 9 o' clock position.

pupillary block, Fig. [7-8a], and configurations corresponding to 12 o'clock iridectomy, Fig [7-8b], 6 o'clock iridectomy, Fig [7-8c], 9 o'clock iridectomy [7-8d] and in horizontal mid plane for 9 o'clock iridectomy, Fig [7-8e]. As the pressure ranges are different in pupillary block and

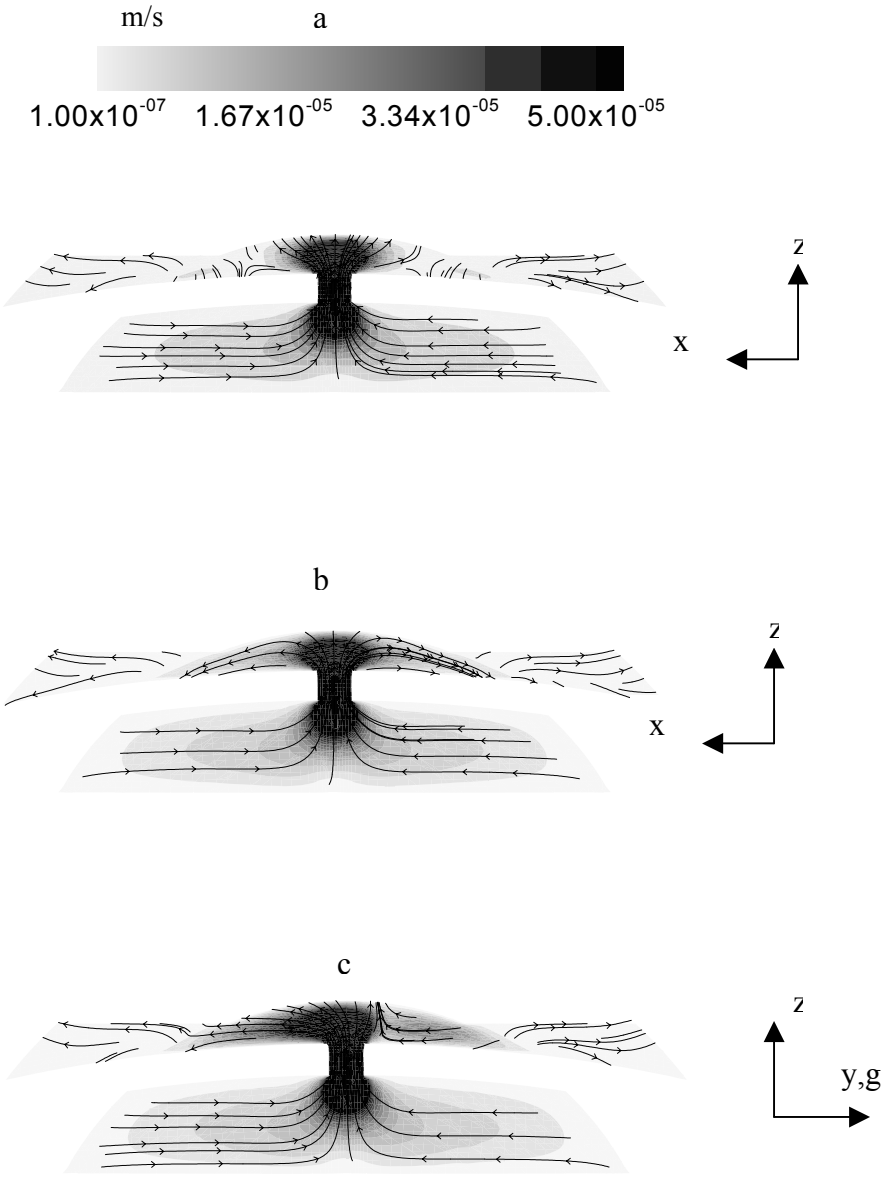

Figure 7-6: Streamlines and contours of velocity magnitude in vertical plane passing through the hole for the case of iridectomy when hole is located next to the iris root, Vertical Orientation. (a) Hole located at 12 o' clock position (b) Hole located at 6 o' clock position (c) Hole located at 9 o' clock position.

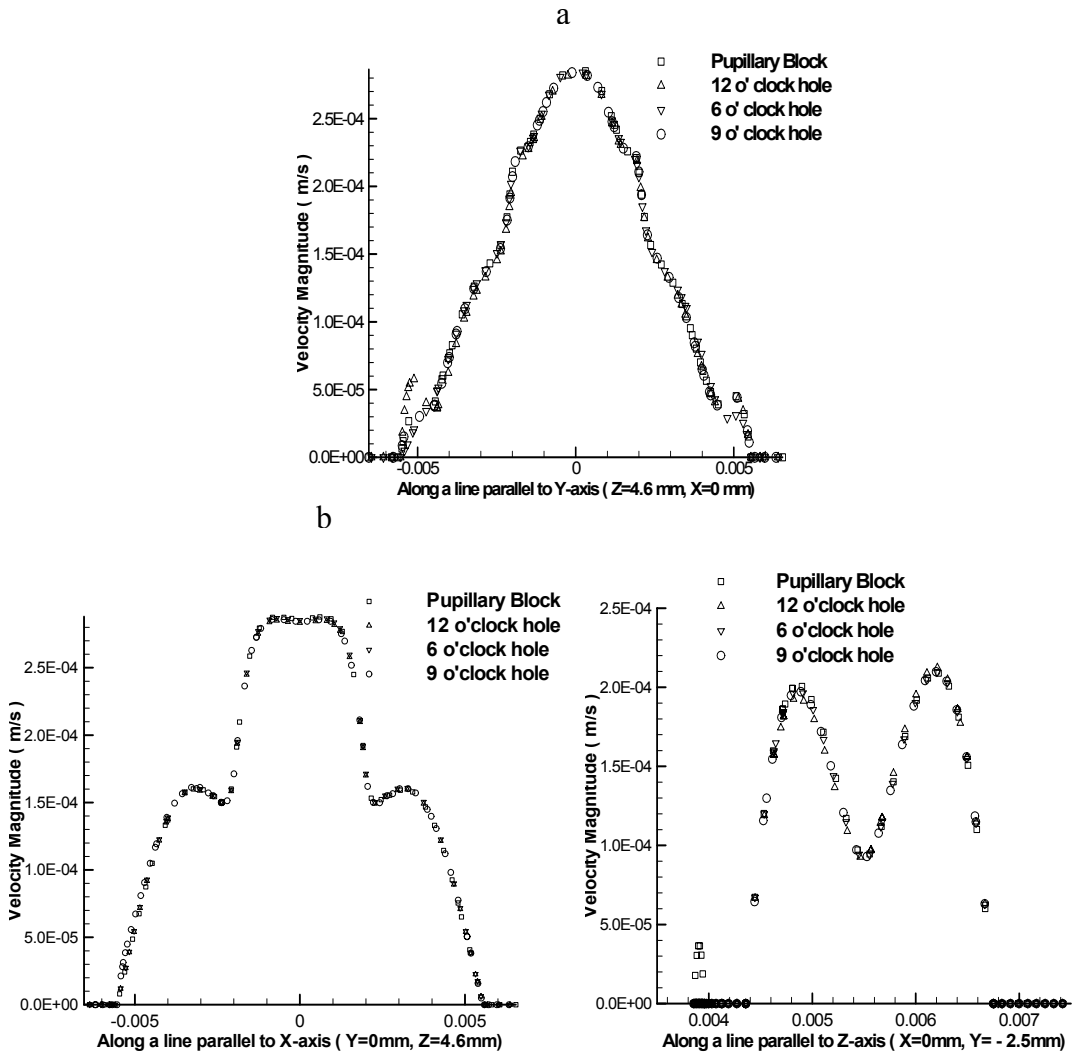

Figure 7-7: Iridectomy with hole located at iris-root, Vertical Orientation. Comparison of velocity magnitude among pupillary block and iridectomy with different locations of holes (a) Along a line parallel to Y-axis (Z=4.6 mm, X=0mm) inside the anterior chamber near the iris periphery. (b) Along a line parallel to X-axis (Y=0mm, Z=4.6mm) inside the anterior chamber near to the iris periphery. (b) Along a line parallel to Z-axis (X=0 mm, Y= -2.5mm).

iridectomy simulations, different scales are used for plots to show the difference of pressure distribution between the posterior chamber and anterior chamber. For the pupillary block the pressure difference between the posterior and anterior chamber is around 60 Pa, Fig [7-8a], which diminishes to 0.05 Pa for all cases of iridectomy, Fig [7-8b-e]. The creation of holes in the iris facilitates the direct passage of flow from the posterior chamber to anterior chamber. So after iridectomy there is no obstruction of flow into the anterior chamber; this leads to a decrease in pressure in the posterior chamber. The pressure (~1940 Pa) in the anterior chamber is same for

pupillary block and iridectomy simulations, Fig. [7-9b]. So iridectomy simulations do not bring any change in the anterior chamber pressure. The effect of pressure differential across the iris is the anterior bulging of iris, which is not modeled in the present simulations. So the pressure elevation in posterior chamber does not bring any significant change in the anterior chamber pressure distribution. Consequently, iridectomy does not cause any significant change in the pressure distribution of anterior chamber. The pressure contours in the vertical mid plane for iridectomy at different locations do not show much difference from each other except at specific location of the holes, Fig. [7-8b-e].

The contours of velocity magnitude and streamlines in a vertical plane parallel to the equatorial plane and located inside the posterior chamber (Z=2.6 mm) show that symmetry in the flow pattern of posterior chamber is completely destroyed by the creation of holes. For the pupillary block simulation, streamlines in the above plane indicate that after secretion from the ciliary body AH moves toward the pupillary gap between the iris and lens from the entire cilary-body surface of the posterior chamber, Fig. [7-10a]. For all iridectomy simulations, AH rushes towards the holes in the iris surface, Fig. [7-10b-d]. As the flow moves towards the location of hole, the magnitude of velocity increases gradually and in the vicinity of hole it increases to very high value. In pupillary block simulation the flow passages through the pupillary gap into the anterior chamber, while with the opening of the holes there is negligible flow from the pupillary gap, which is reflected by the tangential streamlines in the vicinity of the lens, Fig. [7-10b-d].

The velocity magnitude is plotted along a line parallel to Y-axis, Fig. [7-11a], and along a line parallel to X-axis, Fig. [7-11b], located on a vertical plane (parallel to the equatorial plane) inside the posterior chamber (Z=2.6 mm) to analyze the flow profile in the posterior chamber after creation of holes. Here the Y-axis is the location of 12 and 9 o'clock holes, and the X-axis is the location of 9 o'clock and 3 o'clock holes. For pupillary block simulation the flow is

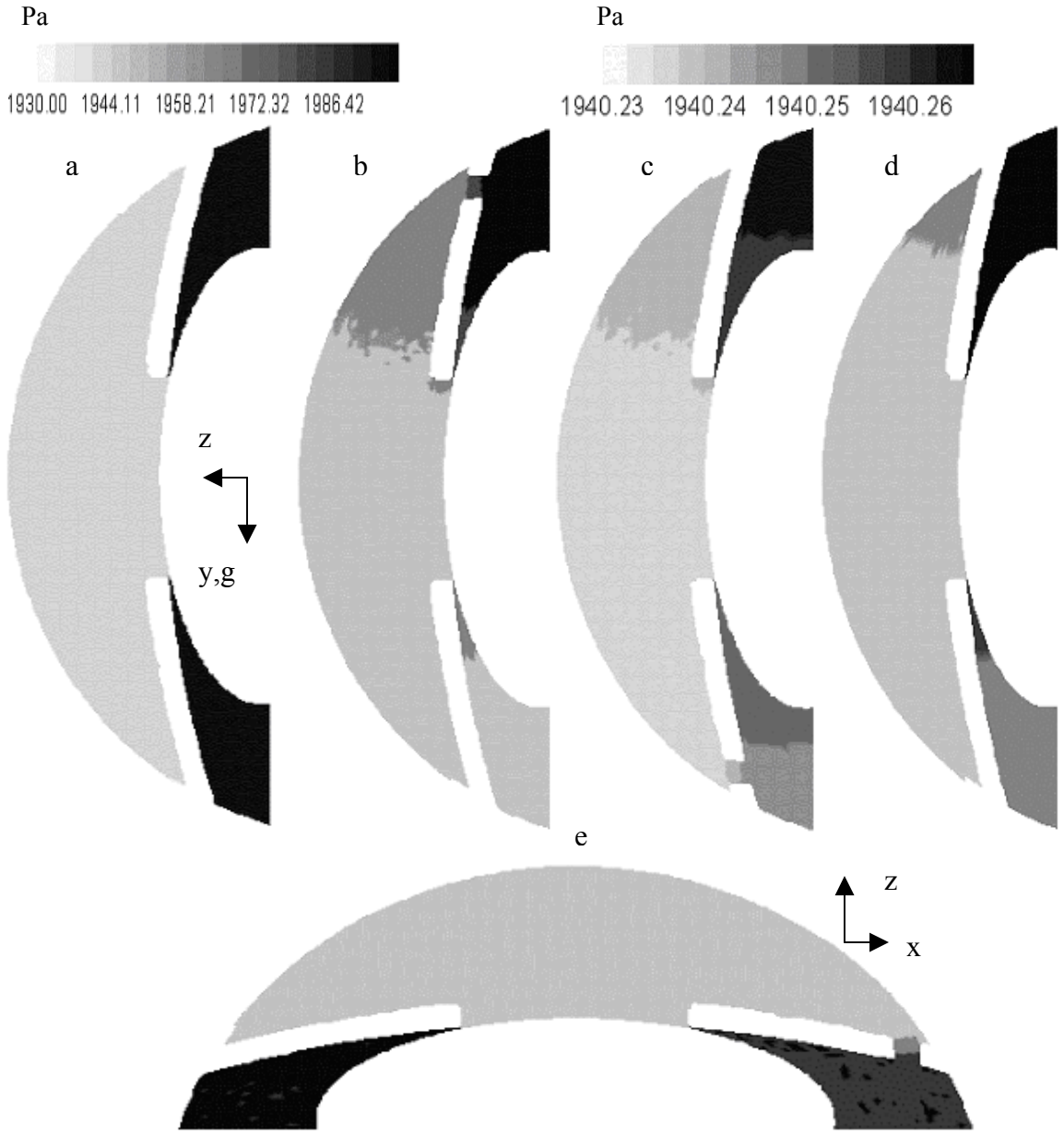

Figure 7-8: Comparison of pressure contours in vertical mid plane for the case of iridectomy when hole is located next to the iris root. (a) Pupillary block (b) Hole located at 12 o' clock position (c) Hole located at 6 o' clock position (d) Hole located at 9 o' clock position. (e) Horizontal plane, Hole located at 9 o' clock position.

symmetrical in this vertical plane and maximum velocity magnitude (1.2 $\mu m / s$) is observed at a radial distance of 6 mm from the center of this vertical plane. In this vertical plane for 12 o'clockiridectomy, the velocity magnitude increases to 26 $\mu m / s$, Fig. [7-11a], in the vicinity of

the 12 o'clock hole, which is 22 times greater than the pupillary block simulation. In this plane at the

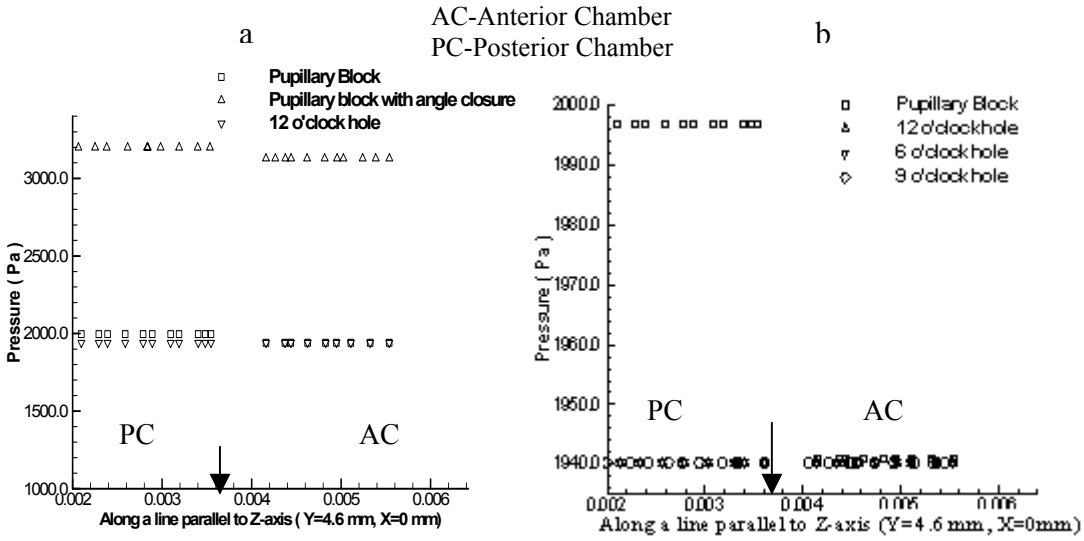

Figure 7-9: Iridectomy with hole located at iris-root, Vertical Orientation (a) Comparison of pressure magnitude among pupillary block, angle closure with pupillary block and 12 o'clock iridectomy along a line parallel to Z-axis (Y=4.6 mm, X=0mm). (c) Comparison of pressure magnitude among pupillary block and various location of holes along a line parallel to Z-axis (Y=4.6 mm, X=0mm).

location close to 6 o'clock the velocity magnitude (1 $\mu m/s$) is even less than the pupillary block (1.2 $\mu m/s$) simulation as the flow is moving away from this location towards the 12 o'clock location, Fig. [7-11a]. At the location of 9 o'clock and 3 o'clock position the velocity magnitude is 6 $\mu m/s$, Fig. [7-11b], which is 5 times greater than the velocity magnitude at the corresponding location in pupillary block simulation. The AH rushes from the bottom of the posterior chamber to the upper portion of the posterior chamber passing through the 9 o'clock and 3 o'clock locations, which leads to high velocity at 9 o'clock and 3 o'clock locations.

For 6 o'clock iridectomy, the flow profile in the vicinity of the 6 o'clock hole resembles with the flow profile at 12 o'clock hole for 12 o'clock iridectomy. The velocity magnitude increases by 22 times (26 $\mu m/s$) in the vicinity of the 6 o'clock hole, Fig. [7-11a], in comparison with the pupillary block simulation. Very low velocity magnitude is observed at 12 o'clock hole

(1 $\mu m/s$), Fig. [7-11a], as flow is moving away from this region to the location of hole. The velocity magnitude at 9 o'clock and 3 o'clock (6 $\mu m/s$) is greater than the pupillary block simulation (1.2 $\mu m/s$) as the flow is moving towards the 6 o'clock hole position (lower portion of posterior chamber) from the upper portion of the posterior chamber.

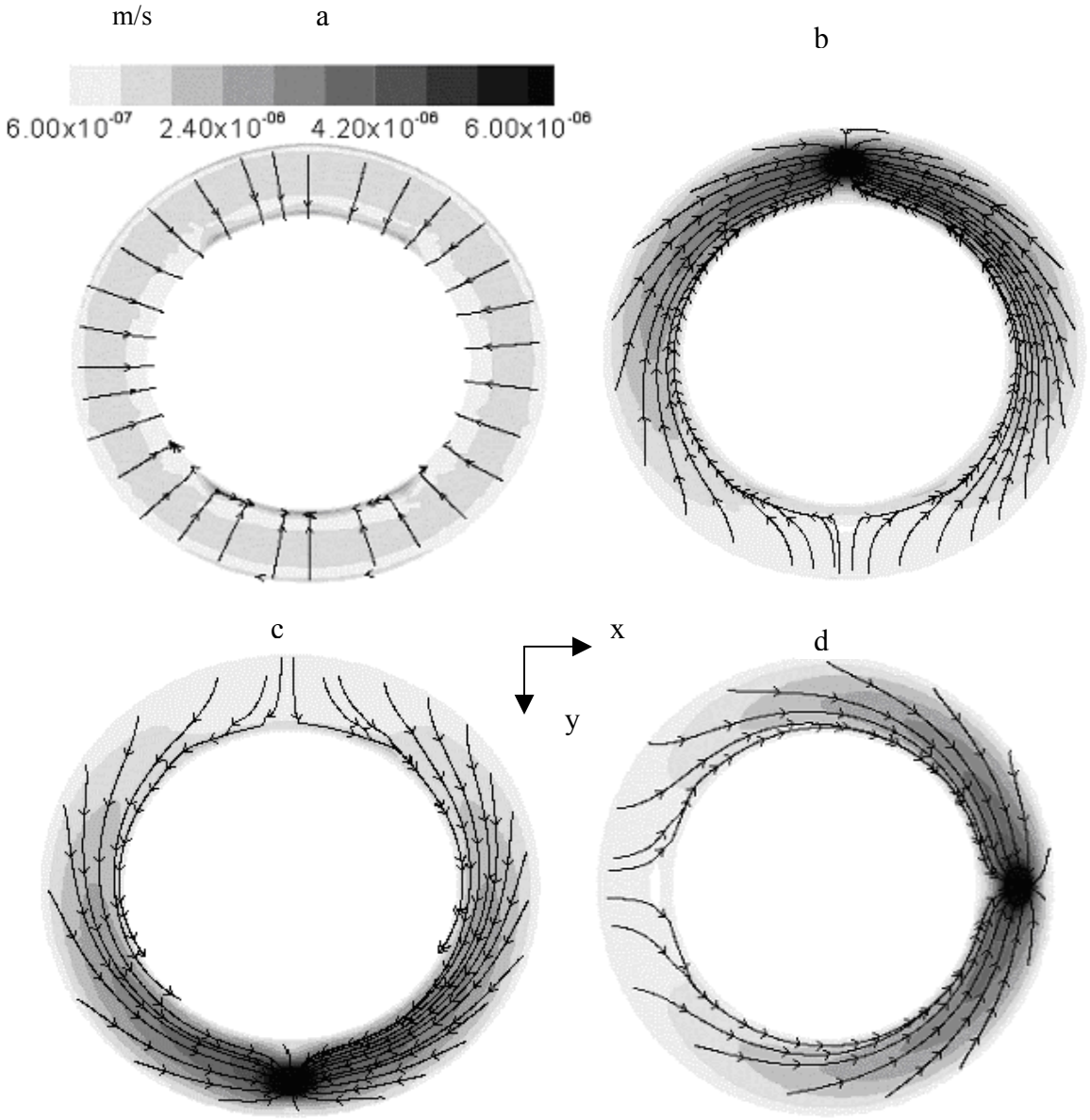

Figure 7-10: Comparison of streamlines and contours of velocity magnitude in plane parallel to equatorial plane (z = 2.6 mm, located in the posterior chamber) for the case of iridectomy when hole is located next to the iris root. (a) Pupillary block (b) Hole located at 12 o' clock position (c) Hole located at 6 o' clock position (d) Hole located at 9 o' clock position.

Like 12 o'clock and 6 o'clock iridectomy, the flow rushes towards the location of hole in 9 o'clock iridectomy. So very high velocity (26 $\mu m/s$) is observed close to the 9 o'clock hole (in vertical plane passing through posterior chamber), Fig. [7-11b], while at 3 o'clock hole the velocity magnitude is lower, Fig. [7-11b], than the velocity magnitude in pupillary block

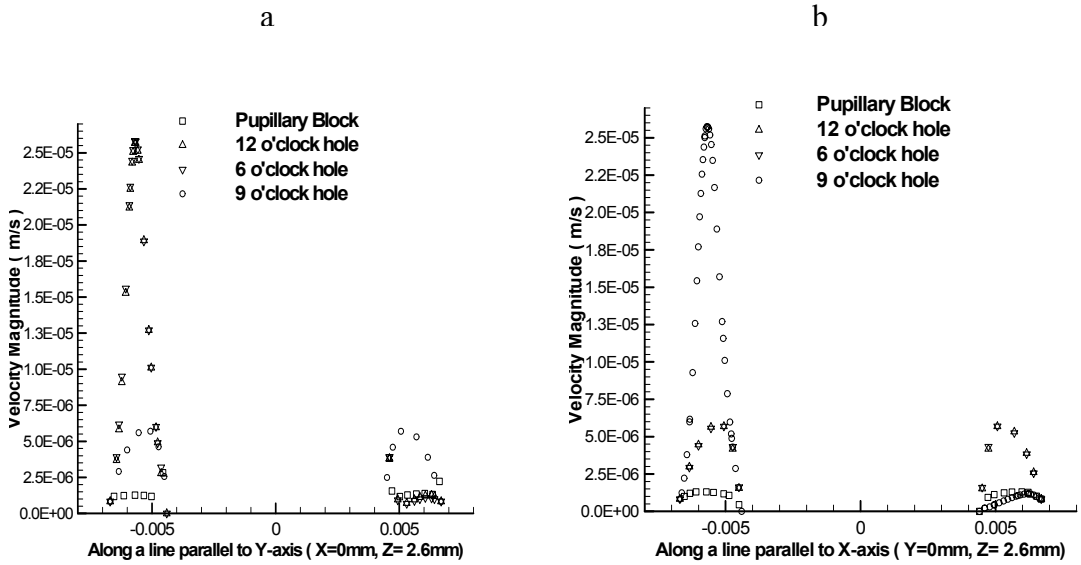

Figure 7-11: Iridectomy with hole located at the iris-root, Vertical Orientation, Comparison of velocity magnitude among pupillary block and various location of holes (a) Along a line parallel to Y-axis (X=0mm, Z=2.6mm) located inside the posterior chamber. (b) Along a line parallel to X-axis (Y=0mm, Z=2.6mm) located inside the posterior chamber.

simulation at the corresponding location. At 12 o'clock and 6 o'clock location greater velocity (6 $\mu m/s$) is observed compared to the pupillary block simulation, Fig. [7-11a].

So, in the vertical cross-section of the posterior chamber (Z=2.6mm) the velocity magnitude increases to 26 $\mu m/s$ at the location on the vertical plane close to the hole for all cases of iridectomy, while on the location just opposite to the hole the velocity magnitude decreases to 1 $\mu m/s$. On the axis perpendicular to the axis of hole-location, the velocity magnitude increases by 5 times to 6 $\mu m/s$ when compared with the corresponding location in pupillary block simulation. Asymmetry is introduced in the posterior chamber flow profile for all locations of the hole. The goal is to find out the location and arrangement of holes to minimize

the asymmetry in flow pattern.

7.2.2 Iridectomy at Central Location in Vertical Orientation

The most preferred site for the iridectomy is the peripheral location, but in some cases when corneal endothelium burns is probable, the iridectomy site is shifted to the more central locations. This happens particularly in eyes with extremely shallow anterior chambers or eyes having brown iris [53]. There are some major disadvantages of the central location- (a) There is possibility of lenticular damage due to the thermal conduction to underlying lens. (b) If laser is misdirected, retinal burns could occur. Like the peripheral iridectomy, iridectomy at central location is generally performed between 9 and 11 o'clock position or between 1 and 3 o'clock position, but in some cases it could be performed between 11 and 1 o'clock position. In the present model for comparing the effect of different iridectomy sites, holes are created at 12, 6 and 9 o'clock position. The holes are located from the iris root at a distance, which is two-thirds of the distance between the pupil edge and the iris root. The center of the hole is located at 4 mm distance from the central axis (Z-axis) and the diameter of the hole is taken as 0.5 mm for all the simulations.

Like the peripheral iridectomy, most of the flow enters into the anterior chamber through the hole in the iris and there is negligible flow through the pupil. For 12 o'clock iridectomy, the flow entering the anterior chamber through the right side of the hole rises along the iris surface up to the TM and then descends along the corneal surface. The major part of the flow coming through the hole moves directly towards the corneal surface and then descends along the corneal surface, Fig. [7-12b & 7-13b]. Plot of velocity magnitude along a line parallel to Y-axis (Z=4.6 mm, X=0mm) and located inside the anterior chamber near to the iris periphery show that the magnitude of velocity is high (40 %)in the vicinity of the hole opening in comparison to the pupillary block simulation, Fig. [7-15a]. For the pupillary block the highest magnitude of velocity (475 μm /s) is observed in the pupillary gap, while after the iridectomy the highest velocity (452

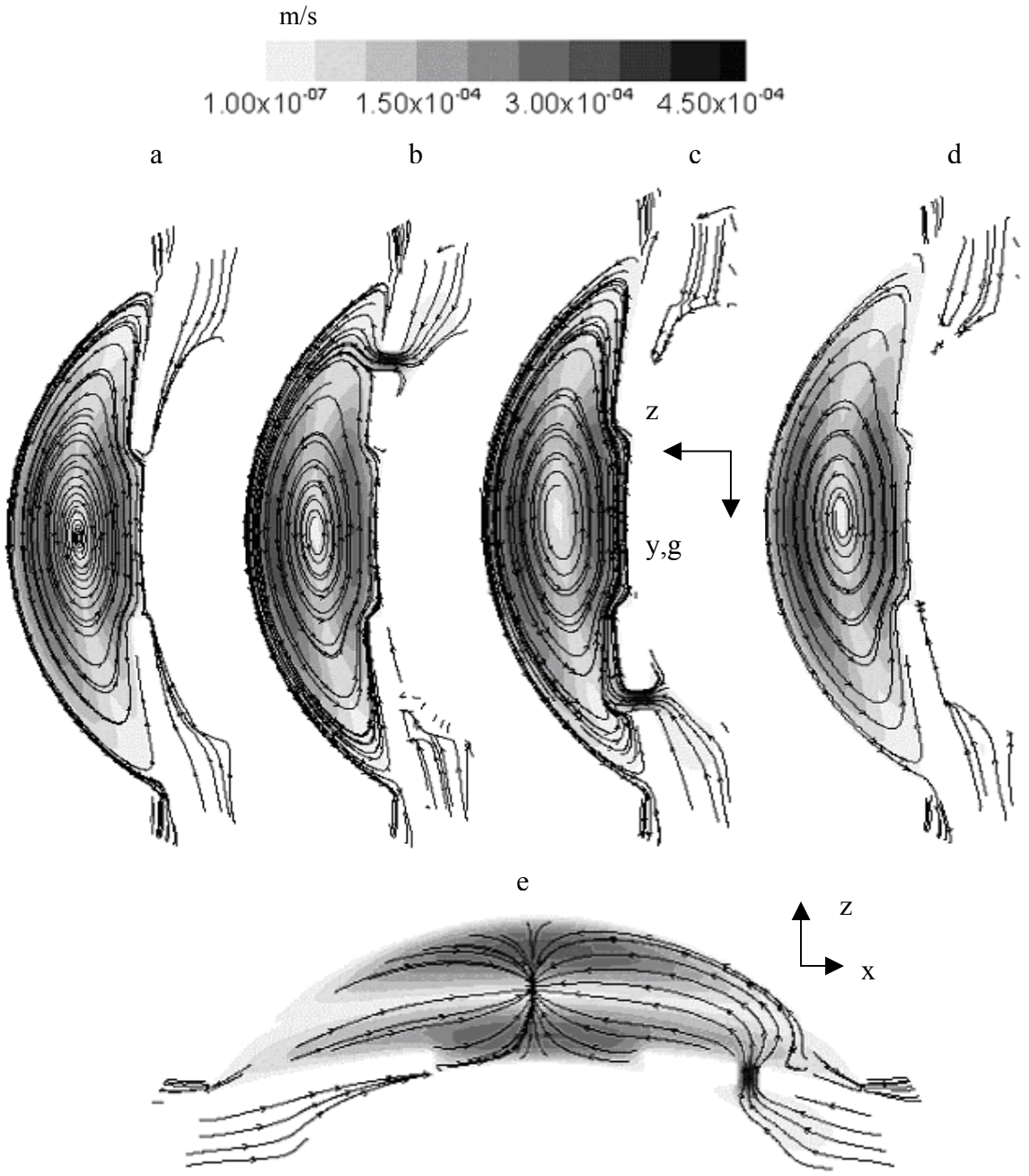

Figure 7-12: Comparison of streamlines and contours of velocity magnitude in vertical mid plane for the case of iridectomy when hole is located at two-thirds of distance between the pupil border and iris periphery. (a) Pupillary block (b) Hole located at 12 o' clock position (c) Hole located at 6 o' clock position (d) Hole located at 9 o' clock position. (e) Horizontal plane, Hole located at 9 o' clock position.

μm /s) is observed in the hole. Any significant difference is not observed on the mid or bottom portion of the anterior chamber. As most of the flow takes a sharp bend towards the corneal

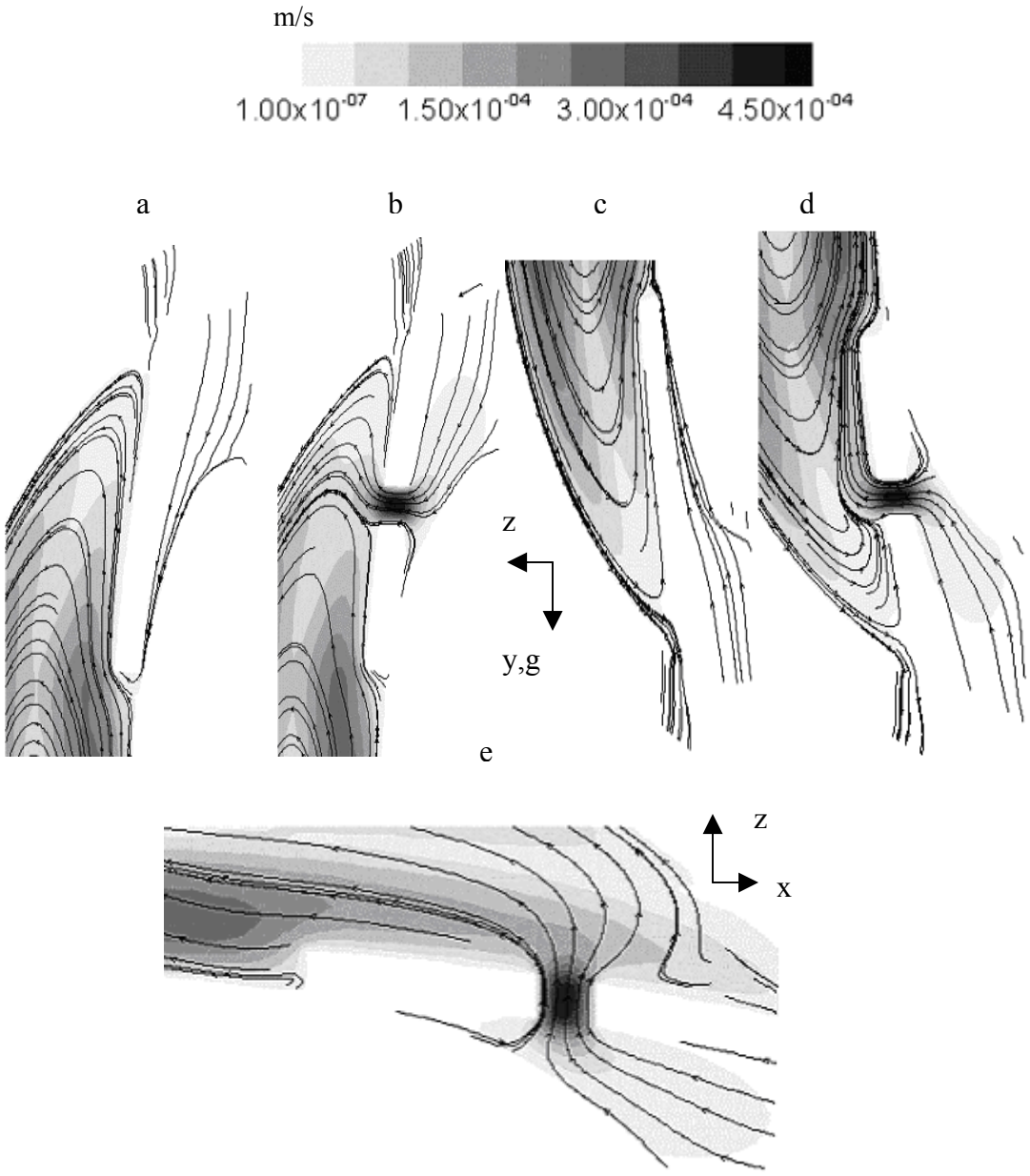

Figure 7-13: Extended view of streamlines and contours of velocity magnitude in vertical mid plane for the case of iridectomy when hole is located at two-thirds of distance between the pupil border and iris periphery. (a) Pupillary block (b) Hole located at 12 o' clock position (c) Hole located at 6 o' clock position (d) Hole located at 9 o' clock position. (e) Horizontal plane, Hole located at 9 o' clock position.

surface at the location of hole, flow in the vicinity of the upper TM is not strong. This could lead to particle deposition on the upper portion of TM and corneal surface. The low velocity magnitude above the hole location could be reason of mal-nutrition of the ocular tissues located in this region.

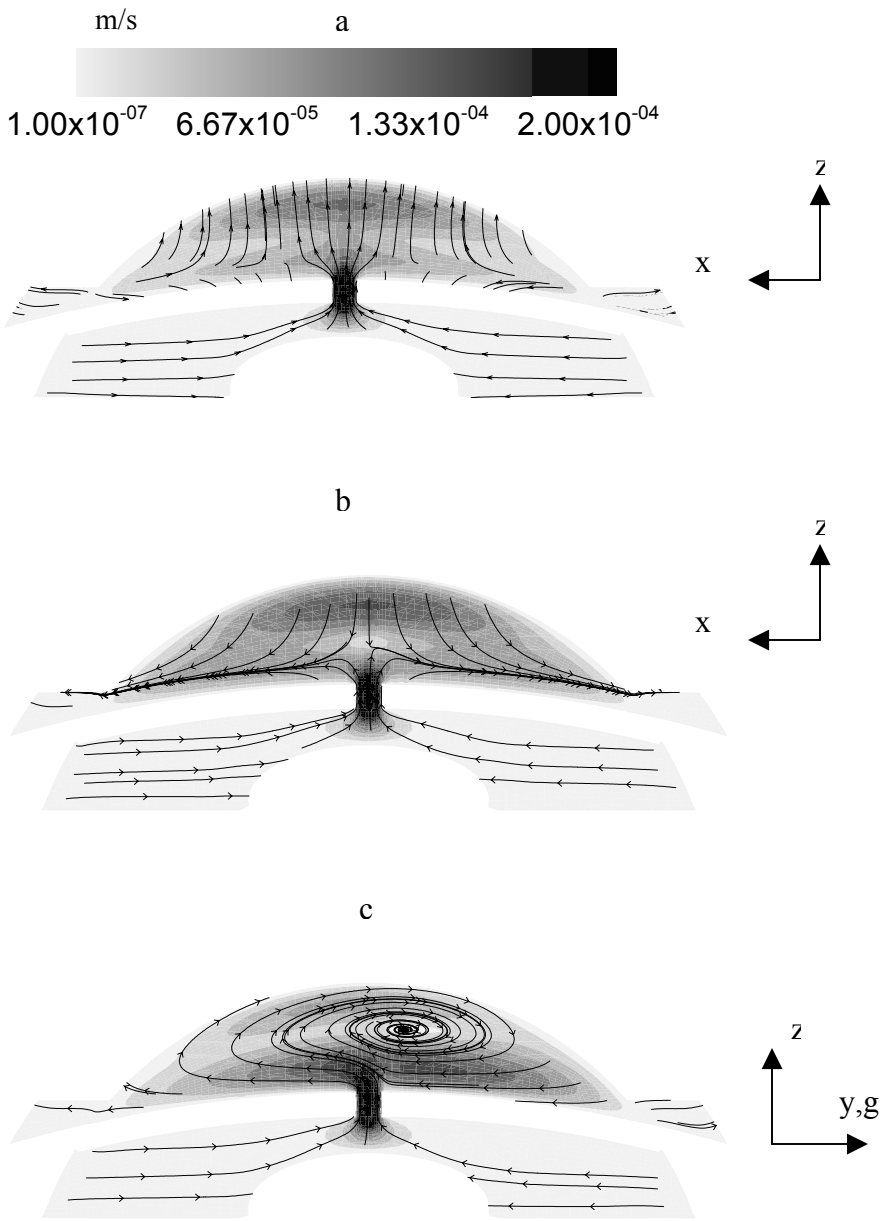

Figure 7-14: Streamlines and contours of velocity magnitude in vertical plane passing through the hole for the case of iridectomy when hole is located at two-thirds of distance between the pupil border and iris periphery, Vertical Orientation. (a) Hole located at 12 o' clock position (b) Hole located at 6 o' clock position (c) Hole located at 9 o' clock position.

inside the iris hole.

When iridectomy site is located at 6 o'clock position, even though the magnitude of flow velocity is very high inside the hole, after entering into the anterior chamber flow do not rise towards the corneal surface because of the buoyancy effects; instead of that it rises along the iris

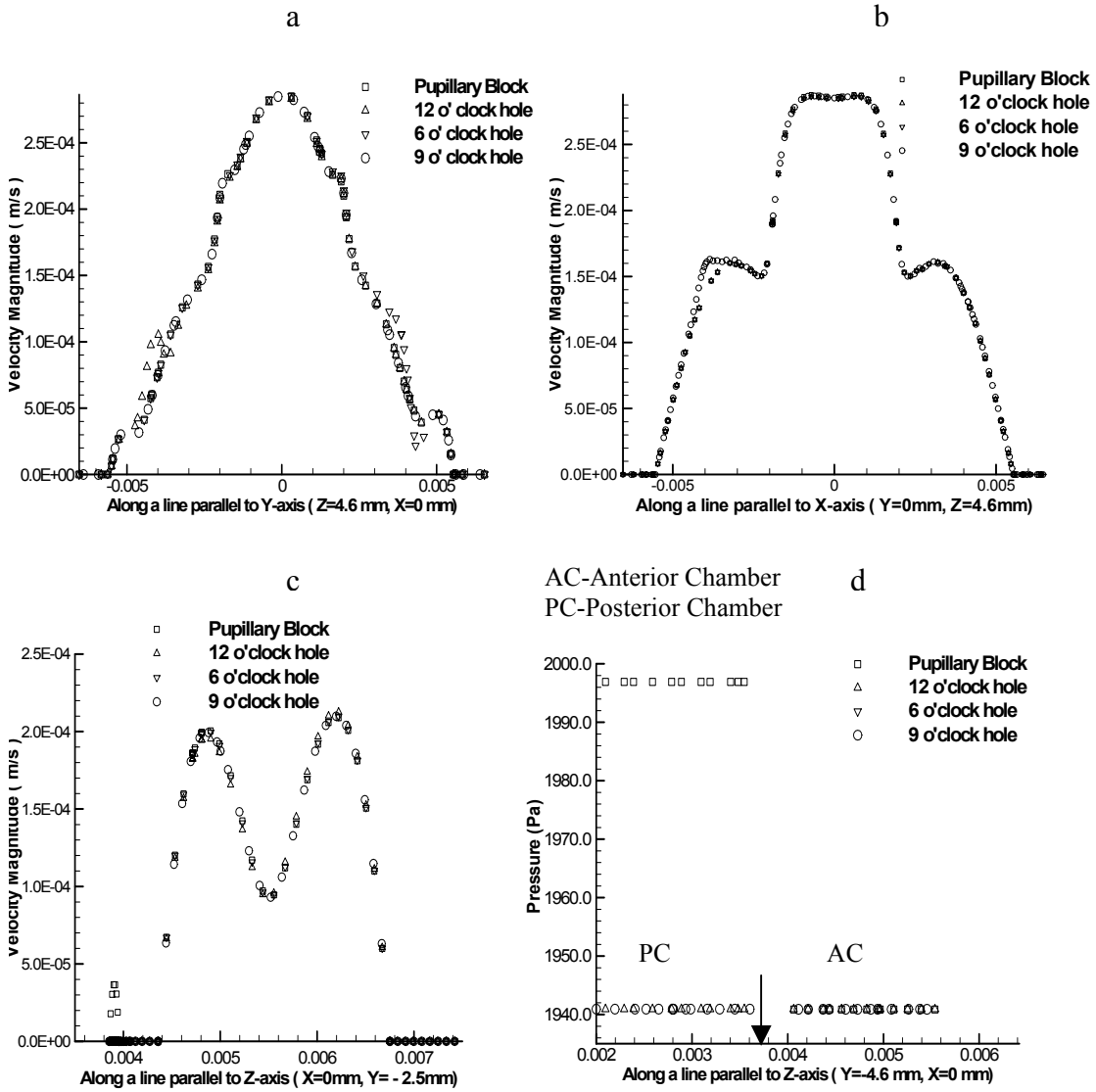

Figure 7-15: Iridectomy with hole located at two-thirds of distance between the pupil border and iris periphery, Vertical Orientation. Comparison of velocity magnitude among pupillary block and various locations of holes (a) Along a line parallel to Y-axis (Z=4.6 mm, X=0 mm) inside the anterior chamber near the iris periphery. (b) Along a line parallel to X-axis (Y=0mm, Z=4.6mm) inside the anterior chamber near the iris periphery. (b) Along a line parallel to Z-axis (X=0 mm, Y= -2.5mm.) (d) Comparison of pressure magnitude among pupillary block and various location of holes along a line parallel to Z-axis (Y=-4.6 mm, X=0 mm).

surface. Consequently strong flow is observed in the vicinity of the lower portion of the iris surface, Fig. [7-12c & 7-13d]. Plot of velocity magnitude along a line parallel to Y-axis (Z=4.6 mm, X=0mm) located inside the anterior chamber near the iris periphery show that the magnitude of velocity is high close to the part of the iris located above the hole, while in the portion of anterior chamber below the location of hole the magnitude of velocity is less in comparison to the

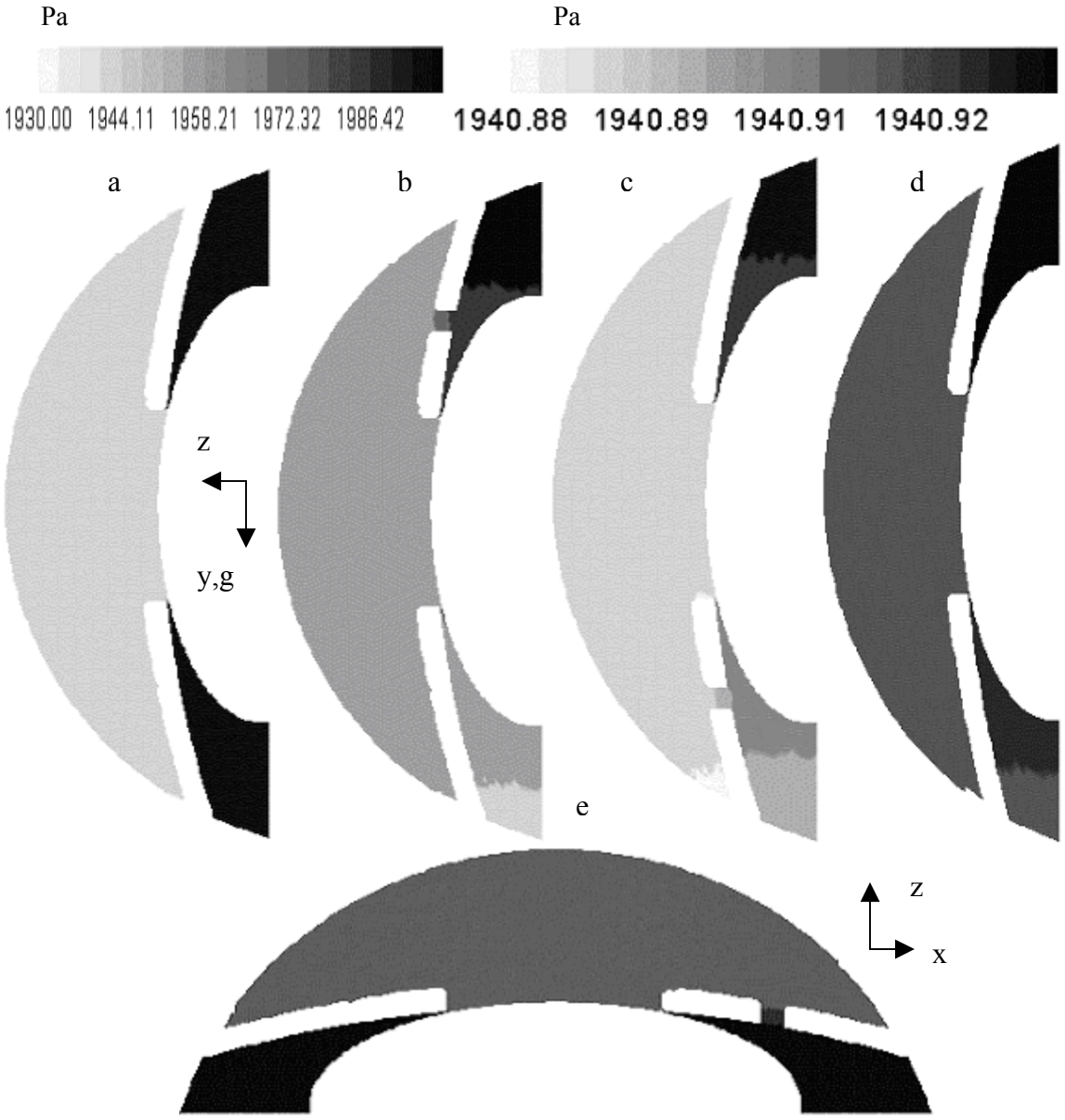

Figure 7-16: Comparison of pressure contours in vertical mid plane for the case when hole is located at two-thirds of distance between the pupil border and iris periphery. (a) Pupillary block (b) Hole located at 12 o' clock position (c) Hole located at 6 o' clock position (d) Hole located at 9 o' clock position. (e) Horizontal plane, Hole located at 9 o' clock position.

pupillary block simulation, Fig. [7-15a]. This flow pattern supports the tendency of particles present in the AH to get sedimented at the bottom of the anterior chamber as flow became less strong in this region after the iridectomy. The strong flow on the part of the lower iris surface located above the hole will prohibit the particle deposition in this location. No significant difference in flow is observed in the upper and mid portions of the anterior chamber.

For the iridectomy site at 9 o'clock central position, flow pattern show similar behaviors with respect to the peripheral iridectomy at 9 o'clock position. Flow enters the anterior chamber through the hole in the mid horizontal plane of the anterior chamber and rises against the gravity in the vertical planes passing through the hole, Fig. [7-12e & 7-13e]. The flow circulates in this vertical mid plane and finally moves towards the center of the anterior chamber, Fig [7-12e & 7-13e]. No significant difference in flow pattern and velocity magnitude is observed in the vertical mid plane, when compared with the pupillary block simulation, Fig. [7-15a]. Again like the peripheral iridectomy it introduces asymmetry across the vertical mid plane.

Fig. [7-14] shows the velocity contours and streamlines in the horizontal plane passing through the hole for 12 o'clock and 6 o'clock iridectomy and in vertical plane for 9 o'clock iridectomy. For 12 o'clock iridectomy the flow coming from the hole move towards the corneal surface in the horizontal plane after entering into the anterior chamber, Fig. [7-14a], while for 6 o'clock iridectomy the major part of the flow rises upward along the iris surface in the vertical plane, but part of the flow move in the horizontal plane along the iris surface and comes out through the TM without circulating in the anterior chamber, Fig. [7-14b]. The flow patterns in the horizontal plane passing through the hole resemble with the flow patterns of peripheral iridectomy. For 9 o'clock iridectomy, the flow moves along the iris surface against the gravity direction (Y-axis) towards the upper portion of the anterior chamber; then it descends along the cooler corneal surface; the part of the flow rising against the gravity turns towards the center of the horizontal plane passing through the hole and circulates in this plane before moving to the other planes or coming out from the TM, Fig. [7-14c].

There is no change in the velocity magnitude along a line parallel to X-axis (Y=0mm, Z=4.6mm) located inside the anterior chamber close to the anterior iris surface for 12 o'clock and 6 o'clock iridectomy, but for 9 o'clock iridectomy the velocity magnitude is high at the location of 9 o'clock hole with respect to the pupillary block simulation, Fig. [7-15b]. The increase in velocity magnitude in the vicinity of 9 o'clock hole on the X-axis is less than 6 % with respect to

the pupillary block simulation. This shows that creating hole at the central location do not bring any change in the flow profile inside the anterior chamber in the horizontal plane except for some local changes in the vicinity of the hole for 9 o'clock iridectomy. There is sharp change in the flow in the vicinity of hole-location for all positions of iridectomy, but any significant change is not observed in the rest part of the anterior chamber. When velocity magnitude is plotted along a line parallel to Z-axis (X=0mm, Y=-2.5mm), it is observed that for all positions of iridectomy, there is negligible flow through the pupillary gap (Z=3.8 mm to 4.2 mm, Fig. [7-15c]), as most of flow rushes towards the location of the hole on the iris surface. No difference is observed in velocity magnitude along the portion of this line located inside the anterior chamber (Z=4.4 mm to 7.0 mm, Fig. [7-15c]) for all positions of the iridectomy.

Like the peripheral iridectomy, the opening of holes in the central position releases the pressure of the posterior chamber. For the pupillary block the pressure difference between the posterior and anterior chamber is around 60 Pa, Fig. [7-14a], which diminishes to 0.05 Pa, Fig. [7-14b-e & 7-15d], after the iridectomy. Iridectomy does not bring any significant change in the anterior chamber pressure distribution and the pressure magnitude is almost constant (~1940 Pa) in the anterior chamber for both pupillary block and iridectomy simulations, Fig. [7-15d].

The contours of velocity magnitude and streamlines in a vertical plane parallel to the equatorial plane located inside the posterior chamber (Z=2.6 mm) do not show any significant difference from the peripheral iridectomy simulations. Hole created for the direct passage of flow into the anterior chamber introduces asymmetry in the flow pattern of posterior chamber for all locations of iridectomy simulated in the present model, Fig. [7-17-d].

For analyzing the flow profile in the posterior chamber after creation of holes, the velocity magnitude is plotted along a line parallel to Y-axis, Fig. [7-18a], and along a line parallel to X-axis, Fig. [7-18b], located on a vertical plane (parallel to the equatorial plane) inside the posterior chamber (Z=2.6 mm). Like the simulations for the central location of the holes, the

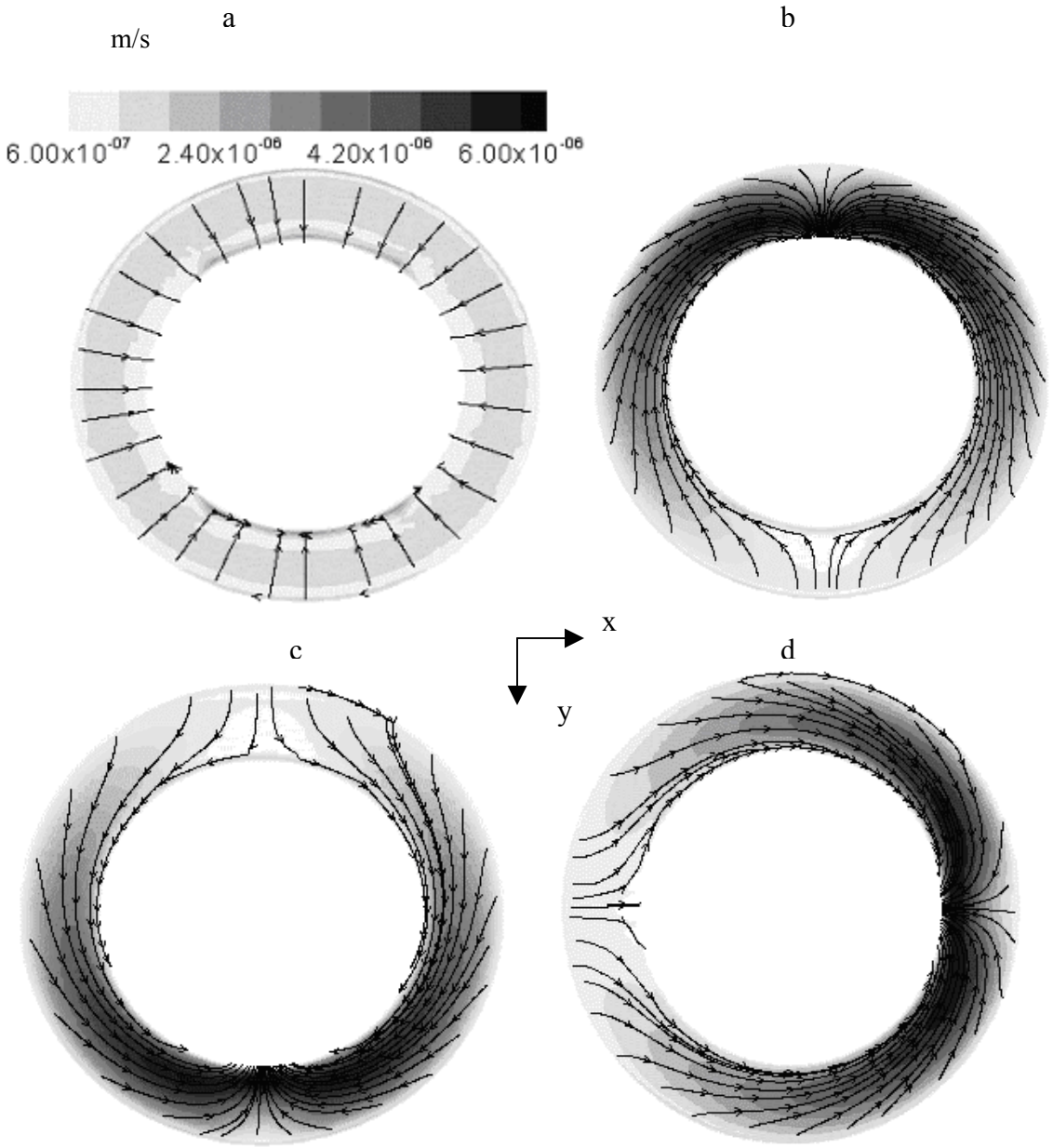

Figure 7-17: Comparison of streamlines and contours of velocity magnitude in plane parallel to equatorial plane (z = 2.6) for the case of iridectomy when hole is located at two-thirds of distance between the pupil border and iris periphery. (a) Pupillary block (b) Hole located at 12 o' clock position (c) Hole located at 6 o' clock position (d) Hole located at 9 o' clock position.

velocity magnitude increases to a high value ($10\ \mu m/s$), Fig. [7-18-a-b], in the vicinity of the location of the holes, but increase in the velocity is less than increase in the velocity at the corresponding location for the central iridectomy ($26\ \mu m/s$). This trend is observed for all three locations of the holes, Fig. [7-18a-b]. It is observed that for 12 o'clock hole, Fig. [7-18a], for

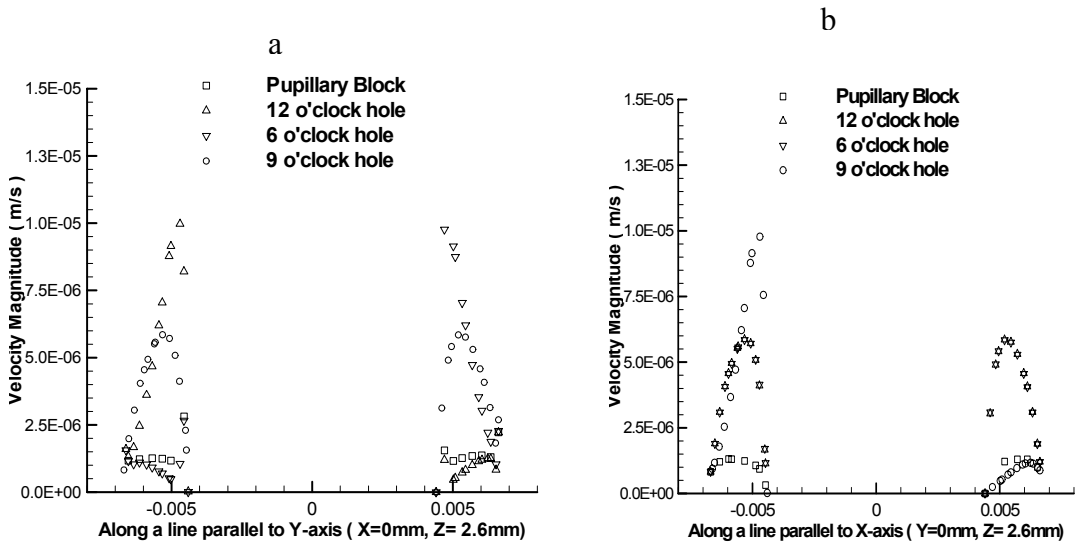

Figure 7-18: Iridectomy with hole located at two-thirds of distance between the pupil border and iris periphery, Vertical Orientation, Comparison of velocity magnitude among pupillary block and various locations of holes. (a) Along a line parallel to Y-axis (X=0mm, Z=2.6mm) located inside the posterior chamber. (b) Along a line parallel to X-axis (Y=0mm, Z=2.6mm) located inside the posterior chamber.

6o'clock hole, Fig. [7-18a], and for 9 o'clock hole, Fig. [7-18b], the velocity magnitude (1 $\mu m/s$) just opposite to the hole decreases in comparison to the corresponding velocity magnitude in pupillary block simulation (1.2 $\mu m/s$). On the axis perpendicular to the axis of hole-location, the velocity magnitude increases to 6 $\mu m/s$ for all location of holes, Fig. [7-18a-b], which is 5 times greater in comparison to the velocity magnitude at the corresponding location in pupillary block simulation. The above analysis reflects that flow is rushing towards the location of the hole after secretion from the ciliary body located around the posterior chamber and asymmetry in the flow profile of the posterior chamber is created like the peripheral iridectomy.

7.2.3 Two Hole Iridectomy at Central Locations in Vertical Orientation

Iridectomy with one hole at any location (peripheral or central) creates asymmetry either across the vertical mid plane or across the horizontal mid plane. So for maintaining the symmetry of the flow profile iridectomy with two holes is analyzed. In the real surgery one or two holes are created in the iris disc depending upon the specific requirements [53]. Both the holes are chosen

at the central location at a distance from the iris-tip, which is two-thirds of distance between the pupil border and iris periphery. The center of the hole is located at 4 mm distance from the central axis (Z-axis) and the diameter of the hole is taken as 0.5 mm for all the simulations. Two

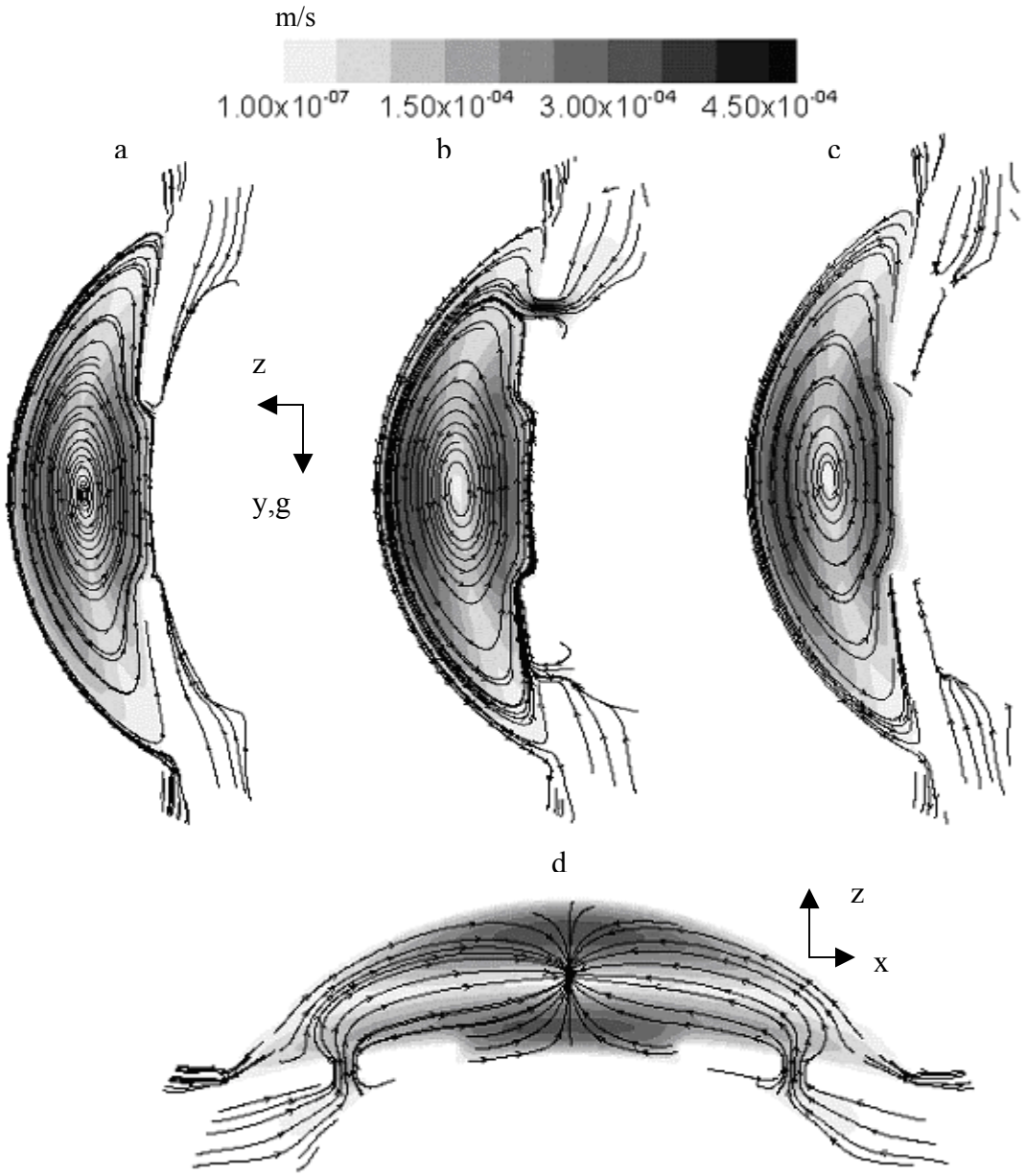

Figure 7-19: Comparison of streamlines and contours of velocity magnitude for the case of iridectomy when holes are located at two-thirds of distance between the pupil border and iris periphery. (a) Pupillary block, Vertical mid plane (b) Holes located at 12 o' & 6 o' clock position, Vertical mid plane (c) Holes located at 9 o' & 3 o' clock position, Vertical mid plane (d) Holes located at 9 o' & 3 o'clock position, Horizontal plane.

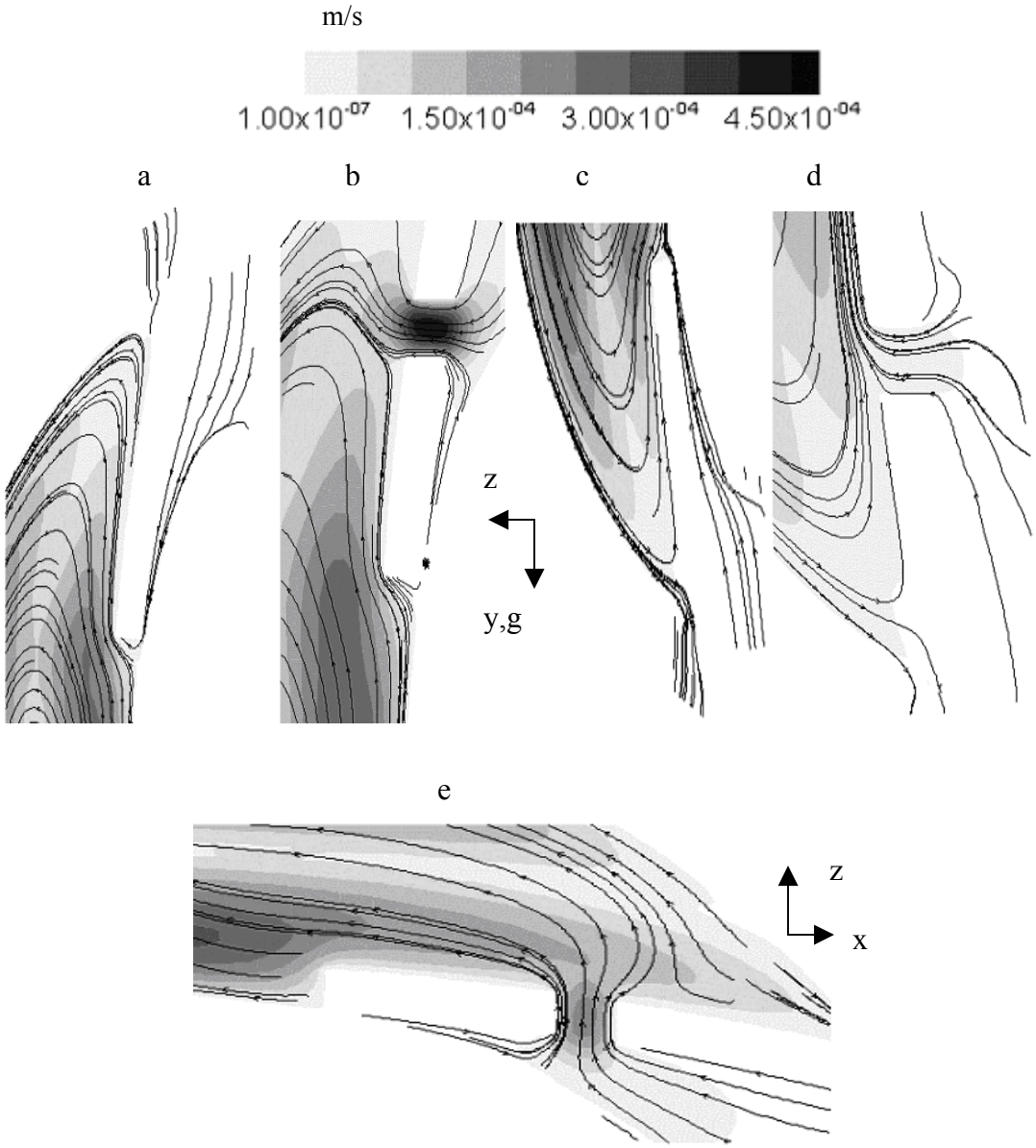

Figure 7-20: Extended view of streamlines and contours of velocity magnitude for the case of iridectomy when holes are located at two-thirds of distance between the pupil border and iris periphery. (a) Pupillary block, Upper portion of iris in vertical mid plane (b) Hole located at 12 o'clock position for 12 o' & 6 o' clock position iridectomy, Vertical mid plane (c) Pupillary block, Lower portion of iris in vertical mid plane (d) Hole located at 6 o'clock position for 12 o' & 6 o' clock position iridectomy, Vertical mid plane (e) Hole located at 9 o' clock position for 9 o' & 3 o'clock position iridectomy, Horizontal plane.

simulations with different arrangements of holes are compared. In one simulation holes are

located at 12 & 6 o'clock position, while in the other simulation holes are located at 9 & 3

o'clock position.

For 12 & 6 o'clock hole iridectomy most of the flow enters into the anterior chamber through the hole located at 12 o'clock position, Fig. [7-19b & 7-20b]. The velocity magnitude in the hole located at 6 o'clock position is very low compared to the velocity magnitude in the hole at 12 o'clock, Fig. [7-19b & 7-20b]. The relatively weak flow from 6 'o clock hole is the consequence of the pressure distribution in the posterior chamber. Because of the buoyancy pressure in the upper portion of the posterior chamber is relatively high compared to the pressure in the bottom part of the posterior chamber. So the pressure differential between the posterior and anterior chamber at the 12 o'clock hole is high compared to the pressure differential between the two chambers at the 6 o'clock hole, Fig. [7-22b]. This high-pressure differential compels most of the flow to enter into the anterior chamber through the hole at 12 o'clock. Plot of velocity magnitude along a line parallel to Y-axis (Z=4.6 mm, X=0mm) located inside the anterior chamber close to the iris periphery show that the magnitude of velocity is high in the vicinity of the hole opening at 12 o'clock position in comparison to the pupillary block simulation, while no significant change is observed at 6 o'clock hole, Fig. [7-21a]. Any significant difference is not observed on the mid or bottom portion of the anterior chamber. For the pupillary block the highest magnitude of velocity (475 μm /s) is observed in the pupillary gap, while after the iridectomy the highest velocity (431 μm /s) is observed inside the iris hole at 12 o'clock. The creation of hole at 6 o'clock in addition to 12 o'clock hole does not bring any significant change in the flow distribution inside the eye. So, there is no additional advantage of making two holes in this arrangement.

When iridectomy sites are located at 9 & 3 o'clock position, the flow enters the anterior chamber through both the holes. There is equal distribution of flow in both of the holes and flow patterns are symmetrical across the vertical mid plane, Fig. [7-19d & 7-20e], which is not observed with single hole iridectomy. Flow enters in the mid horizontal plane of the anterior

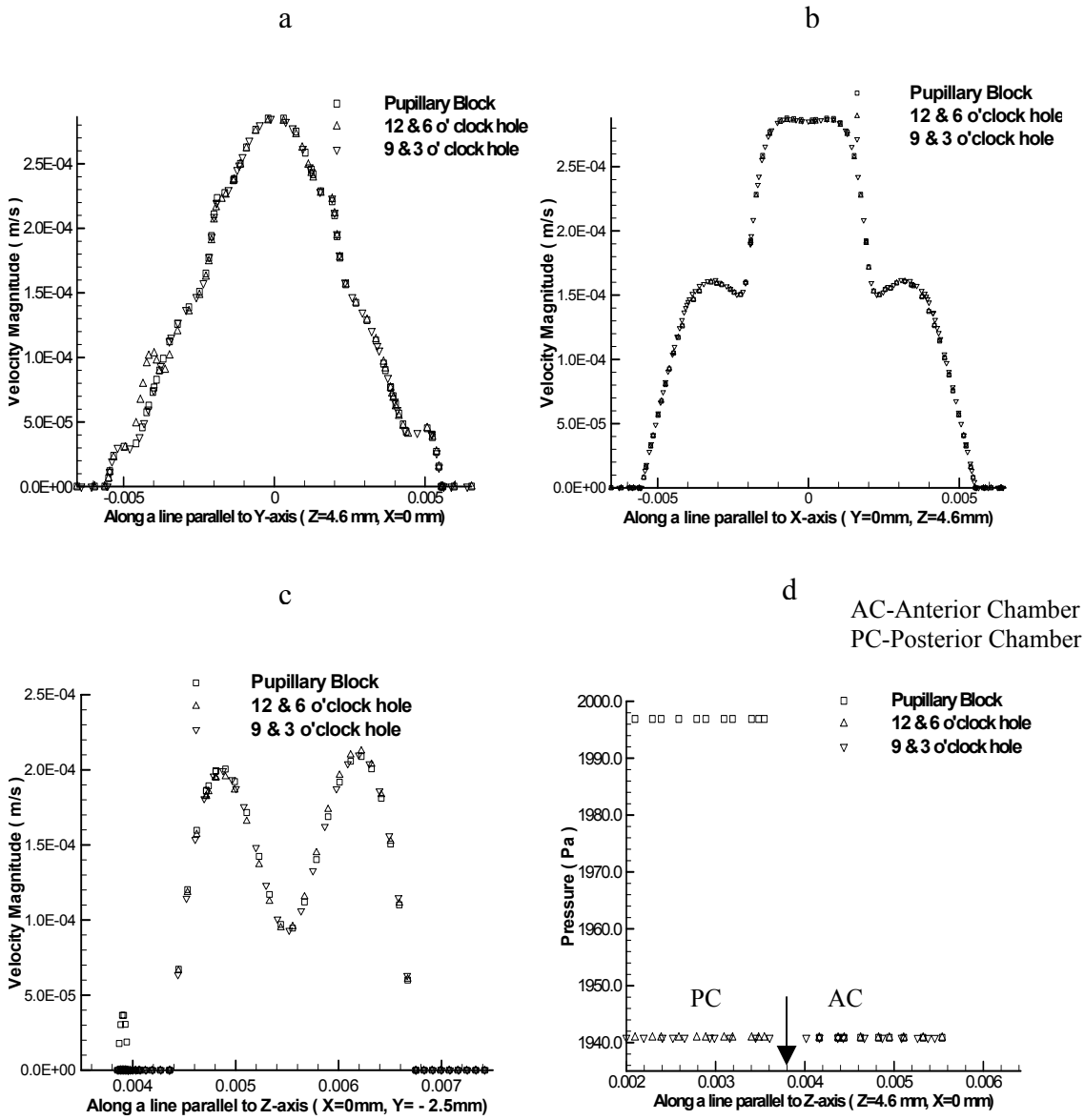

Figure 7-21: Iridectomy with holes located at two-thirds of distance between the pupil border and iris periphery, Vertical Orientation, Comparison among pupillary block, 12 & 6 o'clock hole and 9 & 3 o'clock hole (a) Of velocity magnitude along a line parallel to Y-axis (Z=4.6 mm, X=0 mm) located inside the anterior chamber close to the iris periphery (b) Along a line parallel to X-axis (Y=0mm, Z=4.6mm) inside the anterior chamber close to the iris periphery. (c) Along a line parallel to Z-axis (X=0 mm, Y= -2.5mm). (d) Of pressure magnitude along a line parallel to Z-axis (Y=4.6 mm, X=0 mm).

chamber through both the holes and rises against the gravity in the vertical planes passing through the respective holes. The flow circulates in these vertical planes and finally moves towards the center of the anterior chamber, Fig. [7-19d]. No significant difference in the flow pattern and in the velocity magnitude is observed in the vertical mid plane, when compared with the pupillary block simulation, Fig. [7-19a & 7-19c]. For the pupillary block, the highest magnitude of velocity

(475 μm /s) is observed in the pupillary gap, while after the iridectomy the highest velocity (225 μm /s) is observed inside the holes.

There is no change in the velocity magnitude along a line parallel to X-axis (Y=0mm, Z=4.6mm) located inside the anterior chamber next to the anterior iris surface for both the arrangements of the holes in double hole iridectomy, Fig. [7-21b]. There is sharp change in the velocity magnitude of flow in the vicinity of hole-locations, but any significant change is not observed in the rest part of the anterior chamber. When velocity magnitude is plotted along a line parallel to Z-axis (X=0mm, Y=-2.5mm), it is observed that for all positions of iridectomy, there is negligible flow through the pupillary gap (Z=3.8 mm to 4.2 mm, Fig. [7-21c]), as most of the flow rushes towards the location of the hole on the iris surface. No difference is observed in the velocity magnitude along the portion of this line located inside the anterior chamber (Z=4.4 mm to 7.0 mm, Fig. [7-21c]) for both the hole arrangements at the central locations.

The pressure distribution inside the anterior and posterior chamber with the opening of two holes is not different from the pressure distribution with single hole. Like the single-hole iridectomy, the pressure differential of 60 Pa between the anterior and posterior chamber come down to 0.05 Pa, Fig. [7-22a–7-22d, 7-21d] after the iridectomy. Iridectomy does not bring any significant change in the anterior chamber pressure distribution and the pressure magnitude is almost constant (~1940 Pa) in the anterior chamber.

The contours of velocity magnitude and streamlines in a vertical plane parallel to the equatorial plane located inside the posterior chamber (Z=2.6 mm) show that for 12 & 6 o'clock iridectomy flow rushes towards the hole located at 12 o'clock position, Fig. [7-23b]. There is almost negligible flow towards the hole located at 6 o'clock position, Fig. [7-23b]. So, making two holes in this arrangement does not help to maintain the symmetry in the flow profile of the posterior chamber. When holes are created at 9 & 3 o'clock position, the flow rushes towards the both holes in symmetrical fashion, Fig. [7-23c]. This is the major advantage of the iridectomy in

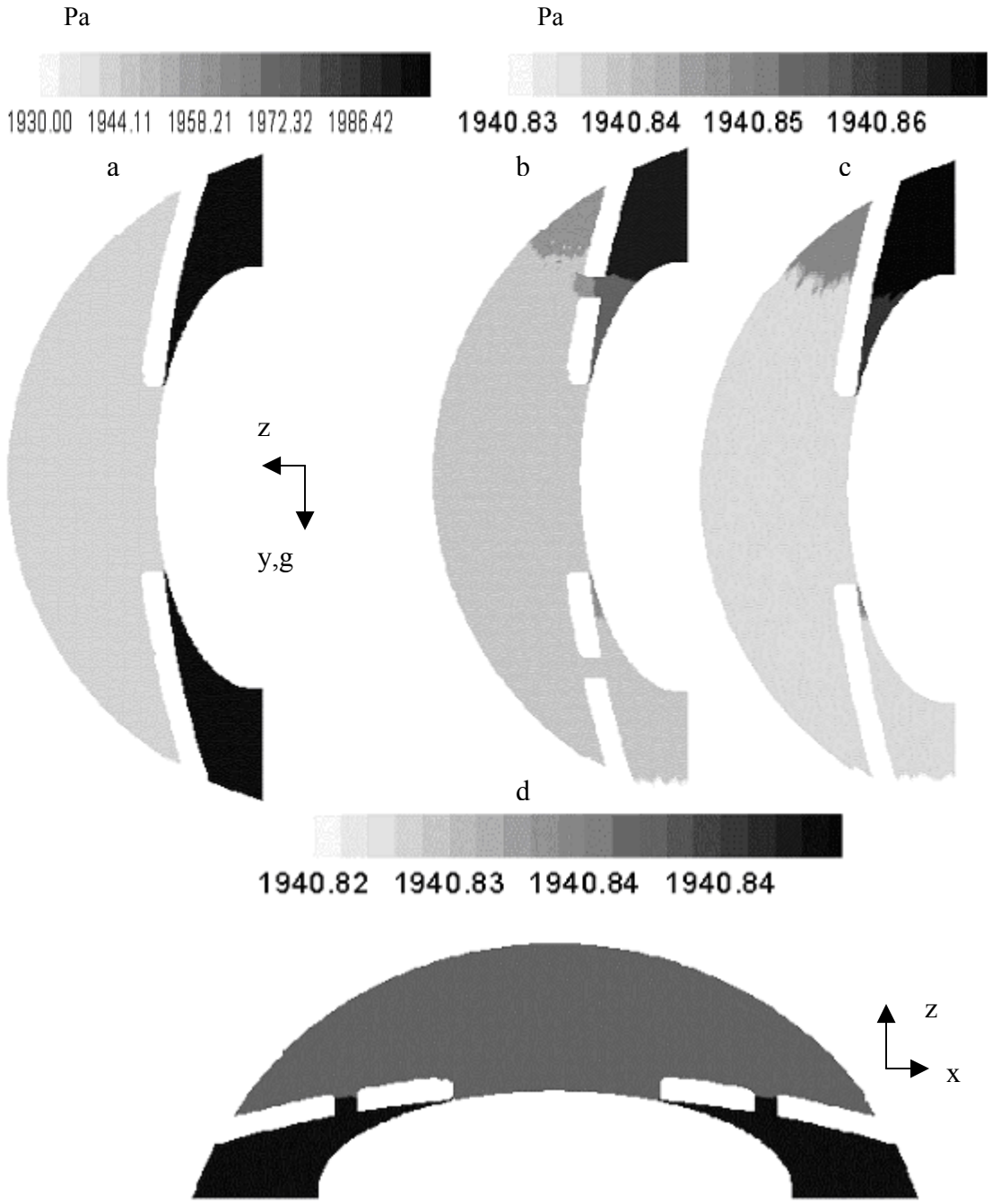

Figure 7-22: Comparison of pressure contours for the case of iridectomy when holes are located at two-thirds of distance between the pupil border and iris periphery. (a) Pupillary block, Vertical mid plane (b) Holes located at 12 o' & 6 o' clock position, Vertical mid plane (c) Holes located at 9 o' & 3 o' clock position, Vertical mid plane (d) Holes located at 9 o' & 3 o'clock position, Horizontal plane.

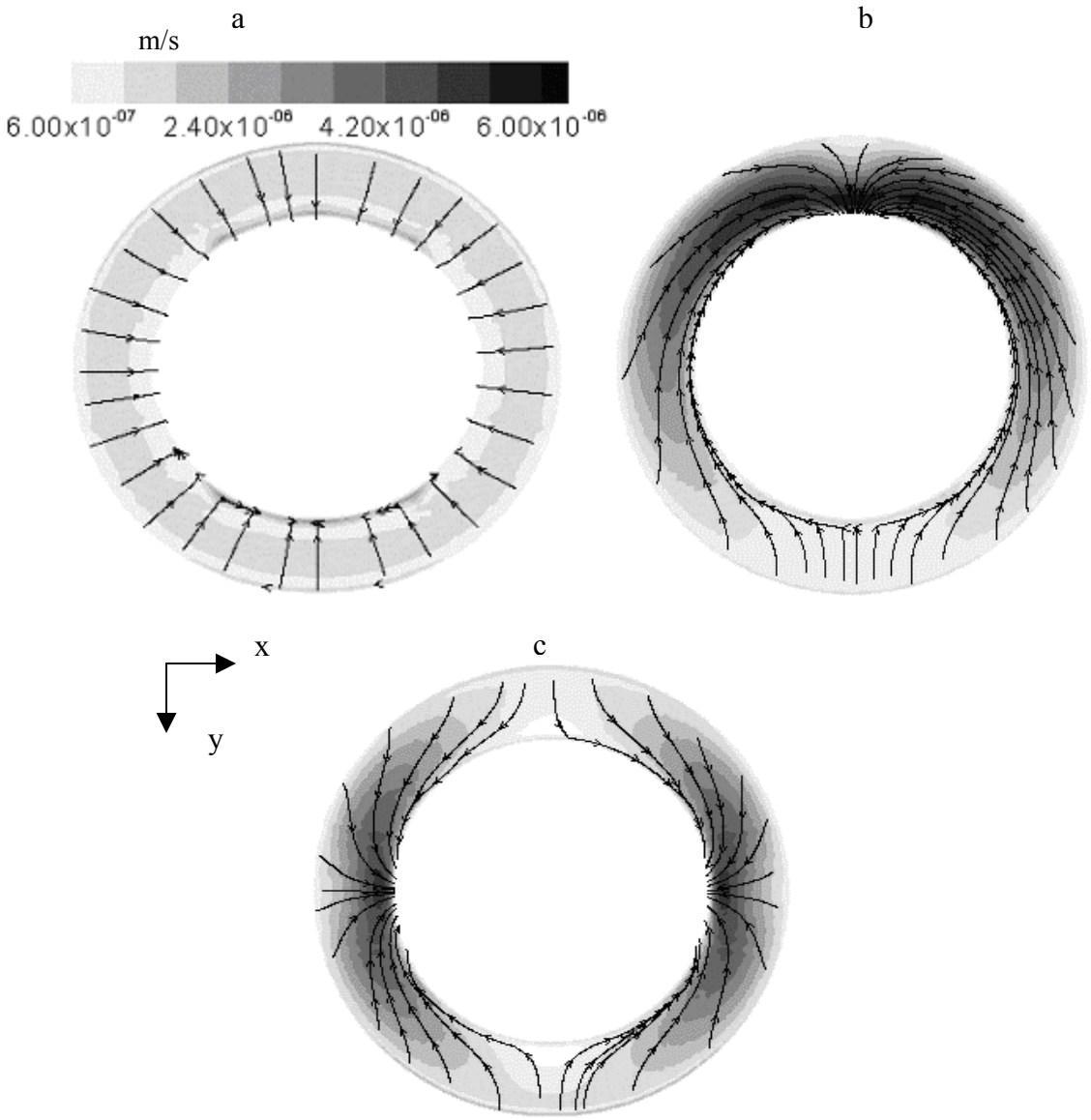

Figure 7-23: Comparison of streamlines and contours of velocity magnitude in plane parallel to equatorial plane (z = 2.6) for the case of iridectomy when holes are located at two-thirds of distance between the pupil border and iris periphery. (a) Pupillary block (b) Holes located at 12 o' & 6 o' clock position (c) Holes located at 9 o' & 3 o' clock position.

this arrangement as symmetry is maintained in both the posterior chamber and anterior chamber. Any impairment in ocular tissues due to the asymmetric nutrition of ocular tissues is not probable. The velocity magnitude is plotted along a line parallel to Y-axis, Fig. [7-24a], and along a line parallel to X-axis, Fig. [7-24b], located on a vertical plane (parallel to the equatorial plane) inside the posterior chamber (Z=2.6 mm) to analyze the flow profile in the posterior chamber for two different arrangements of the double holes. It is observed that for 12 o'clock & 6 o'clock hole

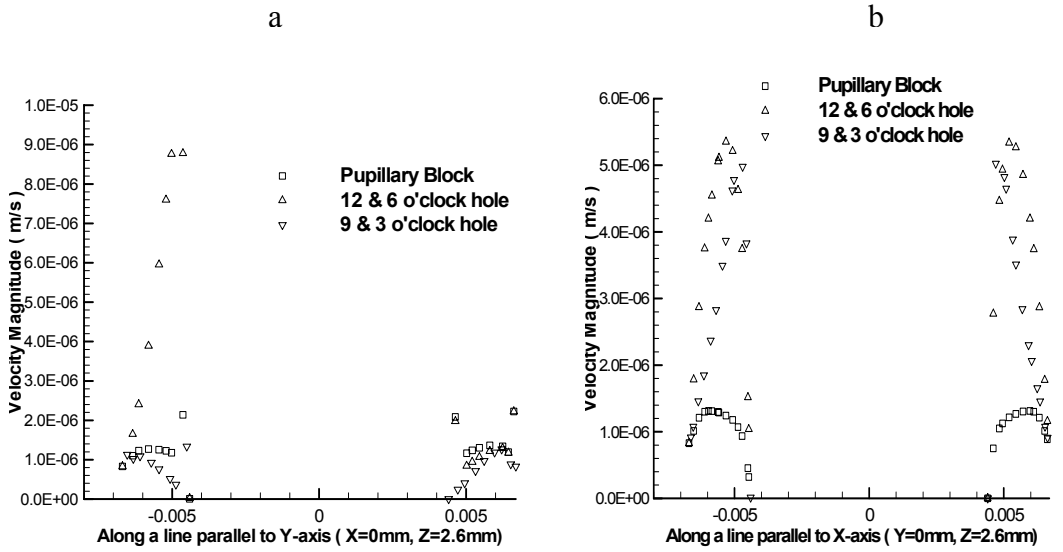

Figure 7-24: Iridectomy with holes located at two-thirds of distance between the pupil border and iris periphery, Vertical Orientation, Comparison of velocity magnitude among pupillary block, 12 & 6 o'clock hole and 9 & 3 o'clock hole. (a) Along a line parallel to Y-axis (X=0mm, Z=2.6mm) located inside the posterior chamber. (b) Along a line parallel to X-axis (Y=0mm, Z=2.6mm) located inside the posterior chamber.

arrangement, the velocity magnitude increases to 9 $\mu m/s$ in the vicinity of 12 o'clock hole, but at the location close to 6 o'clock hole, the velocity magnitude is even less than the pupillary block simulation (1.2 $\mu m/s$). This shows that making an additional hole at 6 o'clock with 12 o'clock hole do not accelerate the flow towards the 6 o'clock hole, Fig. [7-24a] and most of the flow is rushing towards the hole located in the upper part of the iris i.e. 12 o'clock hole. For this arrangement of the holes, at 9 o'clock and 3 o'clock locations the velocity magnitude increases to 5.5 $\mu m/s$, which is approximately 5 times greater than the corresponding value in pupillary block simulation, Fig. [7-24b]. As flow from the bottom of the posterior chamber is rushing towards the location of 12 o'clock hole, at mid way locations of 9 and 3 o'clock high velocity is observed. For 9 and 3 o'clock holes, the velocity magnitude at the both hole locations increases to 5 $\mu m/s$, Fig. [7-24b], which is approximately 5 times increase with respect to the corresponding velocity magnitude in pupillary block simulation. In this arrangement of the holes, on the axis perpendicular to the axis of the holes, the velocity magnitude even decreases with respect to the

pupillary block simulation, Fig. [7-24a]. As from both 12 o'clock and 6 o'clock locations the flow is rushing towards the hole locations at 9 and 3 o'clock hole, so velocity magnitude is very less at 12 o'clock & 6 o'clock locations.

7.2.4 Peripheral Iridectomy in Horizontal Orientation

For the horizontal orientation (sleeping case), all the above location of holes (12, 9 & 6 o'clock iridectomy) on the iris periphery yields similar results due to axis-symmetry of the model. The velocity contours and streamlines in the vertical mid plane show that most of the flow enters into the anterior chamber through the hole and there is almost negligible flow through the pupil, Fig. [7-25b]. The flow entering into the anterior chamber from the hole move along the iris surface towards the center and then rises against the gravity towards the cornea. It takes sharp bend due to the corneal resistance and descends along the corneal surface. The flow keeps on circulating in the vertical plane until it reaches to the center of the vortex. Finally it move to the other vertical plane while circulating until it come close to the TM from where it comes out from the TM, Fig. [7-25b & 7-25d]. Plot of velocity magnitude along a line parallel to Y-axis (Z=4.6 mm, X=0mm) located inside the anterior chamber close to the iris periphery show that velocity-magnitude is high in the vicinity of the iris surface in comparison to the pupillary block simulation, Fig. [7-33a]. Any significant difference is not observed on the mid or other side of the anterior chamber. Plot of velocity magnitude along a line parallel (Y=3.5 mm, X=0 mm) to the central axis (Z-axis) show that there is no flow towards the pupillary gap in the posterior chamber after opening of the holes (Z=3.2 mm to 3.6 mm, Fig. [7-33b]). In the vicinity of the iris surface (Z=4.2 mm to 5.2 mm, Fig. [7-33b]) the magnitude of flow velocity is relatively high (max = 40 μm /s) for the iridectomy simulation compared to the pupillary block simulation (max = 32 μm /s), while in the vicinity of the corneal surface (Z=5.2 mm to 6.2 mm, Fig. [7-33b]), the velocity magnitude (max = 30 μm /s) is less than the pupillary block simulation (max = 36 μm /s). For the pupillary block the highest magnitude of velocity (475 μm /s) is observed in the

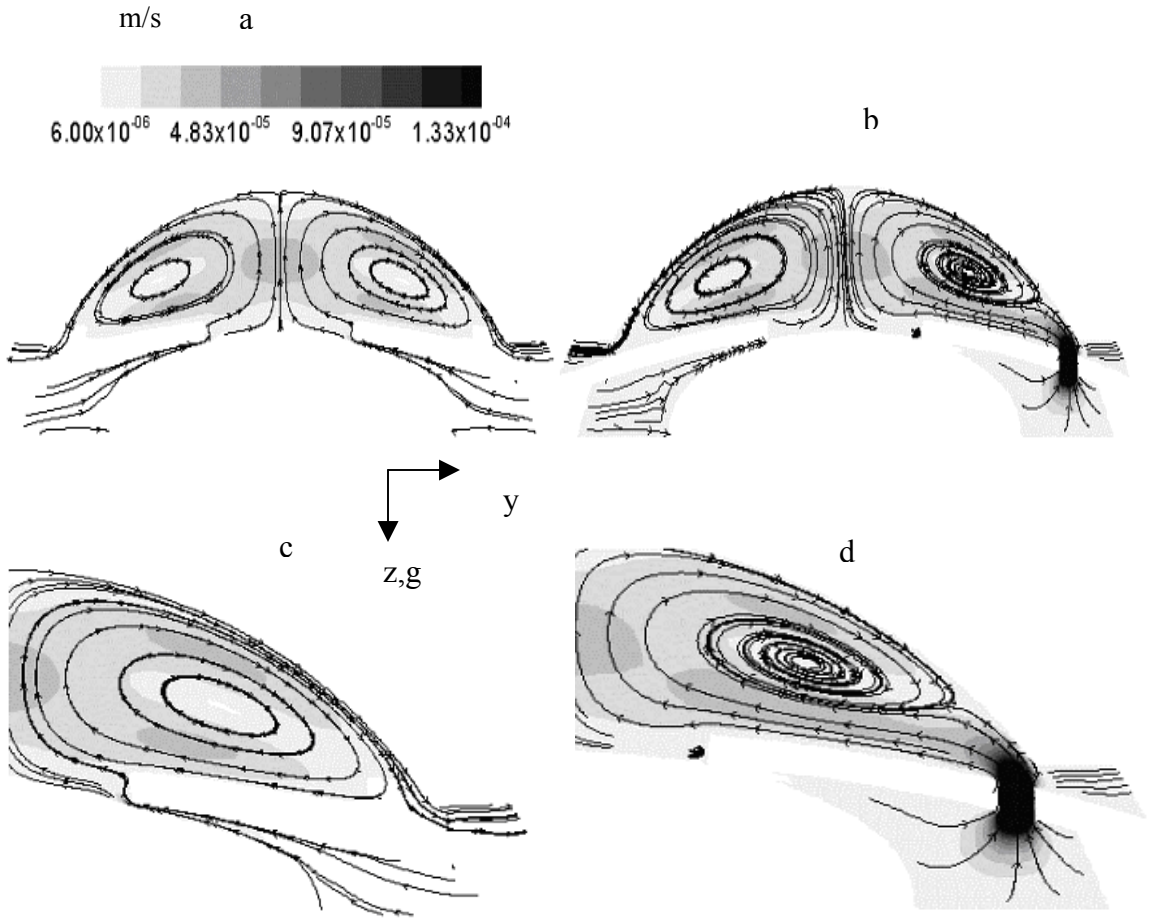

Figure 7-25: Comparison of streamlines and contours of velocity magnitude in vertical mid plane for the case of iridectomy when hole is located next to the iris root, Horizontal orientation. (a) Pupillary block (b) Hole opening (a) Pupillary block, extended view (b) Hole opening, extended view.

pupillary gap, while after iridectomy the highest velocity (448 μm /s) is observed in the iris hole.

To compare the pressure distribution between the pupillary block and iridectomy simulation, pressure contours are plotted in the vertical mid plane. Like the vertical orientation, for the pupillary block the pressure difference between the posterior and anterior chamber is around 60 Pa, Fig. [7-26a & 7-26b], which diminishes to 0.05 Pa for the iridectomy simulation, Fig. [7-31a]. The pressure (~1940 Pa) in the anterior chamber is same for pupillary block and iridectomy simulations, Fig [7-31a]. The contours of velocity magnitude and streamlines in a vertical plane parallel to the equatorial plane located inside the posterior chamber (Z=2.6 mm) show that symmetry in the flow pattern of posterior chamber is completely destroyed by

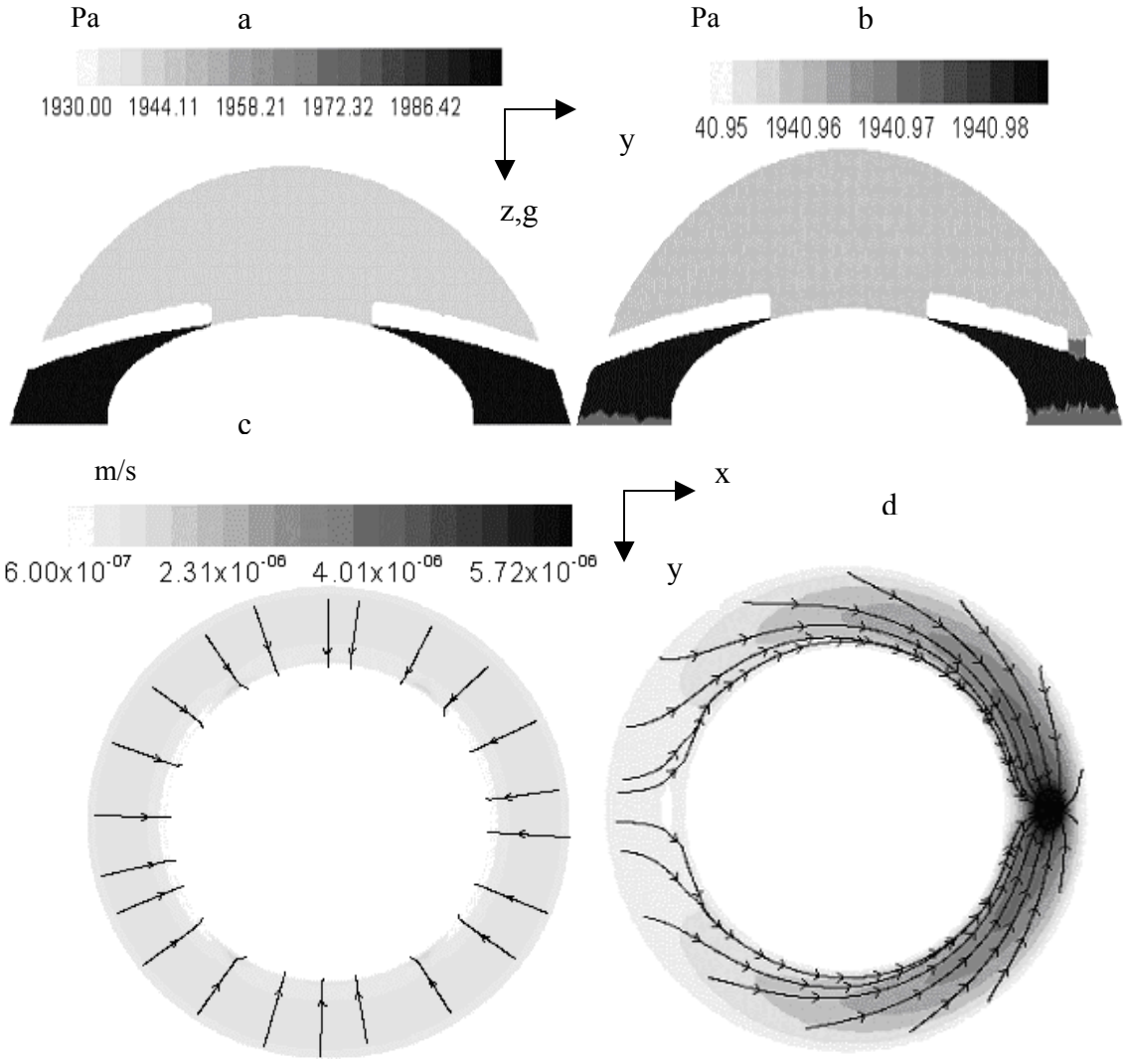

Figure 7-26: Comparison of pressure contours in vertical mid plane for the case of iridectomy when hole is located next to the iris root, Horizontal orientation. (a) Pupillary block (b) Hole opening. Comparison of streamlines and contours of velocity magnitude in plane parallel to equatorial plane (z = 2.6) for the case of iridectomy when hole is located next to the iris root, Horizontal orientation (c) Pupillary block (d) Hole opening.

creation of the hole. For the pupillary block simulation, AH move from the ciliary body surface toward the pupillary gap, Fig. [7-26c], while for iridectomy simulation, AH rushes towards the hole in the iris surface, Fig. [7-26d].

7.2.5 Central Iridectomy in Horizontal Orientation

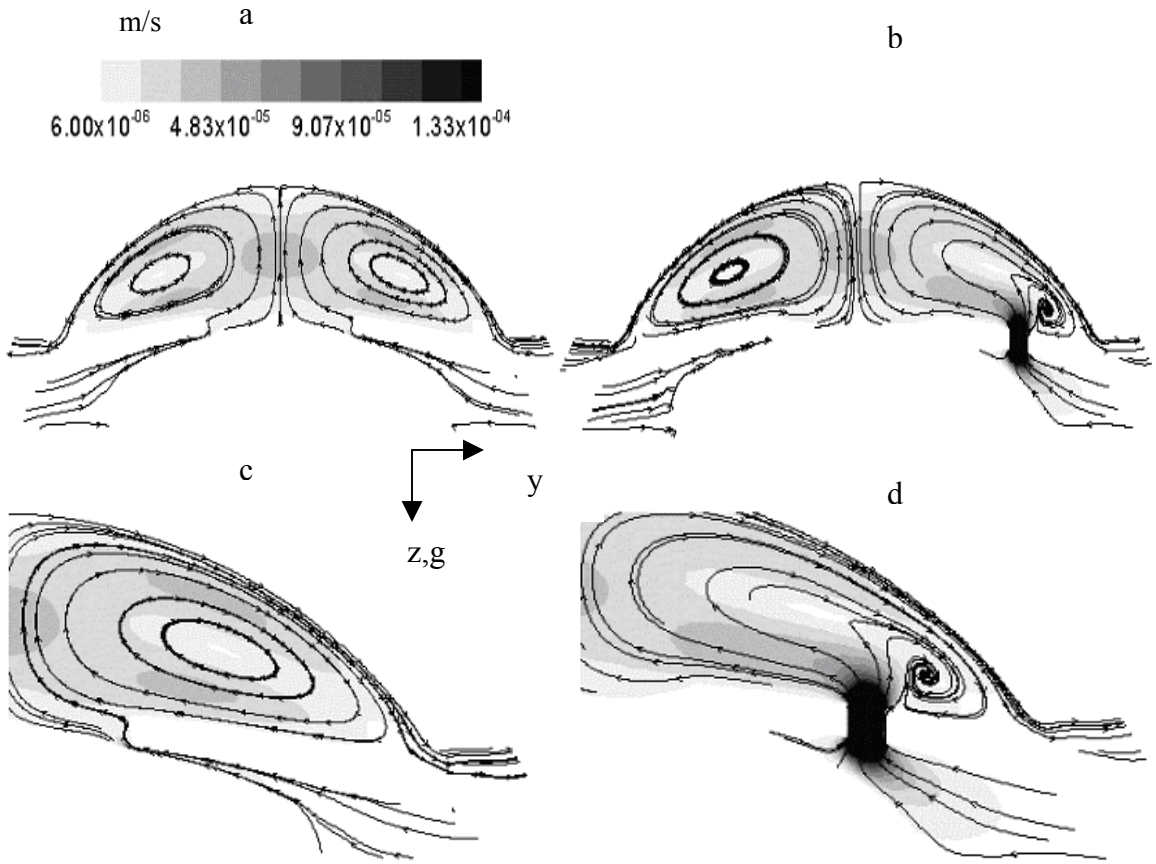

Figure 7-27: Comparison of streamlines and contours of velocity magnitude in vertical mid plane for the case of iridectomy when hole is located at two-thirds of distance between the pupil border and iris periphery, Horizontal orientation. (a) Pupillary block (b) Hole opening (a) Pupillary block, extended view (b) Hole opening, extended view.

The velocity contours and streamlines in the vertical mid plane show that like peripheral iridectomy most of the flow enters into the anterior chamber through the hole and there is almost negligible flow through the pupil, Fig. [7-27b]. Part of the flow entering into the anterior chamber from the left portion of the hole (part of hole close to the lens) move along the iris surface towards the center and then rises against the gravity towards the cornea. It takes sharp bend due to the corneal resistance and descends along the corneal surface and finally comes out from the TM, Fig. [7-27b]. Part of the flow coming from the right side of the hole (part of the hole close to TM) move towards the TM and circulate in the anterior chamber angle at the juncture of the corneal

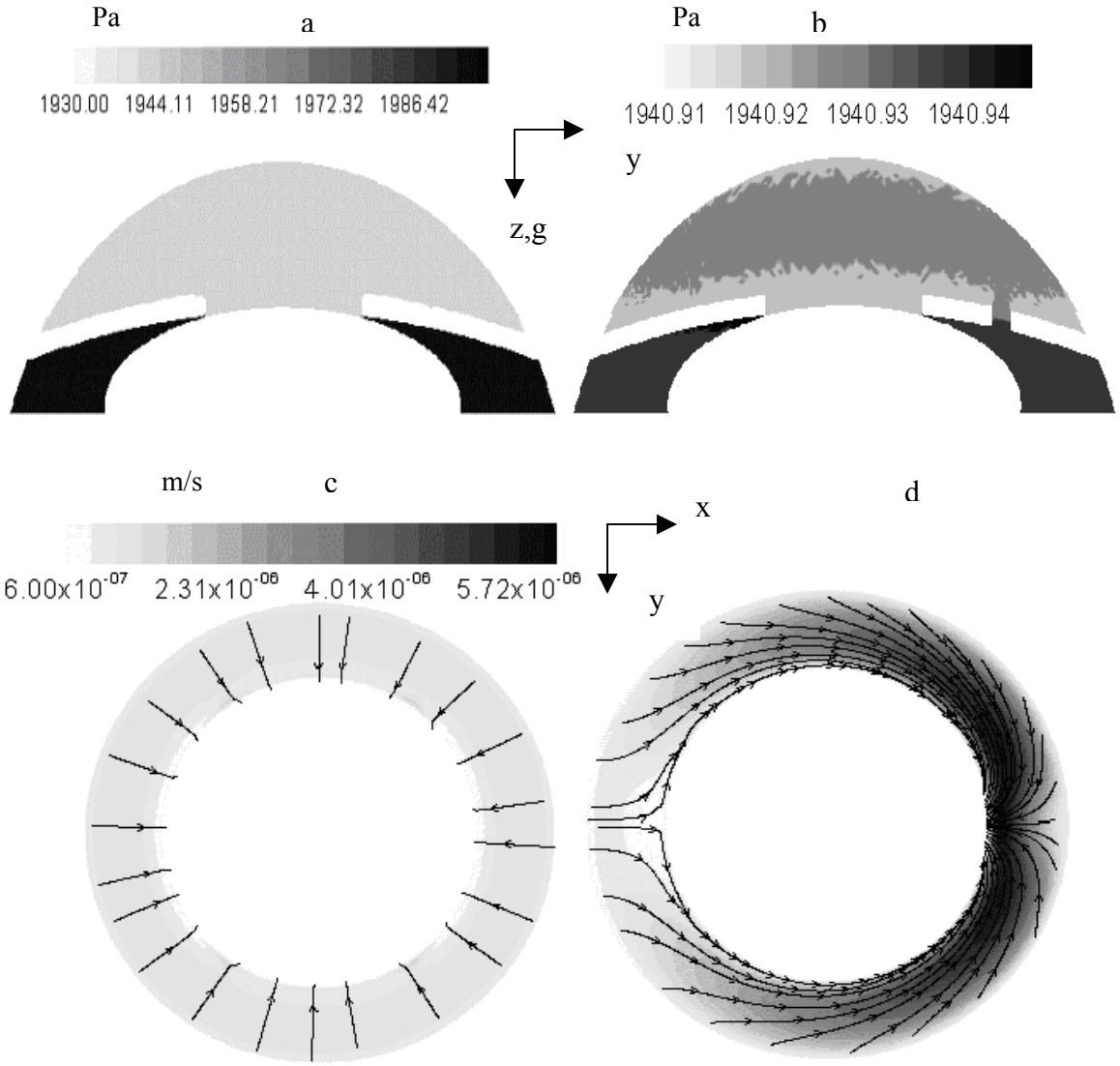

Figure 7-28: Comparison of pressure contours in vertical mid plane for the case of iridectomy when hole is located at two-thirds of distance between the pupil border and iris periphery, Horizontal orientation. (a) Pupillary block (b) Hole opening. Comparison of streamlines and contours of velocity magnitude in plane parallel to equatorial plane (z = 2.6) for the case of iridectomy when hole is located at two-thirds of distance between the pupil border and iris periphery, Horizontal orientation (c) Pupillary block (d) Hole opening.

surface and TM. While circulating it moves to the other vertical planes passing through the central axis until it come close to the TM from where it comes out from the anterior chamber, Fig. [7-27b & 7-27d].

Plot of velocity magnitude along a line parallel to Y-axis (Z=4.6 mm, X=0mm) located inside the anterior chamber close to the iris periphery show that velocity-magnitude is high in the

vicinity of the iris surface in comparison to the pupillary block simulation, Fig. [7-33a]. Any significant difference is not observed on the mid or the other side of the anterior chamber. Plot of velocity magnitude along a line parallel (Y=3.5 mm, X=0mm) to the central axis (Z-axis) show that there is no flow towards the pupillary gap in the posterior chamber after opening of the holes (Z=3.2 mm to 3.6 mm, Fig. [7-33b]). In the vicinity of the iris surface (Z=4.2 mm to 5.2 mm, Fig. [7-33b]) the magnitude of flow velocity is high (max = 52 μm /s) for the iridectomy simulation compared to pupillary block simulation (max = 36 μm /s), while in the vicinity of the corneal surface (Z=5.2 mm to 6.2 mm, Fig. [7-3b]), the velocity magnitude (max = 28 μm /s) is less than the pupillary block simulation (max = 32 μm /s). The flow pattern reflect high probability of particle deposition on the corneal surface in the proximity of the hole due to the relatively weak flow with respect to pupillary block simulation and low probability of particle deposition on the iris surface close to the hole due to the strong flow.

The pressure contours in the vertical mid plane show behavior similar to the peripheral iridectomy, Fig. [7-28a & 7-28b]. The contours of velocity magnitude and streamlines in a vertical plane parallel to the equatorial plane and located inside the posterior chamber (Z=2.6 mm) show that symmetry in the flow pattern of posterior chamber is completely destroyed by creation of hole, Fig. [7-28c& 7-28d], which is again similar to the peripheral iridectomy simulations in the horizontal orientation.

7.2.6 Two Hole Central Iridectomy in Horizontal Orientation

The velocity contours and streamlines in the vertical mid plane for two-hole iridectomy at central location show symmetry across the central axis for the horizontal orientation of the eye, i.e., the flow pattern is similar in both the holes, Fig. [7-29b]. The flow enters into the anterior chamber through the holes and there is almost negligible flow through the pupil. Part of the flow entering into the anterior chamber from the left portion of hole (part of hole close to the lens) move along the iris surface towards the center and then rises against the gravity towards the

cornea. It takes sharp bend due to the corneal resistance and descends along the corneal surface. Part of the flow descending along the corneal surface comes out from the TM, while other part circulates in the anterior chamber and move towards the center of the vortex, Fig. [7-29b & 7-29d]. Part of the flow coming from the right side of the hole (part of the hole close to TM) move towards the center of the vortex. The other part move towards the other small vortex observed in the vicinity of the TM and circulates in the anterior chamber angle at the juncture of the corneal surface and TM, Fig. [7-29b & 7-29d]. The flow circulating in the bigger vortex move to the other vertical planes passing through central axis until it come close to the TM from where it comes out from the anterior chamber.

Plot of velocity magnitude along a line parallel to Y-axis (Z=4.6 mm, X=0mm) located inside the anterior chamber close to the iris periphery show that velocity-magnitude is high in the vicinity of the iris surface in comparison to the pupillary block simulation, Fig. [7-33a]. Plot of velocity magnitude along a line parallel (Y=3.5 mm, X=0mm) to the central axis (Z-axis) show that there is no flow towards the pupillary gap in the posterior chamber after opening of the holes (Z=3.2 mm to 3.6 mm, Fig. [7-33b]). In the vicinity of the iris surface (Z=4.2 mm to 5.2 mm, Fig. [7-33b]) the magnitude of flow velocity is high (max = 42 μm /s) for the iridectomy simulation compared to pupillary block simulation (max = 32 μm /s), while in the vicinity of the corneal surface (Z=5.2 mm to 6.2 mm, Fig. [7-33b]), the velocity magnitude (max = 32 μm /s) is less than the pupillary block simulation (max = 36 μm /s), Fig. [7-33b].

The pressure contours in the vertical mid plane show behavior similar to the single-hole iridectomy, Fig. [7-30a & 7-30b]. The contours of velocity magnitude and streamlines in a vertical plane parallel to the equatorial plane and located inside the posterior chamber (Z=2.6 mm) show symmetry in the flow pattern of posterior chamber across both the horizontal and vertical mid planes, Fig. [7-30c & 7-30d]. The velocity magnitude is plotted along a line parallel

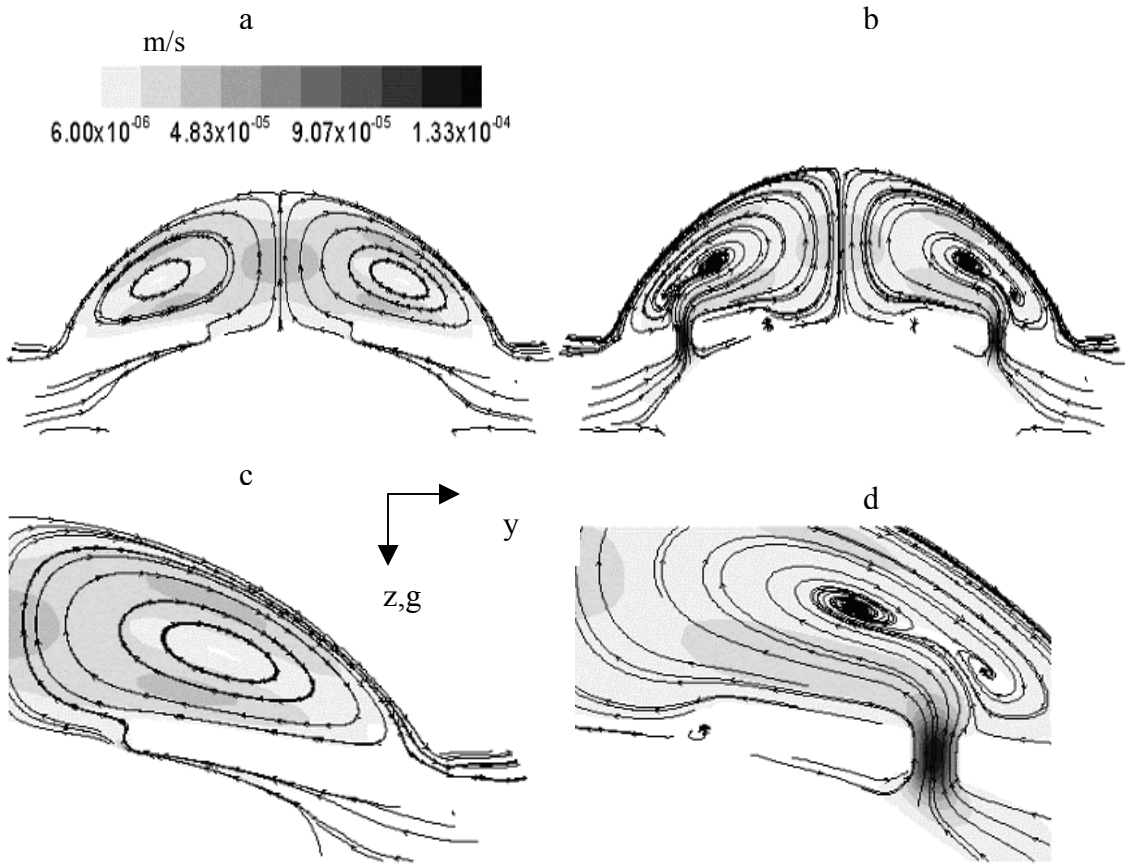

Figure 7-29: Comparison of streamlines and contours of velocity magnitude in vertical mid plane for the case of iridectomy when two holes are located opposite to each other at two-thirds of distance between the pupil border and iris periphery, Horizontal orientation. (a) Pupillary block (b) Hole opening (a) Pupillary block, extended view (b) Hole opening, extended view.

to Y-axis, Fig. [7-31b], and along a line parallel to X-axis, Fig. [7-31c], located on a vertical plane (parallel to the equatorial plane) inside the posterior chamber (Z=2.6 mm) to analyze the flow profile in the posterior chamber after creation of holes. Here holes are located on the Y-axis. For pupillary block simulation the maximum velocity magnitude in this vertical plane is 1.4 $\mu m / s$, while for peripheral iridectomy the velocity magnitude increases to 26 $\mu m / s$, Fig. [7-31b] (in the vicinity of hole), which is 18 times greater than the pupillary block simulation. On the location just opposite to the hole location, the velocity magnitude (1 $\mu m / s$) is even less than the pupillary block (1.4 $\mu m / s$) simulation as the flow is moving away from this location towards the location of the hole, Fig. [7-31b].

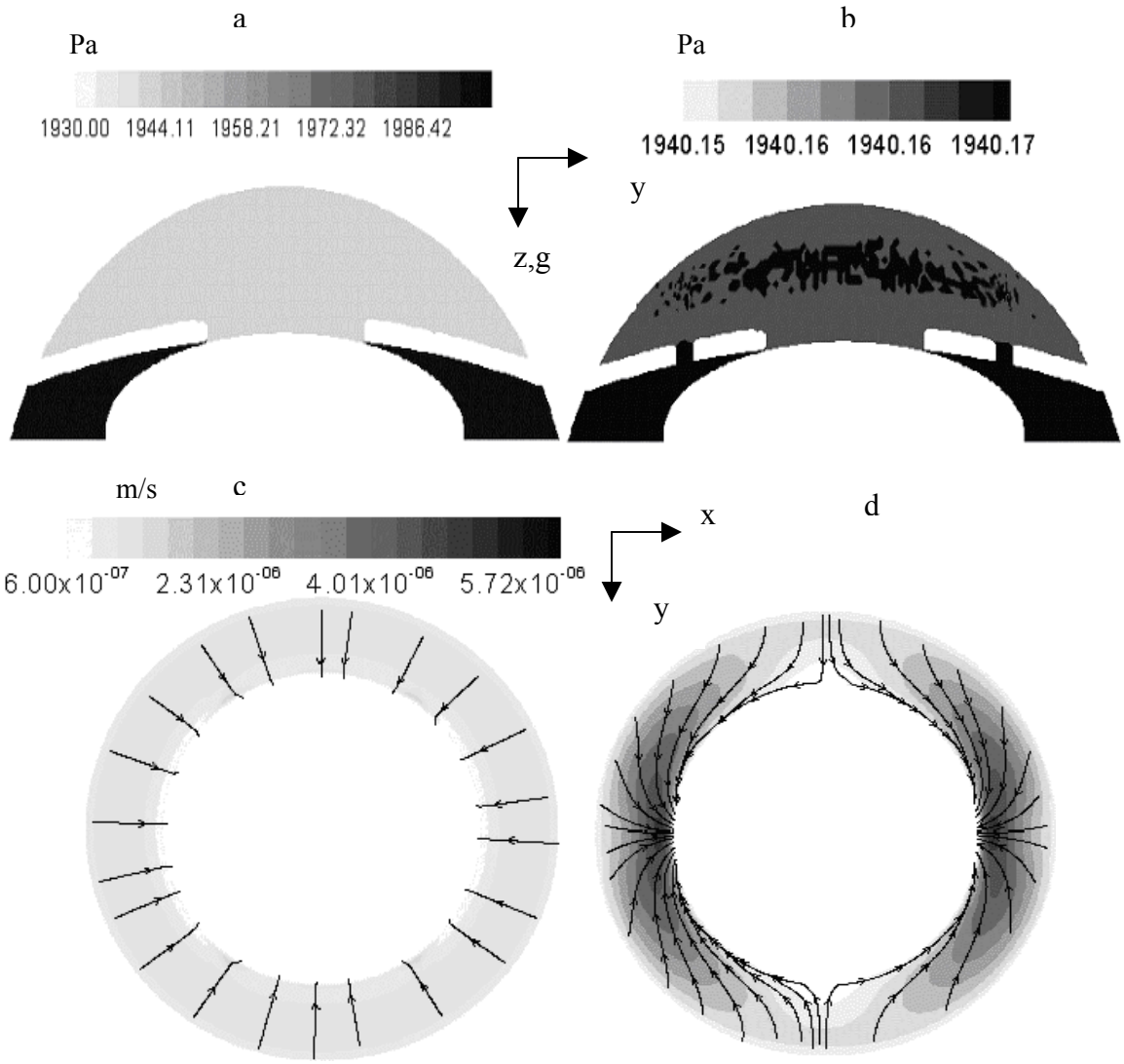

Figure 7-30: Comparison of pressure contours in vertical mid plane for the case of iridectomy when two holes are located opposite to each other at two-thirds of distance between the pupil border and iris periphery, Horizontal orientation. (a) Pupillary block (b) Hole opening. Comparison of streamlines and contours of velocity magnitude in plane parallel to equatorial plane (z = 2.6) for the case of iridectomy when two holes are located opposite to each other at two-thirds of distance between the pupil border and iris periphery, Horizontal orientation (c) Pupillary block (d) Hole opening.

For the iridectomy at the central location, the velocity magnitude increases to 10 $\mu m / s$ in the vicinity of the hole, Fig. [7-31b], which is 7 times greater than the velocity magnitude in pupillary block simulation at the corresponding location. For the central iridectomy increase in

AC-Anterior Chamber
a PC-Posterior Chamber

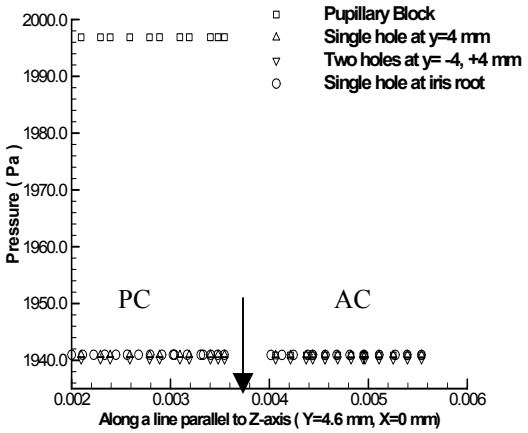

b c

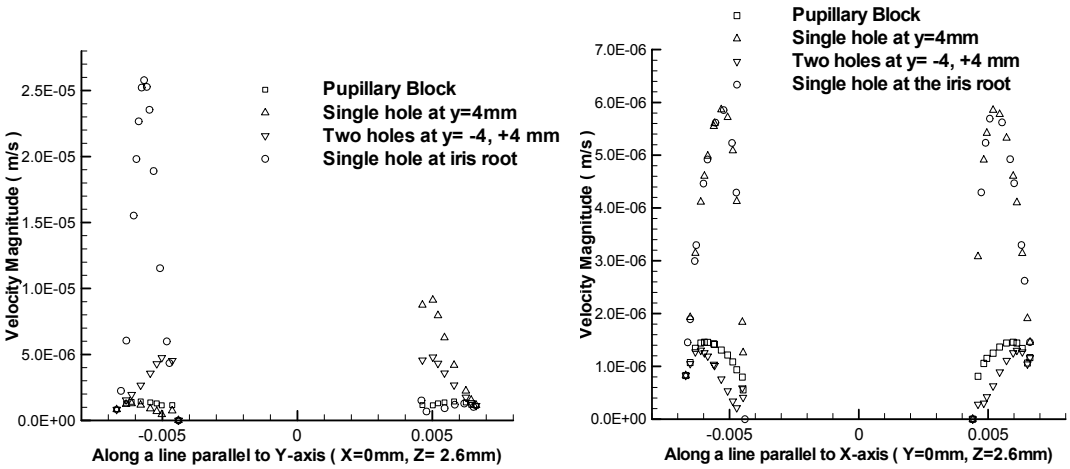

Figure 7-31: Iridectomy with hole located at two-thirds of distance between the pupil border and iris periphery, Horizontal Orientation, Comparison of velocity magnitude among pupillary block and various locations of holes (a) Comparison of pressure magnitude among pupillary block and various locations of holes along a line parallel to Z-axis (Y=4.6 mm, X=0mm). (b) Along a line parallel to Y-axis (X=0mm, Z=2.6mm) located inside the posterior chamber. (c) Along a line parallel to X-axis (Y=0mm, Z=2.6mm) located inside the posterior chamber.

the velocity magnitude is less than the peripheral iridectomy as the axis along which plots are made is close to the location of peripheral hole than the location of central hole. When two holes are created at the central location, Fig. [7-31b], then the velocity magnitude in the vicinity of the holes is 5 $\mu m / s$, which is half of the velocity magnitude for single hole central iridectomy at the location close to the holes.

When velocity magnitude is plotted along a line parallel to X-axis located in the posterior chamber (Z=2.6mm), then for the single hole peripheral or central iridectomy, velocity magnitude increases to 6 $\mu m/s$ on both sides of the line at the radial distance of 5 mm from the center of the vertical plane on which the line is located, Fig. [7-31c]. This is 4.2 times the velocity magnitude in the pupillary block simulation at the corresponding location. When two holes are created, then the velocity magnitude decreases at these locations with respect to the pupillary block simulation, Fig. [7-31c]. This line is located perpendicular to the axis of location of holes. So, when single hole is created either at peripheral or central location, flow rushes towards the location of the hole from the opposite location passing through these locations on the line. This leads to high velocity magnitude at those locations. But when two holes are created, the flow moves in symmetrical fashion from these locations towards the holes, which are located on the perpendicular axis. So velocity magnitude at these locations for two hole iridectomy is even less than the pupillary block simulation.

7.3 Comparison of Iridectomy at Different Locations

For different sites and different number of holes velocity magnitude is compared along a line parallel to Y-axis (Z=4.6 mm, X=0 mm) located inside the anterior chamber near to the iris periphery. 12 o'clock hole at central location and 12 & 6 o'clock hole at central location have approximately same amount of increase in velocity magnitude in the proximity of the iris surface at the location of 12 o'clock hole, Fig. [7-32a]. Making an additional hole does not bring any difference in the flow patterns of the anterior chamber. So there is no use of making hole at 6 o'clock position in addition to 12 o'clock hole. Creating hole at iris root (peripheral location) for 12 o'clock iridectomy is more beneficial than creating hole at central location as the flow coming from the hole at iris root work against the deposition of particle at this location. The flow is relatively weak in the proximity of the TM for the central location iridectomy and more supportive for particle deposition at this location. Peripheral hole leads to strong flow along the

upper corneal surface, Fig. [7-4b] and could be better for proper nutrition of upper corneal surface. 6 o' clock hole at the iris root is better than the 6 o'clock at the central position as hole at the central position leads to relatively weak flow in the vicinity of the lower TM and encourages the general tendency of particle to deposit at that location, Fig. [7-32b]. The hole at the iris root leads to a flow pattern in the vicinity of the TM, which opposes the particle deposition, Fig. [7-4c]. Iridectomy with hole located at 9 o'clock position at iris root or central location and iridectomy at 9 and 3 o'clock position do not show much difference from each other in the flow pattern and velocity magnitude in the vertical mid plane, Fig. [7-32c].

Table 7-1: Magnitude of maximum velocity and its location inside the eye for vertical orientation of the eye.

Iridectomy	Maximum velocity (μm /s)	Location of Maximum velocity	Iridectomy	Maximum velocity (μm /s)	Location of Maximum velocity
Normal(25 μm pupillary gap)	325	Pupil	12 o'clock (central)	452	Hole
Pupillary Block (3 μm gap)	474	Pupil	6 o'clock (central)	448	Hole
12 o'clock (Peripheral)	454	Hole	9 o'clock (central)	452	Hole
6 o'clock (Peripheral)	453	Hole	12 & 6 o'clock	431	12 o'clock hole
9 o'clock (Peripheral)	454	Hole	9 & 3 o'clock	326	Hole

For pupillary gap of 25 μm , the maximum velocity of 325 μm /s is observed at small gap between the iris and pupil which increase to 474 μm /s when gap size is reduced to 3 μm (Vertical orientation). For all iridectomy with single hole either at central location or at peripheral location, the maximum magnitude of velocity is around 450 μm /s observed inside the hole, Table [7-1]. For two hole iridectomy at 12 & 6 o'clock position the most of the flow enters through the upper hole located at 12 o'clock, but some flow also enters through 6'clock position, so maximum of velocity magnitude is slightly less (431 μm /s) than the other iridectomy. For 9 & 3 o'clock hole flow is equally distributed in two holes and maximum velocity (326 μm /s)

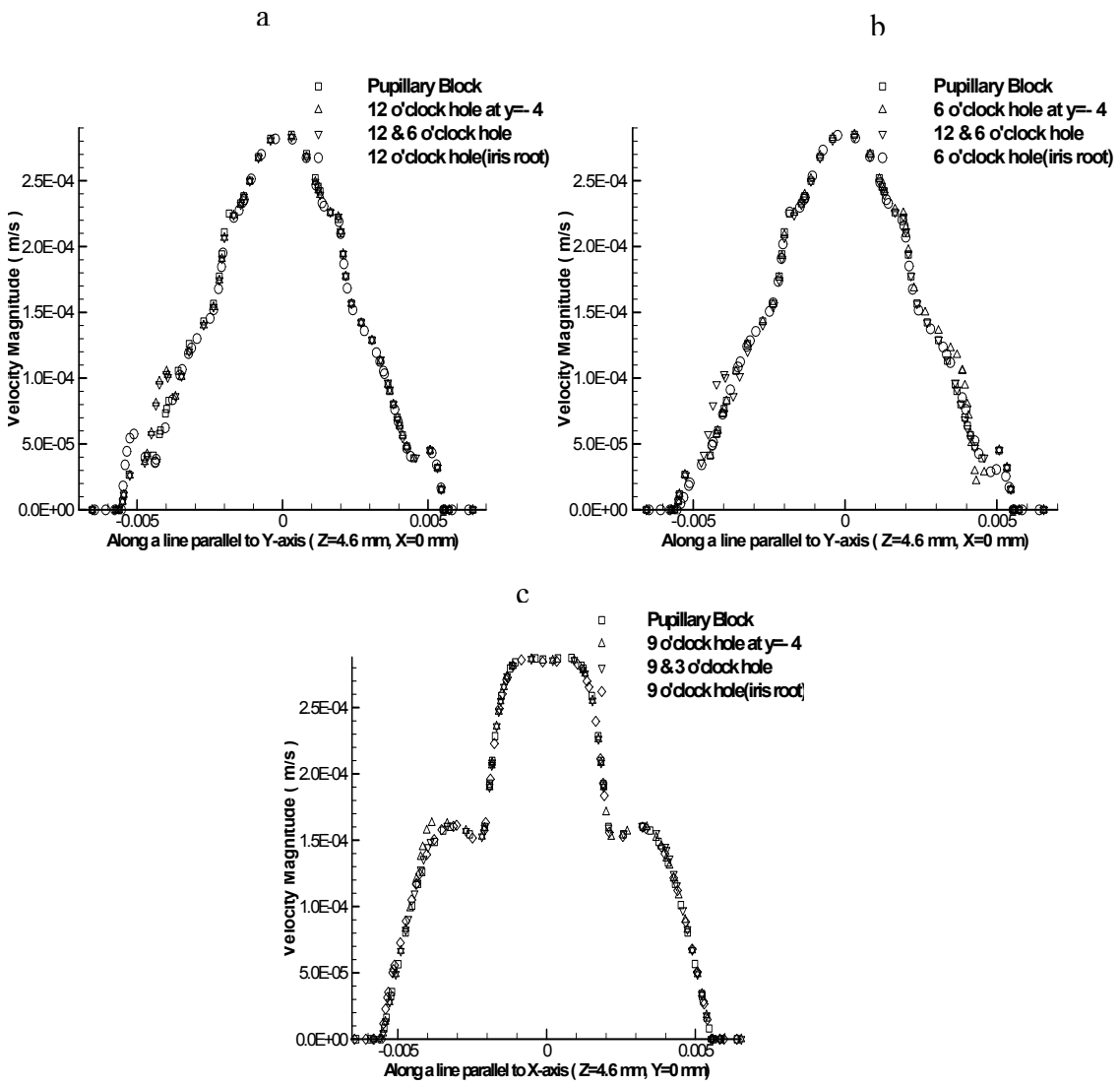

Figure 7-32: Comparison of velocity magnitude among pupillary block and various location of holes along a line parallel to Y-axis (Z=4.6 mm, X=0 mm) inside the anterior chamber near the iris periphery, Vertical orientation (a) Pupillary block, 12 o'clock hole at Y= - 4 mm, 12 & 6 o'clock holes at Y= +4 mm, -4 mm and 12 o'clock hole at iris root. (b) Pupillary block, 6 o'clock hole at Y= - 4 mm, 12 & 6 o'clock holes at Y= +4 mm, -4 mm and 6 o'clock hole at iris root. (c) Pupillary block, 9 o'clock hole at Y= - 4 mm, 9 & 3 o'clock holes at Y= +4 mm, -4 mm and 9 o'clock hole at the iris root.

magnitude observed inside the holes is much less compared to the other iridectomy.

For the horizontal orientation velocity magnitude is plotted along a line parallel to Y-axis (Z=4.6 mm, X=0mm) located inside the anterior chamber near the iris periphery for the pupillary block, single hole iridectomy at central and peripheral locations and two hole central iridectomy,

a b

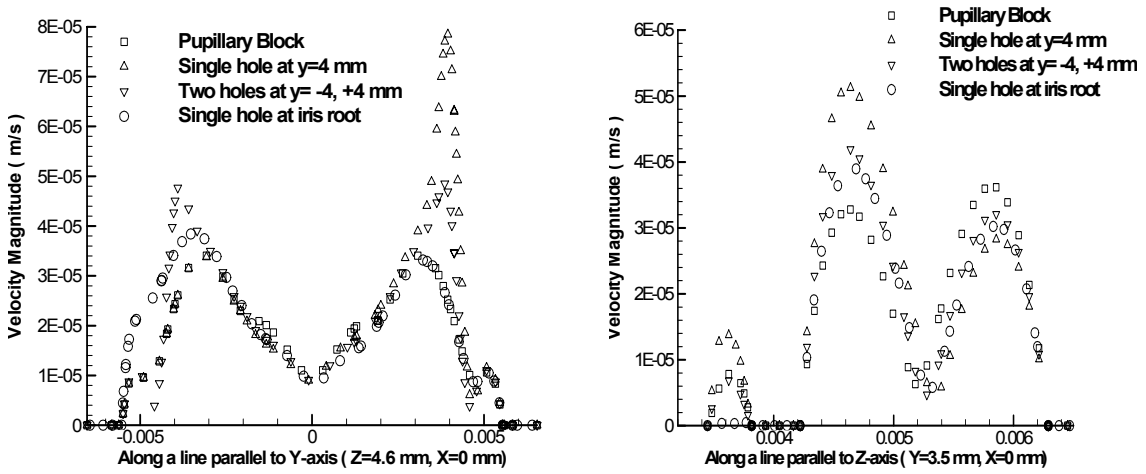

Figure 7-33: Iridectomy with hole located at two-thirds of distance between the pupil border and the iris periphery, Horizontal Orientation (a) Comparison of velocity magnitude among pupillary block and various locations of holes along a line parallel to Y-axis (Z=4.6 mm, X=0mm) inside the anterior chamber near to the iris periphery. (b) Comparison of velocity magnitude among pupillary block and the various location of holes along a line parallel to Z-axis (Y=3.5 mm, X=0mm).

Fig. [7-33a]. The plot shows that for single hole central iridectomy, the velocity magnitude increases to very high value (80 μm /s) close to the location of hole compared to the pupillary block simulation (35 μm /s), Fig. [7-33a]. For single hole peripheral iridectomy the increase in the velocity at the location of hole is relatively lower (40 μm /s) than the central iridectomy. When two holes are created, velocity-magnitude at the location of both the holes is 50 μm /s, Fig. [7-33a].

Table 7-2: Comparison of velocity magnitude on different parts of a line parallel (Y=3.5 mm, X=0 mm) to the central axis (Z-axis) for the horizontal orientation.

Iridectomy	Maximum of velocity magnitude (μm /s) close to the iris surface (Z=4.2 mm to 5.2 mm)	Maximum of velocity magnitude (μm /s) close to the corneal surface (Z=5.2 mm to 6.2 mm)
Pupillary Block (3 μm gap)	32	36
Peripheral (Single hole)	40	30
Central (Single hole)	52	28
Central (Two holes)	42	32

For the horizontal orientation of the eye when velocity magnitude is compared along a line (Y=3.5 mm, X=0 mm) parallel to central axis (Z-axis), Fig. [7-33b], it is observed that close to the iris surface the maximum of velocity magnitude is high for iridectomy simulation relative to the pupillary block simulation, Table [7-2]. It is highest for iridectomy with single hole at central location (52 μm /s), Fig. [7-33b], which reduces to 42 μm /s when two holes are performed at the central location. For single peripheral hole in the iris this magnitude is lowest (40 μm /s). When compared in the vicinity of the corneal location, the velocity magnitude diminishes for iridectomy simulations. The lowest value of maximum of velocity magnitude (28 μm /s) is observed for the single-hole iridectomy at central location, Fig. [7-33b]. For peripheral single hole it is 30 μm /s, while for two holes at central location it further increase to 32 μm /s, Fig. [7-33b]. The high values of velocity magnitude at tissue surface reflect low probability of particle deposition and vice versa.

For the horizontal orientation, when the pupillary gap is 25 μm , the maximum velocity magnitude of 133 μm /s is observed at small gap between the iris and pupil which increase to 474 μm /s when gap size is reduced to 3 μm (Vertical orientation). For single hole iridectomy maximum velocity of 448 μm /s is observed inside the hole which reduces to 225 μm /s when two holes are created due to equal distribution of flow, Table [7-3].

Table 7-3: Magnitude of maximum velocity and its location inside the eye for horizontal orientation of the eye.

Iridectomy	Maximum velocity (μm /s)	Location of Maximum velocity	Iridectomy	Maximum velocity (μm /s)	Location of Maximum velocity
Normal (25 μm pupillary gap)	133	Pupil	Central (Single hole)	448	Hole
Pupillary Block (3 μm gap)	474	Pupil	Central (Two holes)	225	12 o'clock hole
Peripheral (Single hole)	448	Hole			

The contours of velocity magnitude and streamlines in different planes passing through posterior and anterior chambers show that if single hole iridectomy is to be performed, the best location is 12 o'clock peripheral position. This is most preferable site as symmetry is maintained across the vertical mid plane; strong flow along upper corneal surface and upper TM show unfavorable flow pattern for particle deposition and proper nutrition to tissues is expected. When iridectomy between 9 & 11 o'clock position or 1 & 3 o'clock position is to be performed, the flow patterns for different iridectomy simulation suggest that it is better to perform one hole in the vicinity of 9 o'clock position and other in the vicinity of the 3 o'clock position. This will help in maintaining the symmetry in flow pattern of the posterior and anterior chamber, which could prevent the eye from any uneven tissue development, which could be probable by disproportionate nutrition of the ocular tissues if flow patterns are asymmetric.

7.4 Concluding Remarks

A three-dimensional model for the anterior and posterior chamber of eye is developed in order to investigate the re-distribution in the flow and pressure profile after the iridectomy is performed. Different simulations on the eye model are performed which helps in understanding the flow dynamics of eye for pupillary block, angle closure glaucoma and iridectomy. The effect of pupillary block is modeled by decreasing the gap between the iris and lens. Angle closure glaucoma is simulated by closing the part of TM, which represents the inaccessibility of TM for outflow. Iridectomy is simulated by creating holes in the iris surface. The effect of location of holes in the iris surface is considered for one and two hole iridectomy from point of view of asymmetry introduced in flow profile, nutrition of tissues and particle deposition on ocular tissues. The following major observations are made from the computed results:

(1) The pressure differential between the posterior and anterior chamber is found to be dependent on the gap between the iris and lens. Decreasing the pore size causes the blockage of flow into the

anterior chamber, while secretion rate from ciliary body has not been changed. This leads to elevation of pressure in the posterior chamber.

(2) Anterior bulging of the iris surface in eyes with angle closure glaucoma leads to contact between the lower part of the TM and posterior iris surface, which results in narrow anterior chamber angle. High elevation in IOP (24 mm of Hg) is observed by closing the lower half of the TM. This elevation in IOP is in agreement with the observed pressure elevation in some cases of angle closure Glaucoma. So the present model is able to predict the dependence of TM closure and corresponding rise in IOP.

(3) Iridectomy at any location in the iris surface leads to direct passage of flow into the anterior chamber through the holes created in the iris surface. There is almost negligible flow through the gap between the iris and lens as most of the flow secreted in the posterior chamber by the ciliary body rushes towards the location of holes in the iris surface and then enter the anterior chamber through the holes.

(4) Iridectomy leads to release in the posterior chamber pressure, but there is no change in the anterior chamber pressure by creating holes, as effect of iris bulging is not considered in the present model.

(5) When only one hole is created for iridectomy, it brought significant changes in the flow distribution in the vicinity of the holes. The part of the anterior chamber on the other side of the hole is not much affected, as buoyancy is dominant flow driving mechanism inside the anterior chamber. This leads to asymmetry in the flow distribution in the both anterior and posterior chambers.

(6) Peripheral iridectomy is found to be more beneficial than the central iridectomy. The holes created at the iris root causes strong flow in the vicinity of the corneal surface and TM, which

work against the particle deposition on the ocular tissues. The hole created at the central location lead to weak flow in the vicinity of the TM and provides favorable condition for the particle deposition. So peripheral iridectomy should be preferred over central iridectomy. Even from nutrition prospective of ocular tissues peripheral seems to be better than the central iridectomy.

(7) 12 o'clock hole or 6 o'clock hole iridectomy leads to symmetric flow profile along the vertical mid plane, while this symmetry is destroyed for 9 o'clock iridectomy. So when single hole is to be created, the 12 o'clock iridectomy provides better results than the other locations.

(8) Creating a additional hole at 6 o'clock with 12 o'clock iridectomy do not bring any significant change in the flow profile, so it is not advisable to create a additional hole in this arrangement.

(9) When holes are created at 9 & 3 o'clock position, it maintains symmetry across the vertical and horizontal mid planes of the anterior chamber. The flow rushes towards the holes in the posterior chamber such that symmetry in the posterior chamber is also maintained along the vertical mid plane. So this is found to be preferable arrangement as far as symmetry in flow distribution and even nutrition to ocular tissues are considered.

BIBLIOGRAPHY

(1) Palkama, A., Beureman, R., and Reynaud, J., "Ocular fluid dynamics measured with vivo confocal microscopy and microbeads", Ophthalmology, 2001.

(2) Lehto, I., Ruusuvaara, P. and Setala, K., "Corneal endothelim in pigmentary glaucoma and pigment dispersion syndrome", Ophthalmologica, 68, pp. 703-709, 1990.

(3) Bill, A., "Blood circulation and fluid dynamics in the eye", Physiological reviews, 55, pp. 383-417, 1975.

(4) Crouch, E. R. and Crouch, E. R., "Management of traumatic hyphema: Therapeutic options", Journal of Pediatric Ophthalmology & Strabismus, 36(5), pp. 238-250, 1999.

(5) Alessandro, L. P., Forster, D. J. and Rao, N. A., "Anterior uveitis and hypopyon", American Journal of Ophthalmology, 112, pp. 317-321, 1991.

(6) Mclaren, J. W., Trocme, S. D., Relf, S., and Brubaker, R. F., "Rate of flow of aqueous humor determined from measurements of aqueous flare," Invest Opthalmol Vis Sci., 31(2), pp. 339-346, 1990.

(7) Heys, J. J., Barocas, V. H., and Taravella, M. J., "Modeling passive mechanical interaction between aqueous humor and iris," Journal of Biomechanical Engg., 123, pp. 540-546, 2001.

(8) Efron, N., Young, G., Brennan, N. A., "Ocular surface temperature", Current Eye Research, 8, pp. 901-905, 1989.

(9) Okuno, T., " Thermal effect of infrared radiation on the eye: a study based on a model," Ann. Ocuup. Hyg., 35, pp. 1-12, 1991.

(10) Tripathi, R. C., and Tripathi, B. J., "Anatomy of the human eye, orbit, and adnexa", in The Eye, Vol 1a, Vegetative physiology and biochemistry, edited by Hugh Davson, Academic Press, 1984.

(11) Mori, A., Oguchi, Y., Okusawa, Y., Ono, M., Fujishima, H., and Tsubota, K., "Use of high-speed, high-resolution thermography to evaluate the tear film layer," American Journal of Ophthalmology, 124, pp. 729-735, 1997.

(12) Kocak, I., Orgul, S., and Flammer, J., "Variability in the measurement of corneal temperature using a non-contact infrared thermometer," Ophthalmologica, 213(6), pp. 345-349, 1999.

(13) Johnson, M. C., Kamm, R. D., Grant, W. M., Epstein, D.L., and Gasterland, D., "The flow of aqueous humor through micro-porous filters," Invest Opthalmol Vis Sci., 27, pp. 92-97, 1986.

(14) Ethier, C. R., Coloma, M. F., Kater, A. W., and Allingham, R. R., "Retroperfusion studies of the aqueous outflow system," Invest Opthalmol Vis Sci., 34(2), pp. 385-394, 1992.

(15) Ethier, C. R., Kamm, R.D., Johnson, M., Pavoo, A. F. and Anderson, P.J., "Further studies on the flow of aqueous humor through microporous filters," Invest Opthalmol Vis Sci., 30, pp. 739-746, 1989.

(16) Johnson, M. C., and Kamm, R. D., "The role of schlemm's canal in aqueous outflow from the human eye," Invest Opthalmol Vis Sci., 24, pp. 320-325, 1983.

(17) Ethier, C. R., Kamm, R. D., Palaszewski, B. A., Johnson, M.C. and Richardson, T.M., "Calculations of flow resistance in the juxtacanalicular meshwork," Invest Opthalmol Vis Sci., 27, pp. 1741-1750, 1986.

(18) Johnson, M., Shaprio, A., Ethier, C. R., and Kamm, R.D., "Modulation of outflow resistance by the pores of the inner wall endothelium," Invest Opthalmol Vis Sci., 33, pp. 1670-1675, 1992.

(19) Scott, J. A., "A finite element model of heat transport in the human eye," Phy. Med. Biol., 33, pp. 227-241, 1988.

(20) Scott, J. A., "The computation of temperature rises in the human eye induced by infrared radiation," Phy. Med. Biol., 33, pp. 243-257, 1988.

(21) Heys, J. J., and Barocas, V.H., "Computaional evaluation of the role of accommodation in pigmentary glaucoma," Invest. Opthalmol. Vis. Sci., 43, pp. 700-708, 2002.

(22) Canning, C. R., Dewynne, J. N., Fitt, A. D., and Greaney, M. J., "Fluid flow in the anterior chamber of a human eye," IMA Journal of Mathematics Applied in Medicine and Biology, pp. 1-33, 2002.

(23) Heys, J. J., and Barocas, V. H., "A Boussinesq model of natural convection in the human eye and the formation of krukenberg's spindle," Annals of Biomedical Engineering, 30, pp. 392-401, 2002.

(24) Rodrigues, M. M., Spaeth, G. L., Weinreb, D. and Sivalingam, E. "Spectrum of trabecular pigmentation in open-angle glaucoma: A clinicopathologic study," Tr. Am. Acad. Ophthalmol. Oto-laryngol., 81, pp. 258-276, 1976.

(25) Kuchle, M., Christian, Y.M., Nguyen, N.X., Martus., "Quantification of aqueous melanin granules in primary pigment dispersion syndrome", Am J Ophthalmol., 126, pp. 425-431,1998.

(26) Bergenske, P. D., "Krukenberg's spindle and contact lens-induced edema", American Journal of Optometry & Physiological Optics, 57(12), pp.932-935, 1980.

(27) Epstein, D. L., Freddo, T. F., Anderson, P. J., Patterson, M. M., and Chu, S. B., "Experimental obstruction to aqueous outflow by pigment particles in living monkeys", Invest. Opthalmol. Vis. Sci., 27, pp. 387-395, 1986.

(28) Gray, H., "Angiology (The Blood)", in Anatomy of the Human Body, edited by Warren H. Lewis, Philadelphia: Lea & Febiger, 1918. (http://www.bartleby.com/107/134.html).

(29) Sit, A. J., Coloma, F. M., Ethier, C. R. and Johnson, M., "Factors affecting the pores of the inner wall endothelium of schlemm's canal", Invest Opthalmol Vis Sci. 38(8), pp. 1517-1525, 1997.

(30) Wilson, F. M., "Traumatic hyphema: Pathogenesis and management", Ophthalmology, 87, pp.910-919, 1980.

(31) Riley, H. D., "Krukenberg's spindle", in V553 Anterior Segment Path Lecture Notes (http://www.opt.indiana.edu/Riley/HomePage/V553_Path_Slide_Lecture/6Krukenberg's_Spindle.html)

(32) Prof. Alistair Fitt Homepage, "Pictures of Eyes, Department of Mathematics, University of Southampton, United Kingdom", (http://www.maths.soton.ac.uk/staff/Fitt/eyes.htm).

(33) Bergman , R. A., Afifi, A. K., and Heidger, P. M., "Section 4: Blood" in Atlas of microscopic anatomy.

(34) Yedder, R. B. and Bilgen, E., "Laminar natural convection in inclined enclosures bounded by a solid wall", Heat and Mass Transfer, 32, pp. 455-462, 1997.

(35) Mallinson, G. D. and Davis, G. D. V., "Three-dimensional natural convection in a box: a numerical study", Journal of Fluid Mechanics, 83(1), pp. 1-31,1977.

(36) Mullenax, C. A., "Doctoral Research Prospectus," (http://www.studentweb.Tulane.edu/~cmullen/documents.html), pp. 6.

(37) Huillier, J. P., and Sbirlea, G. A., "Morphology of the human eye: Glaucoma physiology and laser iridectomy", in Medical applications of computer modelling: Cardiovascular and ocular systems, edited by T. B. Martonen, WIT Press, 2000.

(38) Ergun, S., "Fluid flow through packed columns," Chemical Engineering Progress, 48(2), pp. 89-94, 1952.

(39) Haider, A. and Levenspiel, O., "Drag coefficient and terminal velocity of spherical and non-spherical particles, Powder Technology, 58, pp. 63-70, 1989.

(40) Doormal, J. P., and Raithby, G. D., "Enhancements of the SIMPLE method for predicting incompressible fluid flow", Numer. Heat Transfer, 7, pp. 147-163, 1984.

(41) Gerlach, J. C., Hentschel, G., Zeilinger, K., Smith, M. D. and Neuhas, P., "Cell detachment during sinusoidal reperfusion after liver preservation", in vitro model, Transplantation, 64, pp. 907-912, 1997.

(42) Lindenmayer, J. M., Kahn, M.G., Hertzman, E., Epstein D.L., "Morphology and function of the aqueous outflow system in monkey eyes perfused with sulfhydryl agents", Invest. Opthalmol. Vis. Sci., 24, pp. 710, 1983.

(43) Lutzen-Drecoll E., "Structural factors influencing outflow facility and its changeability under drugs", Invest. Opthalmol. Vis. Sci., 12, pp. 280-294, 1973.

(44) Kampik, S., Green, W. R., Quigley, H. A., and pierce, L. H., "Scanning and transmission electron microscopic studies of two cases of pigment dispersion syndrome", American Journal of Ophthalmology, 91, pp. 573-587, 1981.

(45) Sugar, H. S., "Pigmentary glaucoma. A 25 year review," Am. J. Ophthalmol., 62, pp. 499, 1966.

(46) Wilson, F. M., "Traumatic hyphema: Pathogenesis and management", Ophthalmology, 87 (9), pp. 910-919, 1980.

(47) Lai, J. C., Fekrat, S., Barron, Y. and Goldberg, M. F., "Traumatic hyphema in children: Risk factors for complications", Arch Ophthalmol., 119, pp. 64-70, 2001.

(48) Lai, W. W., Bhavnani, V. D., Tessler, H. H., Edward, D. P., "Effect of melanin on traumatic hyphema in rabbits", Arch Ophthalmol., 117, pp. 789-793, 1999.

(49) Komaromy, A. M., Brooks, D. E., Kallberg, M. E., Andrew, S. E., ramsey, D. T. and Ramsey, C. C., "Hyphema. Part-II Diagnosis and treatment", Compdenduim, 22(1), pp. 74-79, 2000.

(50) Wilson, F. M., "Traumatic hyphema: Pathogenesis and management", Ophthalmology, 87, pp. 910-919, 1980.

(51) Lozada, G., Rosedale Vision Center, Kansas City, KS (www.rosedalevision.com/eyecare.htm)

(52) Olsen, T. W., Sternberg, P., Martin, D. F., Capone, A., Lim, J. I., and Aaberg, T. M., "Postoperative hypopyon after intravitreal bovine thrombin for macular hole surgery", American Journal of Ophthalmology, 121(5), pp. 575-577, 1996.

(53) Pollack, I. P., " Use of argon laser energy to produce iridotomies," Tr. Am. Ophth. Soc. Vol., 77, 1979.

(54) Pavlin, C. "Glaucoma (Pupillary Block)", http://www.eyeubm.com/pavlin.atlas/Glaucoma/PupillaryBlock.htm

(55) Wills Eye Hospital, "Glaucoma treatments in Laser Therapy for Glaucoma", http://www.wills-glaucoma.org/laser.htm

(56) Kohnen, T., "Lasers in Eye Surgery," http://www.karger.com/gazette/64/kohnen/art_5_2.htm#fig3

VITA

Satish Kumar was born in Patna, a small historical town in India. He is the son of Mrs. Sudha Singh and Mr. Deo Prasad Singh. He got his primary and secondary education in Patna. He received the Bachelor of Technology in Mechanical Engineering from Indian Institute of Technolgy, Guwahati, a prestigious technical institute in India in 2001. He then joined the graduate program at Louisiana State University, Baton Rouge (LSU) in Fall, 2001. He worked on Computational Fluid Dynamics during this graduate program specializing in modeling of ocular fluids. He is a candidate for the degree of Master of Science in Mechanical Engineering to be awarded at the commencement of December 2003. After completing his master's degree he would be pursuing his doctoral program in Purdue University.